

Wide Band Gap Chalcopyrite Photoelectrodes for Direct Water Splitting

Final Technical Report

**United States Department of Energy
Award Number DE-EE0006670**

**Submitted by
Hawaii Natural Energy Institute
School of Ocean and Earth Science and Technology
University of Hawaii at Manoa**



October 2019

Final Technical Report

Project Title: Wide Band Gap Chalcopyrite Photoelectrodes for Direct Water Splitting

PI: Dr. Nicolas Gaillard
Phone: 808-956-2342
Email: ngaillar@hawaii.edu

Project Period: October 1, 2014 – May 31, 2019

Recipient: University of Hawaii / Hawaii Natural Energy Institute
2440 Campus Road, Box 368
Honolulu, HI 96822

Award Number: DE-EE0006670

Working Partners: University of Nevada, Las Vegas (Prof. Clemens Heske, Drs. Monica Blum, Lothar Weinhardt and James Carter)
Stanford University (Prof. Thomas Jaramillo and Drs. Thomas Hellstern and David Palm)
Lawrence Livermore National Laboratory (Drs. Tadashi Ogitsu and Joel Varley)
National Renewable Energy Laboratory (Drs. Kai Zhu, Christopher Muzzillo, Miguel Contreras, Heli Wang and Todd Deutsch)

Executive Summary

The chalcopyrite material class, typically identified by its most popular alloy CuInGaSe_2 , provides exceptionally good candidates for photoelectrochemical (PEC) water splitting and has the potential to meet DoE EERE's targets in terms of hydrogen production costs (less than \$2/gge). Some key advantages of this class include remarkable photon-to-electron conversion efficiency and a high Faradaic efficiency for the hydrogen evolution reaction, two characteristics essential for efficient PEC water splitting. However, the band gaps of commonly used chalcopyrites in the photovoltaic field (1.0-1.6 eV) are too narrow to be compatible with the multi-junction approach for efficient PEC hydrogen production, in which a stack of solar absorbers generates the bias required for water splitting. Nonetheless, previous studies performed by our team demonstrated that chalcopyrites' narrow band gaps could be effectively widened using simple conversion steps, leading to functional chalcopyrite-based PEC electrodes with optical band gap in the 1.8-2.4 eV range, making this class highly suitable for renewable hydrogen production via water splitting.

This multi-disciplinary research program lead by the University of Hawai'i/Hawai'i Natural Energy Institute combined unique analytical techniques (UNLV), state-of-the-art theoretical modeling (LLNL) with advanced thin film materials synthesis (HNEI, NREL and Stanford) to provide deeper understanding of wide band gap chalcopyrite-based PEC materials and engineer high performance/corrosion-resistant photocathodes with tunable energetics and compatible with the multi-junction approach. The goals of this project were to demonstrate photoelectrochemical (PEC) solar-hydrogen production using a dual absorber system with a solar-to-hydrogen conversion efficiency of at least 15% with an operational life up to 2,000 hours and capable of generating at least 3 liters of hydrogen in 8 hours.

After a brief introduction (Section 1) and description of our work plan (Section 2), we present in Section 3 our results on the development of new wide bandgap copper chalcopyrites absorbers for PEC waters splitting. We first show through modeling how alloying can be used to tailor the optical properties and/or surface energetics of various material candidates. We also present how specific defects (e.g., Ga_{Cu}) can lead to recombination centers within the forbidden gap of copper-poor chalcopyrites. Then, we present our efforts to synthesize high efficiency wide band gap CuGa_3Se_5 , $\text{CuGa}(\text{S},\text{Se})_2$ and $\text{Cu}(\text{In},\text{Ga})\text{S}_2$ photocathodes capable of generating photocurrent density over 10 mA/cm². We also demonstrate that Cu-rich absorbers should be avoided as they lead to poor sub-band gap optical transmission. In Section 4, we first report on our efforts to tune the energetics of chalcopyrites toward the hydrogen evolution reaction. First, we quantified the energetics of wide band gap chalcopyrites interfaced with conventional CdS buffer layer, as measured with X-ray photoelectron spectroscopy techniques, and evidence the presence of a large (and undesirable) conduction band offset at this interface. Then, we highlight some of the work performed with alternative buffer layers, including In_2S_3 . Durability improvements with various ultra-thin protective layers are presented in Section 5. Our data show that TiO_2 combined with MoS_2 can significantly improve chalcopyrites lifetime up to 350 hours under continuous operation at 8 mA/cm². Finally, in Section 6 we report strategies to integrate chalcopyrite photocathodes into standalone tandem PEC devices. Although promising methods were proposed for both mechanical and monolithic stacking with narrow band gap PV drivers, no functional device was fabricated on time to fulfill the program end goals.

Outline

| | |
|--|-----------|
| 1. Introduction..... | 5 |
| a. Background..... | 5 |
| b. Technical barriers..... | 8 |
| 2. Work Plan..... | 9 |
| 3. Technical achievements in Task 1 “Wide band gap chalcopyrite absorbers” | 11 |
| a. Theoretical modeling..... | 11 |
| i. Chalcopyrite alloy properties..... | 11 |
| ii. Chalcopyrite/buffer band alignment | 12 |
| iii. Chalcopyrite absorbers band gaps, thermodynamic stability, and defect tolerance | 13 |
| b. Wide band gap CuGa₃Se₅ absorbers..... | 14 |
| i. Effects of Cu/Ga composition on wide band gap chalcopyrite films | 14 |
| ii. Resistivity of CuGa ₃ Se ₅ | 17 |
| iii. Improved CuGa ₃ Se ₅ solar cell open-circuit voltages..... | 18 |
| iv. Transparent devices for tandem top cells..... | 18 |
| v. Conclusions..... | 20 |
| c. Wide band gap CuGa(S,Se)₂ absorbers..... | 20 |
| i. Overview..... | 20 |
| ii. Development of Functional E _G -tunable CuGa(S,Se) ₂ Photocathodes | 21 |
| iii. PEC Performance of Functional E _G -tunable CuGa(S,Se) ₂ Photocathodes | 24 |
| d. Wide band gap Cu(In,Ga)S₂ absorbers from Cu(In,Ga)Se₂ precursors | 31 |
| i. Overview..... | 31 |
| ii. Synthesis techniques | 31 |
| iii. Microstructural, chemical and optical properties of Cu(In,Ga)S ₂ absorber..... | 32 |
| iv. Photoelectrochemical properties of Cu(In,Ga)S ₂ absorbers | 36 |
| v. Conclusions..... | 37 |
| e. Wide band gap Cu(In,Ga)S₂ absorbers from Cu-In-Ga metallic precursors..... | 38 |
| i. Overview..... | 38 |
| ii. CuInS ₂ thin film processing and PEC/PV characterizations..... | 38 |
| iii. Band gap tunable Cu(In,Ga)S ₂ thin film synthesis and PEC/PV characterization | 39 |
| 4. Technical achievements in Task 2 “Sub-surface energetics improvement” | 42 |
| a. Surface and interface characterization by photoelectron spectroscopy | 42 |
| i. Chemical characterization of Cu(In,Ga)S ₂ absorber and CdS buffer layer surfaces | 42 |
| ii. Chemical characterization of several chalcopyrite-based absorber surfaces..... | 44 |
| iii. Chemical and electronic characterization: band alignment at the CdS/CIGS interface | 46 |
| b. Surface treatment of chalcopyrite photocathodes with n-type buffer layers..... | 51 |
| 5. Technical achievements in Task 3 “Surface catalysis and corrosion resistance” | 54 |
| a. ALD MoS₂ development..... | 54 |
| b. MoS₂/TiO₂ coating strategy..... | 54 |
| c. TiO₂ durability investigation | 56 |
| 6. Technical achievements in Task 4 “Structure validation and benchmark efficiency measurement” | 58 |
| a. Temperature resistant transparent conductive oxides as window layers..... | 58 |

| | | |
|-----|---|----|
| b. | CuGaSe ₂ /GaAs Tandem PEC cell | 60 |
| 7. | Summary and outlook | 62 |
| 8. | Acknowledgments | 64 |
| 9. | Disclaimer | 64 |
| 10. | Products developed under the Award | 65 |
| a. | Research papers (6) | 65 |
| b. | Invited presentations (24) | 65 |
| c. | Contributed presentations (9)..... | 67 |
| d. | Poster presentations (8)..... | 68 |
| 11. | References cited..... | 70 |

1. Introduction

a. Background

State-of-the-art standalone Photoelectrochemical (PEC) devices. Renewable hydrogen generation via PEC water splitting has received considerable attention since the first demonstration of spontaneous water cleavage with a single TiO₂ absorber under UV light illumination.¹ However, no single-junction PEC system can split water at the rate required for economically viable hydrogen production. Stacking a photoelectrode with one or more solar cells in a multi-junction structure, also known as Hybrid Photo-Electrodes (HPE),² is an elegant and practical way to generate sufficient photovoltage and photocurrent densities for reasonable solar-to-hydrogen (STH) efficiencies. Using amorphous silicon-germanium-based triple junction solar cells, Rocheleau, Miller, and Misra at the Hawai'i Natural Energy Institute (HNEI) demonstrated STH efficiencies as high as 7.8%.³ Also, Reece and Nocera demonstrated an STH efficiency of 4.7% with a silicon-based triple junction structure in neutral pH conditions.⁴ Gaillard and Kaneshiro at HNEI reported an STH efficiency of 3.1% using a WO₃-based photoanode and double-junction a-Si solar cells.⁵ With a comparable structure, Abdi recently reported a 4.9% STH efficiency with Mo-doped BiVO₄ photoanodes.⁶ Finally, the Turner group at NREL currently holds the world record STH efficiency (16.4%) with *PV-grade* III-V-based HPE devices.⁷ Although extremely attractive based on their efficiency, III-V systems fall short in terms of stability under PEC operation (< 100 hrs.) and in terms of cost due to the need for expensive fabrication processes. While promising pathways are being investigated to overcome these challenges, it is necessary to evaluate alternative materials.

Chalcopyrite thin films for PEC water splitting. The chalcopyrite material class, typically identified by its most popular *PV-grade* alloy CuInGaSe₂, provides exceptionally good candidates for PEC water splitting and has the potential to meet DoE EERE's ultimate targets. A key asset of this band gap tunable, direct absorber, thin film semiconductor material is its outstanding photon-to-electron conversion efficiency, as demonstrated with the short-circuit photocurrent densities (J_{sc} , 35 mA/cm²) achieved with low band gap CuInGaSe₂-based PV cells.⁸ HNEI has already demonstrated that chalcopyrite-based PEC systems can generate photocurrent densities comparable to those achieved by CuInGaSe₂-based solar cells (Figure 1.a) and evolve H₂ with Faradaic efficiencies greater than 85%⁹ even without a catalyst (Figure 1.b) - two major requirements for efficient H₂ production via PEC water splitting. However, chalcopyrite photocathodes suffer from non-ideal interfacial band-edge mismatch with respect to the hydrogen evolution reaction (HER), requiring additional PV cells to drive the water splitting process. Using a 1.67 eV band gap CuGaSe₂ photocathode connected in series with three a-Si PV drivers, HNEI has achieved an STH efficiency of 4% (Figure 1.c).⁹ Using a similar coplanar architecture, the Ångström Laboratory in Uppsala University, Sweden, reported a 10% STH efficiency using three series-connected CuInGaSe₂ solar cells of the same 1.1 eV narrow band gap.¹⁰ In both HNEI and the Ångström Laboratory's experiments, the use of coplanar schemes was dictated by the band gaps of the pure selenide compounds that were too narrow for the HPE stacked approach. Thus, device STH efficiencies were limited by the *relative area* occupied by each chalcopyrite system. The development of advanced wide band gap chalcopyrites allows for relocation of the underlying PV drivers, thereby increasing the STH efficiency.

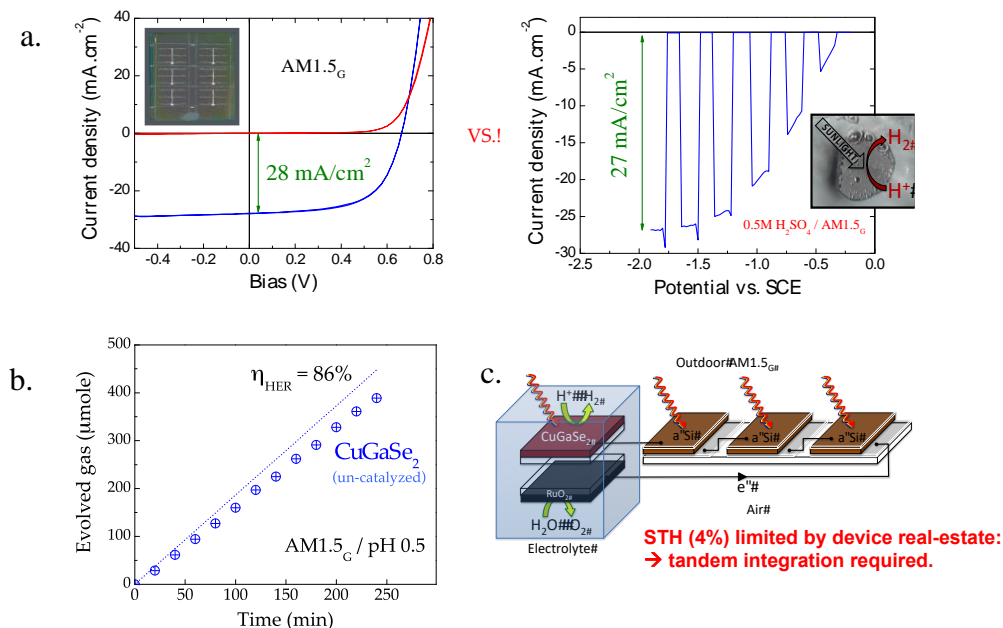


Figure 1. (a) Comparison of current-voltage and linear sweep voltammetry characteristics measured on two 1.3 eV CuInGaSe₂ absorbers originating from the same deposition run and integrated either as (left) a solar cell or (right) a photocathode. (b) Faradaic efficiency measured on 1.67 eV CuGaSe₂ photocathode. (c) Schematic of HNEI's CuGaSe₂-aSi coplanar PEC device generating hydrogen with a 4% STH efficiency.

Description of the HPE device. This program aimed at developing a dual absorber chalcopyrite-based HPE device, consisting of one *PV driver* and one photocathode, capable of producing hydrogen via water splitting in an acidic electrolyte using sunlight as the only source of energy input (Figure 2.a). The *PV driver* is made of a narrow band gap ($1.2 \text{ eV} < E_G < 1.4 \text{ eV}$) chalcopyrite-based solar cell, integrated on a metallic substrate. A catalyst for the oxygen evolution reaction (OER) is deposited on the backside of the metallic substrate, serving as the anode. A wide band gap chalcopyrite material ($1.8 \text{ eV} < E_G < 2.0 \text{ eV}$), deposited on a transparent conductive oxide (TCO) substrate and interfaced with an n-type “buffer” serves as the photocathode. An ultra-thin layer that can serve as the HER catalyst as well as a protective layer against corrosion is deposited on top of the photoelectrode. Placing the PEC electrode on top of the *PV driver* via a mechanical stack forms the HPE device.⁵⁻⁶

Maximum achievable STH efficiency with dual-absorber HPE devices. Below we show modeling work performed by the Jaramillo group to determine theoretically achievable STH efficiencies for HPE devices with varying levels of loss.¹¹ These losses arise from several sources, including free energy losses in the excited charge carriers versus the band gap (Figure 3.a) as well as catalyst overpotentials required to drive the respective half reactions of water splitting. Figure 3.b shows calculated achievable STH efficiencies for a hypothetical device with losses typical for known materials: 0.49 eV free energy loss from each semiconductor, and overpotentials for Pt (HER) and RuO₂ (OER) catalysts. The achievable STH efficiency is 22.8% for such a system. Figure 3.c shows calculated STH efficiencies for an improved system, with 0.39 eV free energy loss from each absorber of the HPE structure, using high performance non-precious metal catalysts for the HER as well as for the OER. The black triangles on these contour plots highlight the boundary associated with achieving 15% STH efficiency; appropriate band gap combinations

needed to reach this goal are found inside of the triangle. These contour plots show that there is a pathway towards achieving STH efficiency > 15% or even beyond 25% STH with the development of high-quality semiconductor absorbers and catalysts with improved kinetics. Importantly, these plots can help target ideal band gaps to use for a high efficiency PEC water splitting device. According to these calculations, the target for the wide band gap material should be 1.6-2.2 eV, depending on the band gap of the bottom absorber. The chalcopyrite materials we proposed to explore in this project fall directly within this range.

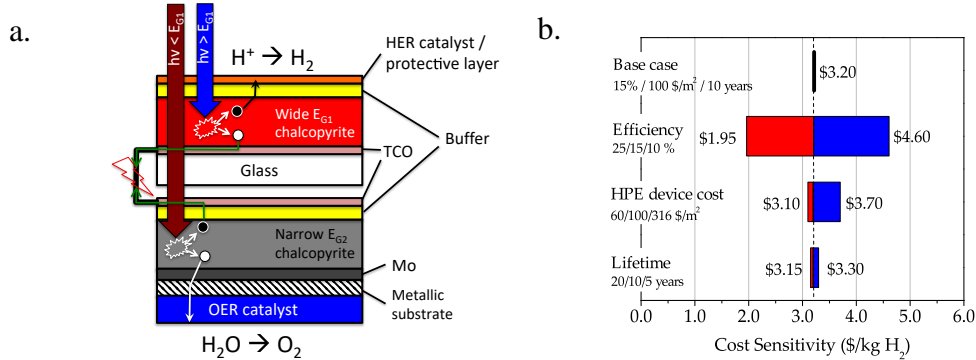


Figure 2. (a) Schematic of the proposed chalcopyrite-based HPE device. (b) Effect of efficiency, panel cost, and component lifetime on the cost of H₂ for a “Type-4” reactor. Each calculation represents the variation of a single parameter from the base case scenario.

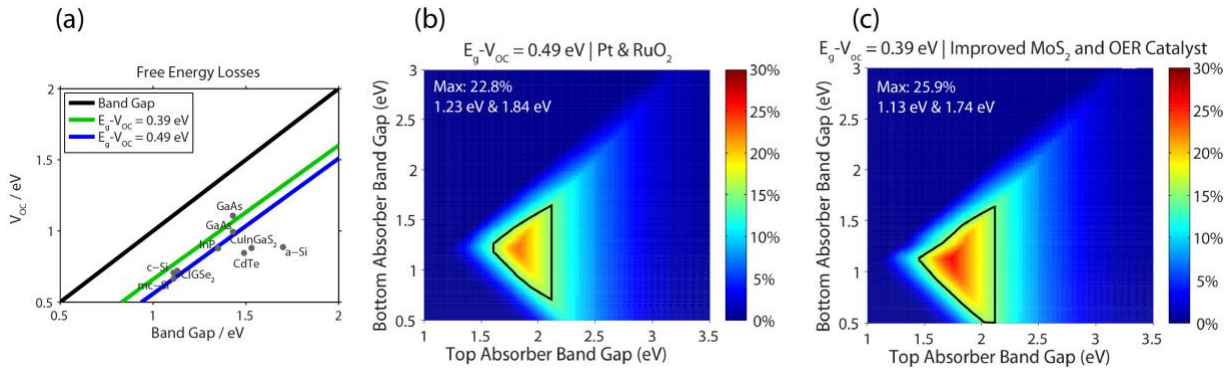


Figure 3. Achievable STH efficiencies based on (a) losses in the free energy of excited charge carriers as well as in the kinetics of HER and OER. (b,c) Contour plots showing achievable STH based on (b) commonly known semiconductors and catalysts and (c) improved semiconductors and catalysts. The black triangles demarcate the window within > 15% STH is achievable. Based on the materials investigated in this project, STH > 15% is achievable and perhaps even STH > 25%. See [11] for more details.

Techno-economic evaluation of the proposed technology. We present here our cost analysis performed with the H2A model on the proposed chalcopyrite-based HPE device. The chalcopyrite-based HPE device is integrated into a “type-4” PEC reactor consisting of a receiver containing the HPE device, a 15x solar concentrator reflector (off set parabolic reflector) to focus solar direct radiation onto the PEC cell and a solar tracking system. This analysis was done for a centralized plant equipped with Type-4 PEC reactors with a production capacity of 50 ton per day (TPD). Calculations were conducted for a “2TPD module” (sub-plant) with an operating capacity factor of 95%.¹² The panel cost (\$100/m²) and lifetime (10 years) used in the base case were derived

from DoE's ultimate target. The STH efficiency was set at 15%. The Tornado plot in Figure 2.b presents the effect of efficiency (STH), device cost, and lifetime on the cost of hydrogen. The cost per kg of H₂ for the base case was \$3.20. Decreasing the STH efficiency to 10%, a value already achieved with chalcopyrite-based PEC systems,¹⁰ increased the cost to \$4.60. Ultimately, a cost of \$1.95 was achieved with a 25% efficient device. The device cost was then altered: using projected values for dual absorber PV technologies (\$316/m²),¹² a cost of \$3.70 is found, while lowering the material cost to \$60/m² (expected manufacturing costs for chalcopyrite-based modules with roll-printing technologies)¹² reduced the production cost to \$3.10. Finally, the impact of the PEC material lifetime was assessed. Doubling the lifetime of the PEC material (20 years) compared to the base case lowered the cost by 5 cents, whereas dividing it by a factor of two (5 years) increased the cost by 10 cents. The rather low impact of the PEC material lifetime on the hydrogen production costs can be explained by a capital cost for the PEC electrode that is ten times lower than that of the concentrator and receiver. Thus, Type-4 reactors limit the burden of material photo-corrosion on the cost of hydrogen when compared to other planar designs.

b. Technical barriers

The previous section briefly discussed the relevant information that aided in identifying this project's specific technical barriers as outlined in DoE EERE's Multi-Year Research, Development, and Demonstration Plan, namely the achievable STH efficiency as well materials durability and manufacturing cost. The following list gives the four primary technical barriers which needed to be addressed in order to achieve DoE's ultimate targets for hydrogen production costs:

Barrier AE: Material Efficiency. The STH efficiency of a particular PEC device depends primarily on its solid-state and catalytic characteristics. Assuming a Faradaic efficiency of unity, the photocurrent density generated by the dual-absorber structure must be 20 mA/cm² to reach an STH efficiency of 25%. Such current density levels have so far been demonstrated only with narrow band gap semiconductors, such as silicon and chalcopyrites.⁸ Our simulations also indicate that the free energy loss in each absorber of the HPE device cannot exceed 0.49 eV. Currently, only solar cells of GaAs or Se-based chalcopyrites meet this requirement (for CuInGaSe₂: E_G=1.13 eV and open-circuit voltage V_{oc} =730 mV, leading to a loss of 0.41 eV).¹⁰ Finally, driving HER and OER at current densities relevant for high STH efficiencies infers overpotentials. Using electrocatalysts with kinetic losses larger than that of precious metal systems will lead to lower achievable STH efficiency for any given device.

Barrier AF: Material Durability. Work performed on the chalcopyrite material class by our group demonstrated hydrogen generation with a Faradaic efficiency of 85% in 0.5M sulfuric acid.⁹ Although high, this value infers that 15% of the photogenerated electrons participate in side reactions, such as photo-corrosion limiting the lifetime of the chalcopyrite material class.⁹

Barrier AG: Integrated Device Configuration. Integrating two similar or dissimilar solar absorbers into one monolithic *stacked* structure is a challenging task. Several attempts have been made in the PV community to form double junction (tandem) solar cells with chalcopyrites using TCO as an intermediate layer. Tunnel junctions were also proposed, although this approach requires absorbers with matching lattice parameters.

Barrier A1: Synthesis and Manufacturing. Our techno-economic analysis revealed that, along with STH efficiency and durability, the cost of materials greatly impacts the hydrogen production cost. Although Type-4 PEC reactors substantially reduce the capital cost associated with materials, a transition towards thin film absorbers and nanoparticle catalysts that can be manufactured at low cost is critical to achieve DoE EERE's target materials cost of 100 \$/m².

2. Work Plan

The research effort to develop practical PEC water splitting chalcopyrite systems were grouped into four principle task categories each addressing the aforementioned technical barriers: "I. Development of PV-grade wide band gap Cu(In,Ga)S₂ absorbers", "II. Sub-surface energetics improvement", "III. Surface catalysis and corrosion resistance" and "IV. Structure validation and benchmark efficiency measurement". State-of-the-art techniques in materials discovery, film synthesis, film-surface enhancement, and materials characterization were employed to facilitate the development of appropriate films for incorporation into practical PEC hydrogen-production devices. Cross-cutting characterization and theoretical modeling activities were applied to our focus material class to enhance understanding of fundamental performance parameters and expedite development of process-compatible forms of these materials. A brief description of each task is outlined below. Specific milestones and Go/NoGo metrics are provided in Table 1.

Task 1. Wide band gap chalcopyrites absorbers. Achieving *PV-grade* wide band gap chalcopyrites requires an in-depth understanding of both bulk and interfacial phenomena and their impact on the device performance. In this task, we applied extensive knowledge obtained from previous studies towards material synthesis and characterization in order to produce thin film absorbers with optical band gaps wider than 1.7 eV. Solid-state characterization were performed using cutting-edge spectroscopic techniques to pinpoint possible shortcomings. Simultaneously, theoretical modeling were used to identify possible paths towards improving material performance. The expected outcomes of this task were fully functional PEC absorber with a band gap wider than 1.7 eV, generating photocurrent density of at least 10 mA/cm² in year 1 (first Go/No-Go decision point), 12 mA/cm² in year 2, and 13 mA/cm² in year 3.

Task 2. Sub-surface energetics improvement. In this task, we used n-type "buffers" (such as CdS) to improve the surface energetics of the wide band gap chalcopyrite absorbers developed in Task 1. The electrical performances of heterojunctions were characterized by various solid-state techniques. Simultaneously, advanced surface spectroscopy analysis were used to evaluate the energetics of the junction, including X-ray and UV Photoelectron Spectroscopy (XPS and UPS), X-ray-excited Auger Electron Spectroscopy (XAES), and Inverse Photoemission Spectroscopy (IPES). We used this information to identify pitfalls occurring at the interface between the two semiconductors and determine the optimum surface energetics an "ideal" buffer should have. Theoretical modeling were performed to identify cadmium-free "buffers" with energetics compatible with wide band gap chalcopyrites. These new "buffer" materials were synthesized and integrated into PEC devices and tested. The expected outcomes of this task were a heterojunction formed by a chalcopyrite material with band gap greater than 1.7 eV and an n-type buffer with a V_{oc} of at least 600 mV in year 1, 750 mV in year 2 (second Go/No-Go decision point), and 900 mV in year 3.

Table 1. Project milestones and Go/NoGo criteria

| Task# | FY15 Milestones | Due Date | Status |
|---|---|----------|----------|
| 1 | Synthesize a CuInGaS ₂ thin film material with controlled stoichiometry & microstructure | 12/2014 | Complete |
| 2 | Fabricate Cu(In,Ga)S ₂ cells with Voc > 600 mV | 03/2015 | Complete |
| 3 | Durability > 500 hrs at 8 mA/cm ² with a chalcopyrite photoelectrode | 06/2015 | 70% |
| 4 | Chalcopyrite photoelectrode with bandgap > 1.7eV that generates at least 10-12 mA/cm ² | 09/2015 | Complete |
| Go/No-Go: Demonstrate a chalcopyrite photoelectrode with bandgap > 1.7eV that generates a photocurrent density > 10-12 mA/cm ² | | 09/2015 | Complete |
| Task# | FY16 Milestones | | |
| 1 | Cu(In,Ga)S ₂ solar cells with a conversion efficiency > 6% | 12/2015 | Complete |
| 4 | Photocurrent density relevant to 15-16% STH with chalcopyrite: 12-13 mA/cm ² | 03/2016 | Complete |
| 3 | Durability > 750 hrs at 8 mA/cm ² , with a stretch goal of 1,000 hrs | 06/2016 | 45% |
| 2 | Fabricate Cu(In,Ga)S ₂ cells with Voc > 750 mV | 09/2016 | Complete |
| Go/No-Go: Demonstrate a wide bandgap chalcopyrite-based heterojunction with an open circuit potential > 750 mV | | 09/2016 | Complete |
| Task# | FY17 Milestones | | |
| 1 | Photocurrent density relevant to 16-17% STH with a chalcopyrite: 13-14 mA/cm ² | 12/2017 | 92% |
| 2 | Fabricate Cu(In,Ga)S ₂ cells with Voc > 900 mV | 03/2018 | 94% |
| 3 | Durability > 1,000 hrs at 8 mA/cm ² , with a stretch goal of 2,000 hrs | 06/2018 | 35% |
| 4 | HPE PEC device with a standalone STH >15% generating at least 3L of H ₂ in 8 hrs. | 09/2018 | NOT MET |

Task 3. Surface catalysis and corrosion resistance. Protective surface coatings were engineered for the wide band gap chalcopyrite semiconductors using earth-abundant MoS₂. This material, synthesized by sulfurizing molybdenum metal deposited directly on top of the p-n+ junction (or on a TCO layer), provided corrosion resistance for long-term operation as well as improved surface catalysis to boost STH efficiency. The primary challenge in this project was engineering the solid-solid-interfaces appropriately to minimize charge-carrier recombination or losses in photovoltage. This task was supported by surface and interface characterization and theoretical modeling activities. Accelerated durability tests were conducted by means of cyclic voltammetry whereas long-term durability of PEC structures were assessed by chronoamperometry (current-vs-time). The expected outcomes of this task were a wide band gap chalcopyrite-based photoelectrode with lifetime of at least 500 hours in year 1, 750 hours in year 2, and 1,000 hours in year 3 at a photocurrent density greater than 8 mA/cm².

Task 4. Structure validation and benchmark efficiency measurement. all components developed in tasks 1, 2, and 3 were combined into a single photoelectrode. The highest performing photoelectrodes were integrated into complete HPE structures in year 3 with readily available state-of-the-art 1.3-1.4 eV solar cells, aiming for an STH efficiency of at least 15% by year 3. Temperature-resistant transparent conductive oxide layers were developed for monolithic device integration. Mechanical stacking was also investigated as alternative integration method. The expected outcome was a PEC reactor generating at least 3 standard liters of hydrogen in 8 hours.

3. Technical achievements in Task 1 “Wide band gap chalcopyrite absorbers”

a. Theoretical modeling

i. Chalcopyrite alloy properties

The design of optimal absorbers for photoelectrochemical hydrogen production requires tuning both the band gap for good absorption and the band offsets to facilitate the desired charge transfer. The lower band gap copper-based group-III chalcopyrites like CuInSe₂ and alloys with CuGaSe₂ (CIGSe), are conventionally used as absorbers in thin-film photovoltaics, but do not exhibit favorable band alignments for PEC hydrogen production. Alternative chalcopyrite-based materials and alloys can yield tunable band gaps and band edge positions that may make favorable large-band gap partner layers to CIGSe bottom cells in tandem devices. However, the extent to which the band gaps change, and how these changes are reflected in the ionization potentials and electron affinities is not well understood. To address these issues, we performed calculations based on density functional theory (DFT) and hybrid functionals to calculate the electronic structure in chalcopyrite-based materials, as well as to evaluate the thermodynamic stability of candidate alloys. Specifically, the calculations utilized the Heyd-Scuseria-Ernzerhof (HSE06) range-separated hybrid functional and projector-augmented wave pseudopotentials implemented in the VASP code.¹³ DFT based on conventional (semi)local exchange-correlation functionals can lead to significant underestimations of calculated band gaps in excess of 50%, making them inadequate in identifying materials with target band gaps. While much more computationally demanding, hybrid functionals incorporate a fraction of Hartree-Fock exact-exchange and lead to band gaps that are in much closer agreement with experiment, and additionally improve the calculated band edge positions relative to conventional DFT.

The chalcopyrite compounds are known to exhibit a wide range of band gaps ranging from ~1 eV for CuInSe₂ to ~3.4 eV for CuAlS₂. Using hybrid functional calculations we have evaluated the band gaps of the Cu-III-VI₂ (III=In,Ga,Al ; VI = S, Se) to establish baselines for the band gaps of the bulk constituents. This allows us to identify strategies for achieving optimal absorber band gaps through alloying on both the anion and cation sites. We include the band gaps of the Cu(In,Ga)S₂ and Cu(In,Al)Se₂ systems in Figure 4, which relies on calculated and experimental data to illustrate how the band gap and band offsets are influenced by alloying. Models for maximizing the solar-to-hydrogen efficiency in dual-absorber hybrid photoelectrode have predicted a target band gap of ~1.8 eV for the larger absorber, larger than for pure CuInS₂ (1.53 eV) or CuInSe₂ (1.04 eV) and smaller than pure CuGaS₂ (2.43 eV) or CuAlSe₂ (2.67 eV). The results from Figure 4 show that incorporating ~40% Ga into Cu(In,Ga)S₂ or ~60% Al into Cu(In,Al)Se₂ leads to an optimal large-band gap partner for the lower-gap choice (i.e. Cu(In,Ga)Se₂). Nonlinearities in the band gap with alloy concentration, so-called band gap bowing, are expected to be a relatively weak effect in Cu(In,Ga)S₂ alloys and more pronounced in the more size mismatched Cu(In,Al)Se₂ alloys. In addition to alloying in the group-III site, we also explored alloys on the group-VI site (e.g. S and Se alloys), as well as alloying Ag and Cu.

Extensions to B-containing chalcopyrites were also pursued, as the previously reported optical band gaps of 3.61 eV (3.13 eV) for CuBS₂ (CuBSe₂)¹⁴ suggested that only modest amounts of B could increase the band gap to target values. Our initial calculations with hybrid functionals identified both the sulfide and selenide exhibit large direct band gaps in good agreement with

experimental reports. However, we identified that the B-containing CuBS₂ and CuBSe₂ compounds exhibit smaller fundamental band gaps than previously assumed from experimental measurements of the optical band gaps. Our results on the optical spectra of these compounds identified a very weak absorption onset and that the fundamental band gaps are actually much smaller than the optical gaps. Our results using the state-of-the-art first-principles methods such as the *GoWo* approximation confirmed this and identified a fundamental gap of 2.86 eV for CuBS₂ and 2.29 eV for CuBSe₂, roughly 0.8 eV lower than the reported optical band gaps. This resulted in our calculations identifying that the conduction band edges of the B-containing chalcopyrites are much closer to the Ga-containing analogs. The magnitude of the absorption offset is likely decreased in the alloys due to the resulting changes in the valence band electronic structure, further decreasing the blue-shift expected for B-containing alloys. Combined with the relative thermodynamic difficulty in incorporating B into Cu-III-(S,Se)₂ alloys, this suggests B-containing alloys may be much more difficult to realize than other alloys via traditional synthesis approaches.

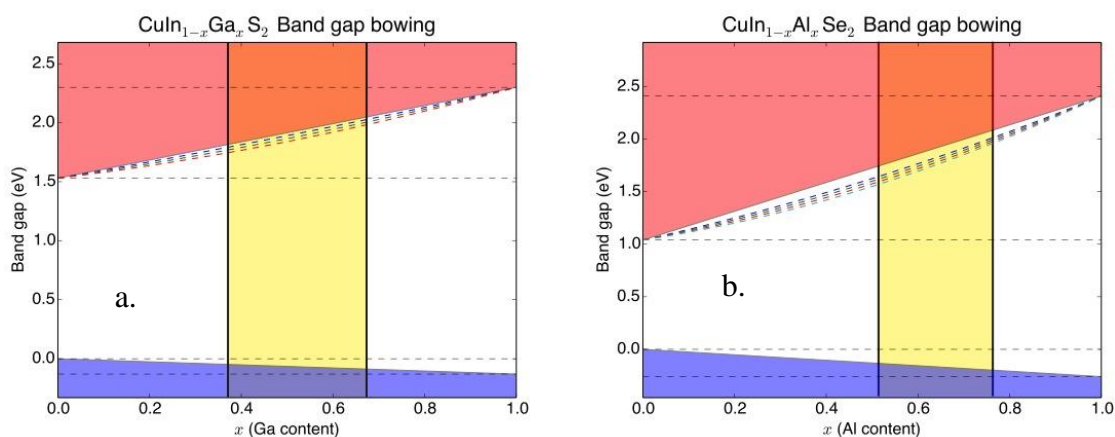


Figure 4. Band gap and calculated natural band offsets of (a) the Cu(In,Ga)S₂ system as a function of the Ga content and (b) the Cu(In,Al)Se₂ system as a function of Al content. The values of the pure compounds are linearly interpolated (black solid line) and a range of the experimentally reported bowing parameters are included as the colored dashed lines. The yellow region indicates compositions that exhibit band gaps in the range of ~1.8-2.0 eV desirable for PEC hydrogen production.

ii. Chalcopyrite/buffer band alignment

The development of a functional PEC device relies on the ability to efficiently separate and transfer photo-generated carriers to the catalytically-active surface. Engineering optimal absorber and buffer partners for heterostructures that facilitate the charge transfer is therefore of the highest priority. This process is analogous to engineering high-efficiency thin-film solar cells, where the best performing Cu(In,Ga)Se₂-based devices typically employ CdS buffer layers due to a favorable conduction band offset and *n*-type conductivity. We identified that this advantage to the low-gap Cu(In,Ga)Se₂ absorber is unfavorable for the larger-gap sulfide alloys as a consequence of how the band offsets change with composition. This is illustrated in Figure 5, which shows how the calculated band offsets of CdS relative to the bulk chalcopyrites. While 1.0 eV CuInSe₂ and 1.5 eV CuInS₂ have a moderate conduction band offset (CBO) with CdS, a significant “cliff” is expected at the interface formed by 1.6 eV CuGaSe₂ with CdS. A similar issue is likely to happen with wide band gap CuInGaS₂ and CdS.

Our results identify that the influence of Al incorporation, like Ga, is to primarily raise the conduction band of CuInSe₂ or CuInS₂. The degree that Al influences the conduction band position on an absolute energy scale and the resulting band offset with the buffer is expected to be more significant than for Ga due to the larger band gap variations between the parent compounds (2.65 eV for CuAlSe₂ vs 1.68 eV for CuGaSe₂), and offers alternative compositions to Cu(In,Ga)S₂ alloys for targeting the desired 1.8-2.0 eV absorber band gap of PEC materials. We also identify that despite an unfavorably large conduction band offset for ZnS buffers in CIGSe devices, some Zn incorporation into CdS may provide optimal band alignments for CIGS or CIGAS absorbers in PEC devices. Specifically, CdZnS buffer layers with compositions in the vicinity of 50% Zn were identified as more favorable partners for the higher-gap absorbers having optimal band alignment (CBO = 0 eV) with 1.8-2.0 eV chalcopyrite PEC materials.

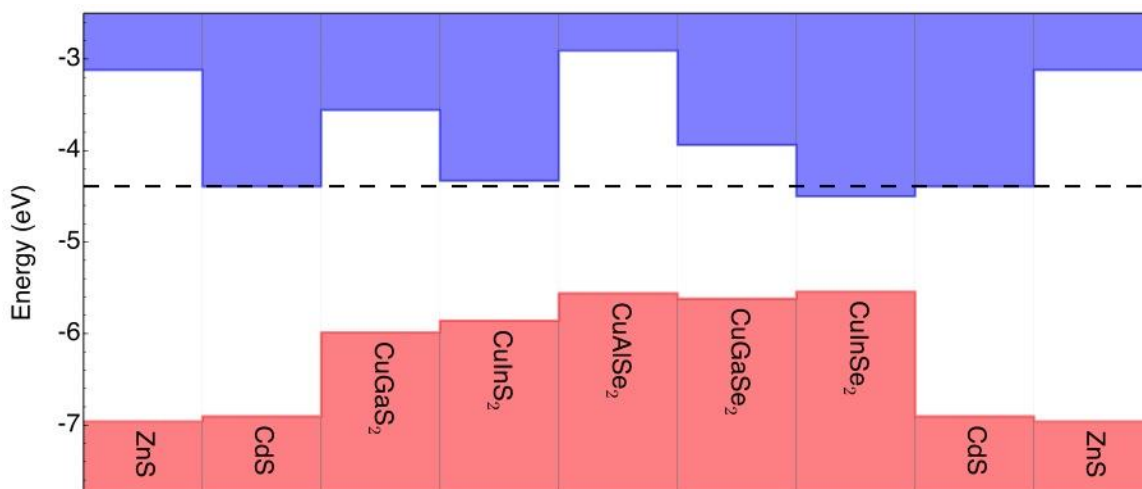


Figure 5. Calculated unstrained band offsets of CdS and ZnS with respect to bulk CuGaS₂, CuInS₂, CuGaSe₂, CuInSe₂ and CuAlSe₂. CdS exhibits a favorable conduction band offset with low-Ga content CIGSe alloys, while it is expected to lead to unfavorable conduction band offsets for the sulfide chalcopyrites. ZnS exhibits large conduction band offsets for CIGSe, but may be a good candidate for alloying with CdS to tune the buffer band edges.

iii. Chalcopyrite absorbers band gaps, thermodynamic stability, and defect tolerance

To better inform the experimental synthesis of desirable alloys, we have focused on assessing the band gap and thermodynamic stability of absorber alloys as function of composition and also begun calculations to characterize how point defects may influence the resulting properties of the alloys. We spent considerable attention on the CGSSe alloys to supplement the experimental efforts and summarize the calculated band gap and stability as a function of S content in Figure 6.a. We find that these alloys are readily mixed to form solid solutions and are stable against phase separation at modest processing temperatures (Figure 6.b). Additionally, CGSSe alloys exhibit band gaps within the target range of ~1.8-2 eV for S-contents ranging from ~20-40%, with a nearly linear dependence on composition. Additional calculations on Cu(In,Ga)S₂ (CIGS) alloys identify that the band gap of these alloys display a slightly more nonlinear behavior with composition than in the CGSSe alloys. This is evident in our calculated band gap bowing parameter of 0.05 eV, as seen in Figure 6.a, compared to the 0.2 eV calculated for CIGS alloys.

We also evaluated the solubilities and electronic character of native and extrinsic defects in pure CGSe and CGS. Due to the complexity of the chalcopyrite materials, there are a large number of competing secondary phases that define regions in the phase diagram (i.e. Cu-poor, Ga-rich, Se-poor, etc.) that can drastically influence resulting defect concentrations. Additionally the role of disorder (e.g. antisites) are important features in assessing the quality of chalcopyrite materials. We focused on assessing the stability of defects with deep states like the Ga_{Cu} deep donors that have previously been suggested to play a role in limiting the performance of high-Ga CIGSe photovoltaics as either isolated defects or when complexed with Cu vacancies.¹⁵ In Figure 6.c we include the deep levels associated with this defect in both CGSe and CGS and find that they are deeper in the CGS band gap by ~ 0.5 eV relative to CGSe. Our results identified that these defects exhibit localized states within the band gap that are quite similar on an absolute energy scale between the sulfide and selenide parent phases. Most importantly, the results highlight that these antisites may also be problematic for pinning the Fermi level if their concentrations are high enough, as would be expected for more Cu-poor and Ga-rich growth conditions. This type of analysis was important feedback for the experimental efforts to identify favorable synthesis conditions that mitigate detrimental defect populations.

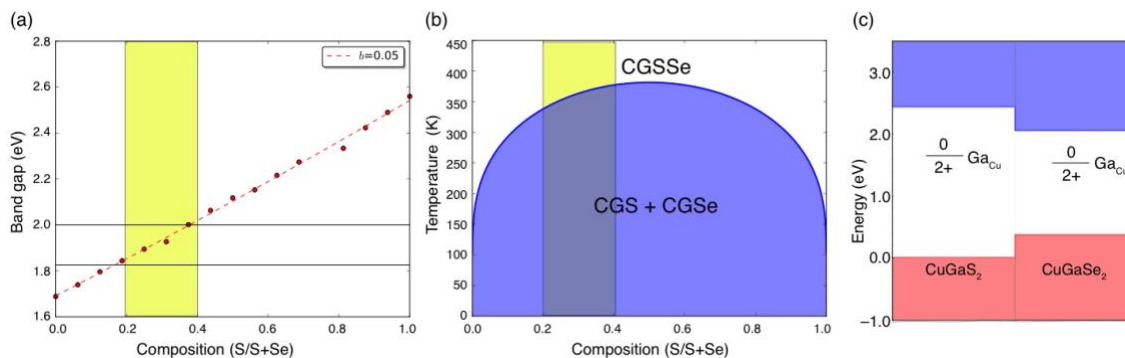


Figure 6. (a) Calculated band gap and (b) thermodynamic stability of $\text{CuGa}(\text{S},\text{Se})_2$ alloys as a function of composition. The target band gap for an optimal top cell partner of 1.8-2.0 eV is denoted by black lines in (a), where we also highlight that alloys with ~ 20 -40% S may yield the desired properties. (c) Defect levels associated with Ga_{Cu} antisites shown relative to the band edge positions in the parent CuGaS_2 and CuGaSe_2 compounds. These defects are believed to be problematic recombination centers conventional high-Ga $\text{Cu}(\text{In},\text{Ga})\text{Se}_2$ photovoltaics and may also limit the performance of $\text{CuGa}(\text{S},\text{Se})_2$ absorbers.

b. Wide band gap CuGa_3Se_5 absorbers

i. Effects of Cu/Ga composition on wide band gap chalcopyrite films

In this task, we explored ordered vacancy compounds CuGa_3Se_5 chalcopyrites as new materials candidates for PEC water splitting. The Cu/Ga composition of co-evaporated films was varied from 0.31 to 0.66, as measured by XRF. XRD showed that films with Cu/Ga of 0.66, 0.52, and 0.36 had single-phase CuGaSe_2 , two-phase $\text{CuGaSe}_2 + \text{CuGa}_3\text{Se}_5$, and single-phase CuGa_3Se_5 , respectively, similar to previous reports.¹⁶ PV devices fabricated with these absorbers had poor power conversion efficiencies ($\leq 3.7\%$), relative to absorbers typically used for PV (Cu/Ga > 0.7). Widening the band gap of CuGaSe_2 by moving to more Cu-poor compositions actually decreases open-circuit voltage and fill factor, making films with Cu/Ga < 0.7 unattractive for PV applications. On the other hand, the performance of the bare CuGa_3Se_5 PEC photocathodes was

particularly good compared to previous reports,¹⁷ despite the absence of both buffer layers (e.g. CdS) and catalyst layers (e.g. Pt). The source of this superior performance is the subject of ongoing investigation. Figure 7 shows the best LSV curves at different Cu/Ga compositions (3 electrode configuration in 0.5 M H₂SO₄ electrolyte). In chalcopyrite compounds such as CuGaSe₂, the repulsion of Cu *d* and Se *p* orbitals is known to shift the valence band to higher energies.¹⁸ Therefore, reducing the Cu/Ga composition from 1 to 0.33 (CuGaSe₂ to CuGa₃Se₅) reduces the valence band energy by 0.2 eV. Thus, the band gap is expected to vary from 1.65 eV to 1.86 eV for Cu/Ga of 1 to 0.33,¹⁹ which explains the trend of decreased saturated photocurrent density (*J*_{SAT}) with decreased Cu/Ga composition. Throughout this work the *J*_{SAT} is taken as the light current density minus the dark current density at -1 V vs. RHE.

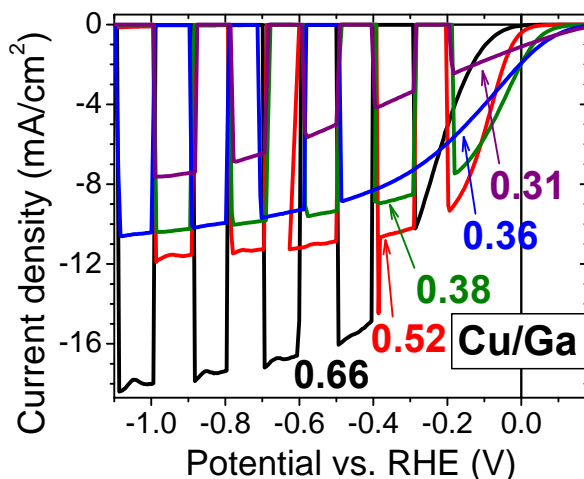


Figure 7. LSV data for Cu-Ga-Se photocathodes with Cu/Ga compositions of 0.66 (black), 0.52 (red), 0.38 (green), 0.36 (blue), and 0.31 (purple).

The incident photon-to-electron conversion efficiency (IPCE) long wavelength cutoffs followed a similar trend with the *J*_{SAT} in LSV measurements. The long wavelength drop in IPCE data was used to extrapolate effective band gaps on a logarithmic scale, where this effective band gap contains optical and electronic information. The transmittance of a CuGa₃Se₅ film on bare soda-lime glass was also measured, and the band gap calculated from the Tauc plot was in good agreement with effective values from IPCE. For each absorber, the *J*_{SAT} and the IPCE effective band gap were plotted against Cu/Ga in Figure 8, illustrating the trade-off between band gap and *J*_{SAT}.

The shelf life of a PEC device with Cu/Ga of 0.66 was examined by measuring LSV initially, after 4 months and after 9 months of storage in air (Figure 9). The PEC performance was effectively unchanged by aging, or even slightly improved. This result was unexpected, as the PV properties of bare chalcopyrite absorbers deteriorate rapidly in air, and even when stored under N₂.²⁰ This result indicates that the PEC properties of Cu-poor Cu-Ga-Se films could be recovered during operation, even though the absorber has been stored in humid air for a long period of time. It is speculated that the acidic electrolyte dissolves oxidation products, similar to the way potassium cyanide etches unwanted phases from chalcopyrite surfaces before device fabrication.¹⁶

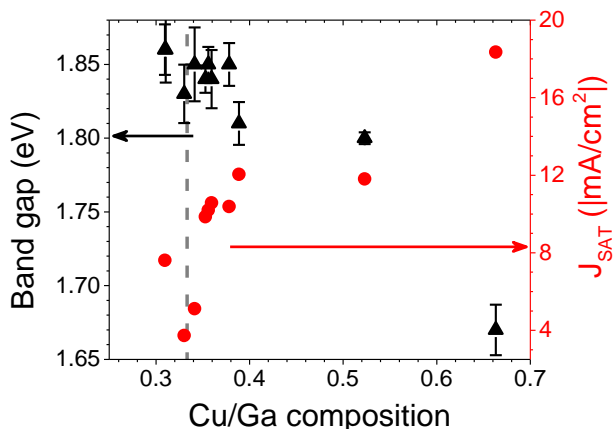


Figure 8. Effective band gap extracted from IPCE data (left axis) and saturated photocurrent density (J_{SAT} at -1 V vs. RHE; right axis) for Cu-Ga-Se photocathodes as a function of Cu/Ga composition. The dashed line represents stoichiometric $CuGa_3Se_5$.

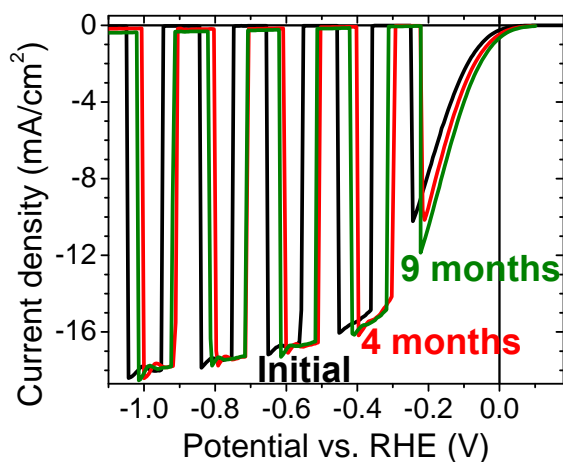


Figure 9. Initial (black), 4 months aged (red), and 9 months aged (green) LSV data for a Cu-Ga-Se photocathode with Cu/Ga of 0.66.

While the shelf life result in Figure 9 is promising, it is no substitute for continuous water splitting in reactive electrolyte. Continuous galvanostatic testing was therefore carried out at 1 sun and 8 mA/cm^2 for photocathodes with Cu/Ga compositions of 0.66, 0.52 and 0.36. The J_{SAT} (light minus dark current) and dark current density at -1.0 V vs. RHE were plotted against time for the three photocathodes in Figure 10. For all three samples, degradation in photocurrent roughly coincided with increased dark current—a possible indication of shunting, which could be due to pinhole formation or a phase transformation producing conductive material. Relative to the near-stoichiometric $CuGa_3Se_5$, the films with higher Cu/Ga of 0.66 and 0.52 both showed faster photocurrent degradation. These films both contained $CuGaSe_2$, which may degrade faster than $CuGa_3Se_5$, as a previous study linked Cu^+/Cu_2^+ dissolution/re-adsorption to the degradation of $Cu(In,Ga)Se_2$ PEC films.²¹ Films with lower Cu concentrations are therefore speculated to produce Cu^+ at a lower rate, and degrade slower as a result. More study will be needed to confirm this connection. On the other hand, the film with Cu/Ga of 0.36 only exhibited $CuGa_3Se_5$ by XRD, and evolved H_2 continuously for 17 days at 11.7 mA/cm^2 , equivalent to $\sim 17200 C/cm^2$, the most

durable PEC result for any polycrystalline absorber.²² For comparison, the previous world records¹⁰ for polycrystalline PEC durability used more complex (Ag,Cu)GaSe₂/CuGa₃Se₅/CdS/Pt and CIGS/CdS/Ti/Mo/Pt architectures and achieved 20 days at ~7.5 mA/cm² (13000 C/cm²)²³ and 10 days at ~19.5 mA/cm² (16900 C/cm²),²⁴ respectively. The present water splitting performance/durability result is important, as the present work did not employ a catalyst or buffer layer, and used a wider band gap absorber material (1.86 eV), which is better suited to tandem device implementation for commercially viable solar-to-hydrogen efficiencies.

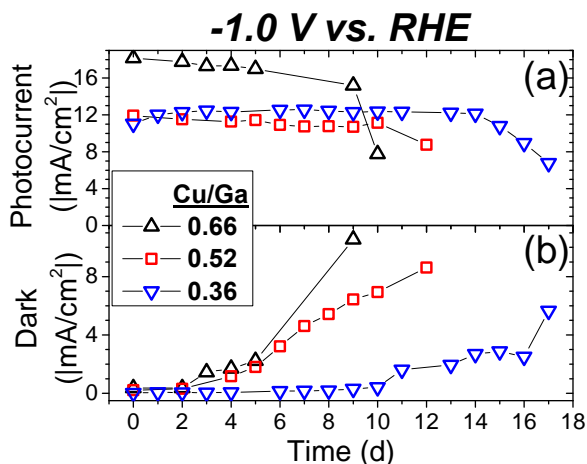


Figure 10. (a) Photocurrent (light minus dark current density) and (b) dark current density from LSV data at -1 V vs. RHE as a function of continuous galvanostatic testing time for Cu-Ga-Se films with Cu/Ga compositions of 0.66 (black up triangles), 0.52 (red squares), and 0.36 (blue down triangles).

ii. Resistivity of CuGa₃Se₅

In order to build on these initial successes, a better understanding of the device physics is needed. To this end, the resistivity of Cu(Ga,In)₃Se₅ materials was studied. Cu(Ga,In)₃Se₅ films are generally understood to be more resistive than Cu(In,Ga)Se₂, presumably due to increased compensation by (Ga,In)_{Cu} donor defects. However, the effects of out-diffused alkali metals from the glass substrates are not well studied. Therefore, single stage CuGa₃Se₅, CuIn₃Se₅, and 3-stage CuGa₃Se₅ were grown on 3 different glasses: soda-lime glass (high Na), Schott D263 borosilicate glass (high K), and Schott borofloat glass (no alkali metal). Ohmic contacts were formed by ultrasonic soldering of In. The in-plane resistivity values are shown in Figure 11. The resistivity was decreased by using the 3-stage process, and by out-diffusing alkali metals. For soda-lime glass, the 3-stage process reduced resistivity by ~2 orders of magnitude, so different absorber thicknesses should be used to minimize resistive losses while avoiding pinholes. CuIn₃Se₅ had lower resistivity than CuGa₃Se₅, and Na appeared to increase CuIn₃Se₅ resistivity, an unexpected result that, if reproduced, could help clarify the alkali metals' effects on resistivity. Only the 3-stage CuGa₃Se₅ sample grown on soda-lime glass (SLG) had low enough resistivity for Hall measurements: it had a resistivity of 1800 Ω.cm, a mobility of 4.5 cm² V⁻¹.s⁻¹, and a carrier concentration of 7.9x10¹⁴ cm⁻³. This was in good agreement with the 2-probe current-voltage resistivity measurement on the 3-stage CuGa₃Se₅ on SLG sample (~1000 Ω.cm). Unfortunately, the carrier type determination was unreliable due to the small magnitude of the Hall voltage. It is concluded that the carrier type of these materials is difficult to access experimentally, but doping should be carefully controlled to further improve water splitting performance.

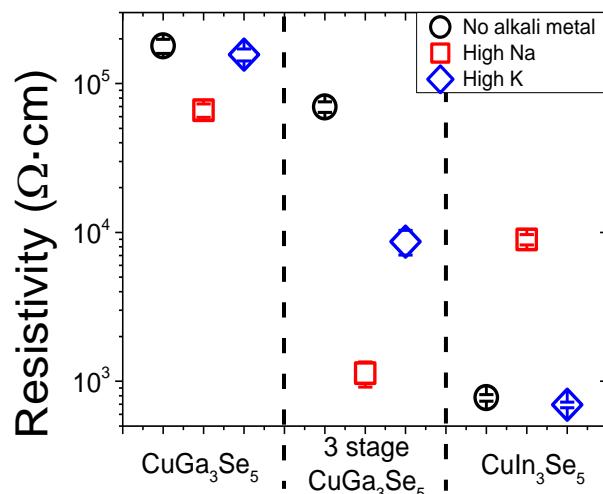


Figure 11. In-plane resistivity of Cu(Ga,In)₃Se₅ films grown on glass substrates with different alkali metal content.

iii. Improved CuGa₃Se₅ solar cell open-circuit voltages

Quasi-Fermi level splitting determines both water splitting and photovoltaic efficiency, so methods for improving V_{oc} of CuGa₃Se₅ solar cells were explored as a means to improve PEC. First, air annealing (2 min, 170 °C) of complete solar cell stacks (glass/Mo/CuGa₃Se₅/CdS/i-ZnO/Al:ZnO/metal grids) was used to improve V_{oc} by 10 – 30 mV. This is a technique previously used in narrow band gap CIGSe, and is not well understood, but could relate to oxygen-induced passivation.²⁵ Next, light soaking (10 min under 1 sun) was used to improve V_{oc} by 0 – 25 mV. This is another phenomenon observed in narrow band gap CIGSe that is related metastable defects. These processing changes combined with potassium doping improved V_{oc} from its baseline of 725 mV up to 848 mV for 1.8 eV band gap absorbers.

iv. Transparent devices for tandem top cells

Throughout this project, standard glass/Mo substrates were used for co-evaporated wide band gap CuGa₃Se₅ PEC photocathodes. The next step toward competitive H₂ production is to implement these absorbers on transparent substrates so they can act as top cells in tandem devices, and reach solar-to-hydrogen efficiencies >10%. Transparent conductive fluorine-doped tin oxide (FTO) back contacts were chosen, as they have been demonstrated as promising substrates for bifacial narrow band gap Cu(In,Ga)Se₂ photovoltaic devices.²⁶ In particular, TEC glass from Pilkington was used, which consists of a soda-lime glass/diffusion barrier/FTO stack. As seen in the black curves of Figure 12, photovoltaic (PV) and PEC devices both showed very poor performance when standard 3-stage CuGa₃Se₅ absorbers were grown on these substrates. This is partially a result of the diffusion barrier, which blocks Na from diffusing out from the substrate during absorber growth, where Na is required to enhance the absorber's carrier concentration (Section 3.b.ii). To correct this, extrinsic NaF was introduced: 10 nm of NaF was evaporated before and after CuGa₃Se₅ co-evaporation, and different behavior was observed for each. Pre-deposited NaF (blue) had better short-circuit current density (Figure 12.a)/saturated photocurrent density (Figure 12.b), and worse open-circuit voltage (Figure 12.a)/turn-on voltage (Figure 12.b), relative to post-deposited NaF

(red). Thus, the transparent PV devices with CdS buffers and ZnO contacts had the same trend as the bare FTO/CuGa₃Se₅ PEC photocathodes. This current-voltage tradeoff may be useful in pairing the top cell with a bottom cell. Overall, the transparent PEC photocathodes did not suffer much loss relative to the baseline Mo back contacts (Section 3.b.i), which is very promising for tandem device efficiency.

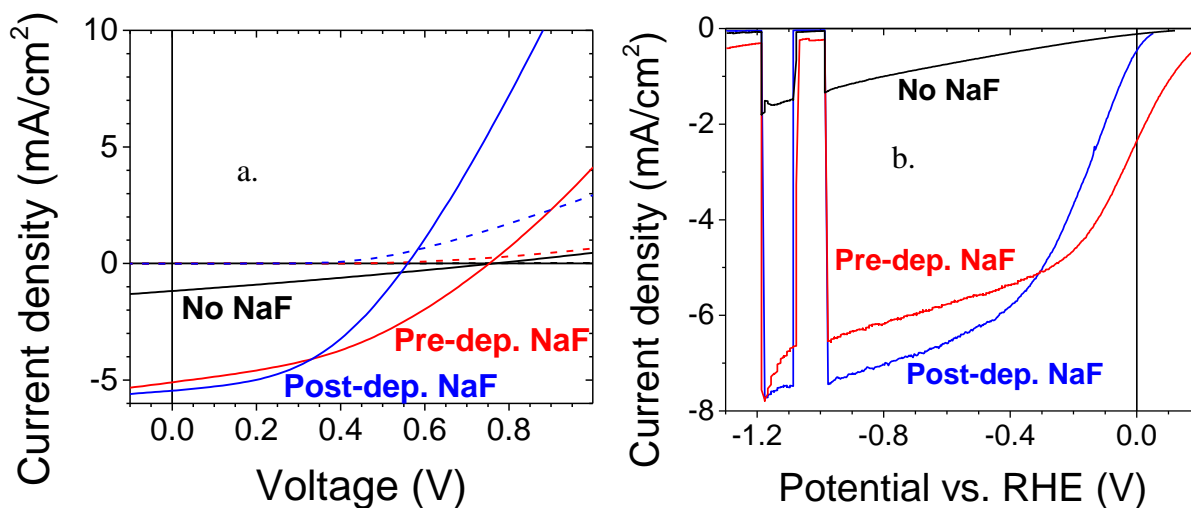


Figure 12. (a) Current density-voltage characteristics of transparent SLG/FTO/CuGa₃Se₅/CdS/ZnO solar cells and (b) chopped light current-voltage characteristics of transparent SLG/FTO/CuGa₃Se₅ PEC photocathodes with no NaF introduced (black), 10 nm NaF deposited before the absorber (red), and 10 nm NaF deposited after the absorber (blue). The PV and PEC devices show similar trends.

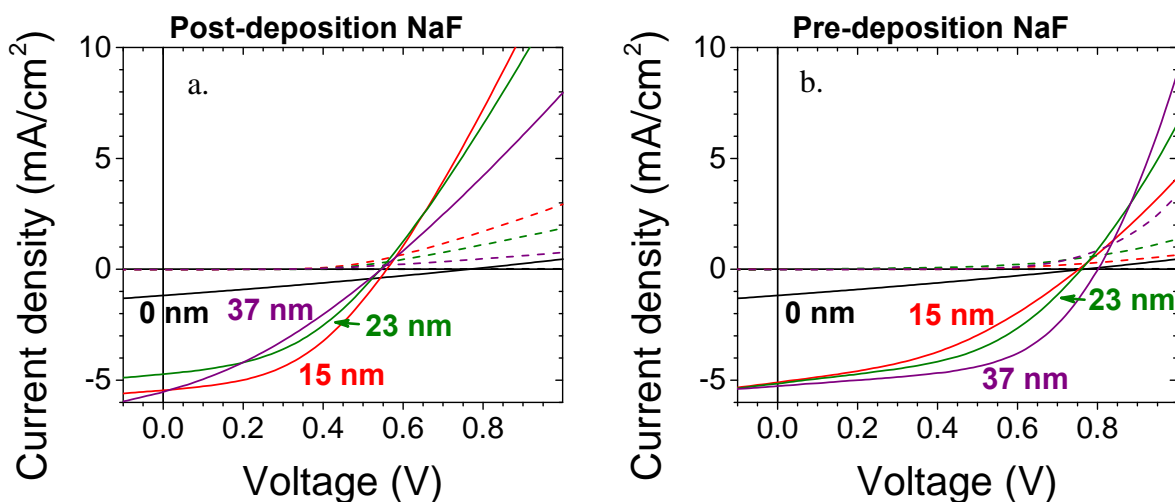


Figure 13. Light (solid) and dark (dashed) current density-voltage characteristics of transparent solar cells (glass/FTO/CuGa₃Se₅/CdS/ZnO/grids) with different thicknesses of NaF evaporated (a) after and (b) before the absorber.

Transparent solar cells were also fabricated with varied extrinsic doping levels. The post-deposition NaF treatments of every thickness led to inferior open-circuit voltages (Figure 13.a). This indicates that the NaF crystals on the absorber surface should be rinsed before CdS buffer

deposition. On the other hand, the pre-deposited NaF thickness correlated with improved open-circuit voltage and fill factor, culminating in 801 mV for the 37 nm device. The dark and light current-voltage characteristics in Figure 13.b indicate that the improvements were from reduced series resistance. This result exceeded the 800 mV milestone, only with a transparent device grown at 100 °C lower temperature (500 °C)—promising results for implementation in tandem top cells.

v. Conclusions

The prospect of adapting chalcopyrite-based thin film PV absorbers to PEC water splitting devices was explored. In particular, the suitability of Cu-Ga-Se absorber films for H₂ evolution was examined at Cu/Ga compositions of 0.31 to 0.66. These compositions had poor PV performance, but exhibited PEC performance that was superior to previous reports, despite the absence of buffer or catalyst surface layers. Decreasing Cu/Ga composition increased the effective band gap (determined from IPCE cutoff), resulting in a decrease in saturated photocurrent density, as expected. The photocathodes showed excellent shelf-life, where PEC performance was unchanged after 9 months of storage in air. More importantly, a bare CuGa₃Se₅ film with a band gap of 1.86 eV exhibited remarkable operando durability, achieving 17 d of continuous water splitting (~12 mA/cm² at -1 V vs. RHE). This is equivalent to ~17200 C/cm², which is a world record for any polycrystalline PEC absorber. The results also suggest that Cu content plays a strong role in degradation, since the greatest durability was found for the film with the lowest Cu/Ga composition. Increasing dark current coincided with degradation, so the formation of shunts or pinholes are possible degradation mechanisms. Routes for further improving performance were also explored: resistivity was decreased by growing with a 3-stage co-evaporation process and adding alkali metal dopants, air annealing and light soaking processes led to improved open-circuit voltages in solar cells (up to 848 mV), and absorbers were grown directly onto F:SnO₂ contacts to maintain good water splitting performance in transparent devices that can operate as tandem top cells. The present work demonstrates that CuGa₃Se₅ is a promising wide band gap candidate for top cell photocathodes in tandem water splitting devices. Further work to improve surface energetics and reduce Cu dissolution will be critical to achieving low-cost, efficient and durable PEC H₂ production.

c. Wide band gap CuGa(S,Se)₂ absorbers

i. Overview

The purpose of this work was to explore the capabilities of CuGa(S,Se)₂ as a wide-E_g top cell absorber for PEC water splitting. To fully assess a top cell absorber candidate for PEC water splitting, a transparent conductive back contact is mandatory to allow measurement of both PEC performance and light transmittance. As we learned throughout the course of this study though, synthesizing CuGa(S,Se)₂ films on transparent conductive fluorinated tin oxide (FTO) substrates easily degrades the optoelectronic properties of the FTO unless specific synthesis conditions were used. Thus the following report is broken into two parts. Section 3.c.ii details the process of discovering an annealing method that preserved the optoelectronic properties of the substrate. Section 3.c.iii reports the PEC properties that we obtained from functional E_g-tunable CuGa(S,Se)₂ photocathodes, made possible by the annealing method used in section ii).

ii. Development of Functional EG-tunable CuGa(S,Se)₂ Photocathodes

We started our study by determining if the E_G of our CuGaSe₂ precursor films deposited on SLG substrates could be increased (thus indicating sulfur incorporation into the film) using the one-step sulfoselenization annealing (550 °C, 25 mg sulfur, 0-75 mg selenium). Precursors on SLG substrates were 500 nm thick. The absorption coefficient of an as-deposited Cu-rich CuGaSe₂ precursor as well as several sulfoselenized Cu-rich samples are plotted in Figure 14.a along with an optical image of the corresponding samples in Figure 14.b. The samples were KCN-etched after sulfoselenization to remove any copper sulfide and/or copper selenide phases. As seen in Figure 14.a, the etched Cu-rich CuGaSe₂ exhibited a E_G of 1.66 eV, consistent with literature values.²⁷ When only sulfur was used during the annealing, the highest E_G of 2.38 eV was obtained, which is consistent with reported values for CuGaS₂.²⁸ Since sulfur-containing chalcopyrites always have higher band gaps than their selenium containing counterparts (e.g. CuInSe₂ (1.0 eV) vs CuInS₂ (1.5 eV)),²⁹ the increase in E_G as the ratio of sulfur-to-selenium (S/Se) mass ratio used during annealing increases suggests that the sulfoselenization process has successfully replaced part or all selenium in CuGaSe₂ with sulfur to form CuGa(S,Se)₂.

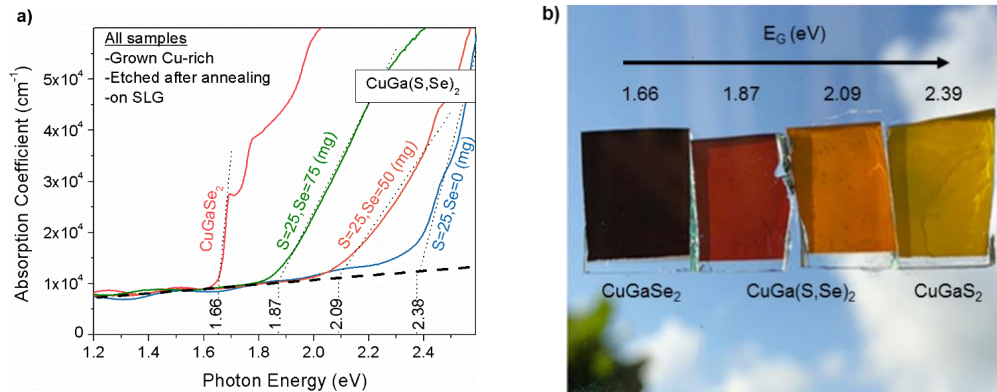


Figure 14. (a) Plot of absorption coefficient of a CuGaSe₂ and several sulfoselenized samples showing that the E_G increases as the S/Se mass ratio used for the annealing step increases. This trend suggests that CuGaSe₂ is successfully being converted to CuGa(S,Se)₂. (b) Corresponding CuGa(S,Se)₂ samples.

To further support the claim that sulfur substitution has occurred, we performed XRD on the samples of Figure 14, the data of which is plotted in Figure 15.a. Full spectrum scans ($20^\circ < 2\theta < 74^\circ$) of an as-deposited CuGaSe₂, a KCN-etched CuGaSe₂, and a sulfurized CuGaSe₂ converted into CuGaS₂ can be seen in figure Figure 15.b. We observed that as the S/Se mass ratio increased, the peak associated with the (112) plane of the chalcopyrite structure shifted to higher 2θ values. This trend can be explained by Bragg's law, which states that the lattice spacing of a crystal plane and 2θ are inversely proportional. As the smaller sulfur atoms replace selenium in the chalcopyrite lattice, the lattice spacing decreases and as a result the 2θ value of the (112) peak position shifts to higher angles. Thus, the shifting of the (112) peak to higher 2θ values, seen in Figure 15.a, supports the claim that sulfur substitution has occurred. All peaks in Figure 15.a had a similar width and shape except for the sample that was annealed in a 25/50 S/Se mass ratio ($E_G = 2.09$ eV), which was approximately twice as broad as the others. This broadness suggests that there is not a dominant compositional ratio of S/Se in this sample, but rather a spread of compositional ratios, which may also explain why the slope of the absorption coefficient of the 25/50 S/Se sample, seen in Figure 14.a, is lower than the other samples.

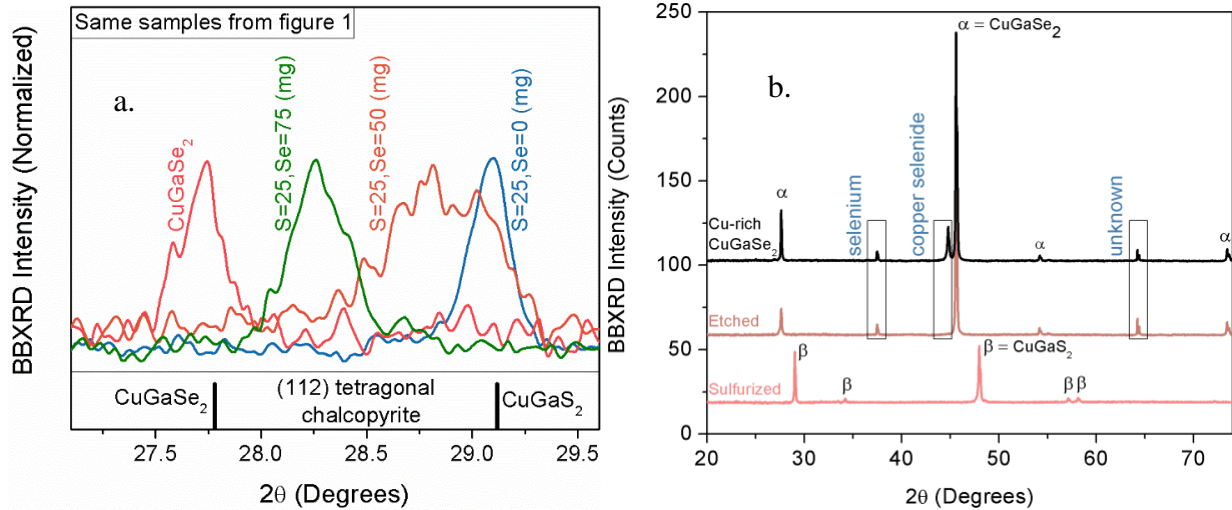


Figure 15. (a) Normalized XRD measured on the samples of Figure 14. The peak of the (112) plane shifts closer to the CuGaSe₂ reference as the S/Se mass ratio increases, suggesting that CuGaSe₂ converts to CuGa(S,Se)₂. (b) Bragg-Brentano XRD scans probing the bulk of a Cu-rich CuGaSe₂ sample before etching (top), after etching (middle), and after sulfurization (bottom). All phases closely matched to either CuGaSe₂ (Powder Diffraction File, 035-1100), selenium (PDF 00-054-0500), copper selenide (PDF 027-1131), or CuGaS₂ (PDF 025-0279) except for two unknown peaks at 64.24 and 64.40 degrees, which did not match any combination of copper, gallium, selenium, oxygen, and sodium.

It should be noted that the trends of Figure 14 and Figure 15 only apply to Cu-rich samples. The one-step sulfoselenization was not effective at increasing the E_G nor the 2θ values of the XRD peaks of Cu-poor samples, as seen in Figure 16. Difficulty in sulfurizing Cu-poor chalcopyrites was expected, however, since other groups have also reported negligible shifts in their XRD measurements after attempting to sulfurize Cu-poor chalcopyrites.³⁰

While the one-step sulfoselenization worked well on SLG substrates, when applied to precursors on FTO substrates, the resistance of the FTO would increase by several orders of magnitude, from $10^1 \Omega$ to $10^5 \Omega$ as measured with a digital multimeter. This increase in resistance was presumably caused by the reaction of FTO and sulfur into tin sulfide, the resistivity of which has been shown to vary between 10^1 - $10^4 \Omega \cdot \text{cm}$ depending on the particular phase.³¹ The resulting CuGa(S,Se)₂ electrodes would output negligible photocurrent (LSV not shown). The inability of the one-step sulfoselenization process to simultaneously convert CuGaSe₂ precursors into CuGa(S,Se)₂ and keep the underlying FTO conductive led to the development of a two-step annealing in which the first step was a sulfurization at low temperature and the second step was an annealing at high temperature in an inert environment. To demonstrate this process, a 1.2 μm -thick Cu-rich CuGaSe₂ precursor on FTO and a bare FTO substrate (control sample) were first sulfurized at 300 °C for 60 minutes with 1.6 mg of sulfur. In the second step, the samples were annealed in nitrogen (without sulfur) at 500 °C for 10 minutes. UV-Vis and BBRD measurements were used to track the formation of CuGa(S,Se)₂, and 4-point probe measurements were performed on the bare FTO to track changes in resistivity. Upon visible inspection after the first annealing step in sulfur, the surface of the sulfurized chalcopyrite sample appeared to have changed color from green-blue to dark-blue. Despite this color change, neither the E_G nor the XRD pattern changed significantly, as seen in Figure 17.a and Figure 17.b. Only after the second sulfur-free annealing step at 500 °C did we observe both an increase in the E_G , to 1.91 eV, as well as a shift in the 2θ value of the XRD

(112) chalcopyrite peak, from 27.73 to 28.36°, also shown in Figure 17.a and Figure 17.b, respectively. The 4-point probe resistivity of the FTO control before and after the entire two-step annealing remained at 15 Ω /sq. ($\pm 5\%$). Thus, breaking up the annealing into two steps – a low-temperature sulfurization followed by high-temperature inert annealing – was effective at forming $\text{CuGa}(\text{S},\text{Se})_2$ from our precursors while at the same time preventing the FTO resistance from increasing.

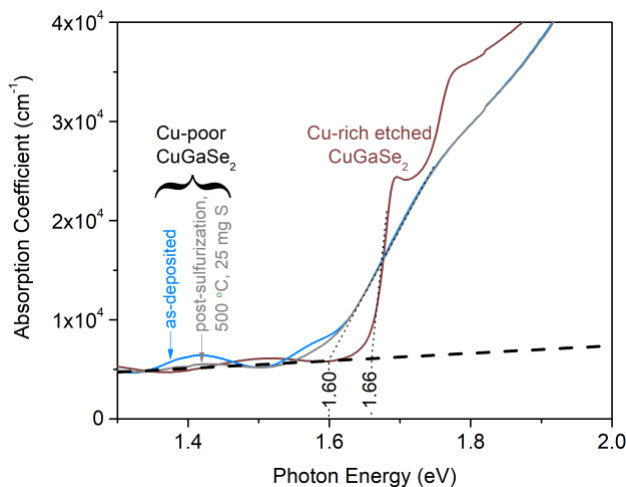


Figure 16. Plot of absorption coefficient showing that the one-step sulfurization does not increase the band gap of Cu-poor CuGaSe_2 . As-deposited CuGaSe_2 is plotted to show the slight differences in band gap between Cu-rich and Cu-poor CuGaSe_2 as measured by UV-vis.

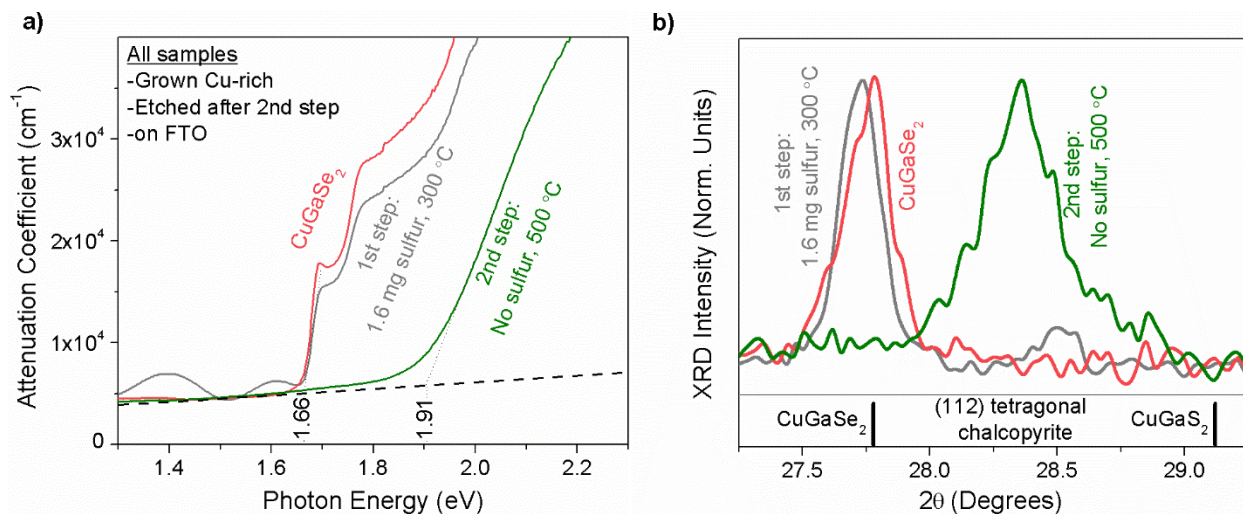


Figure 17. Plot of (a) absorption coefficient and (b) BBXRD before and after the first low-temperature sulfurization step as well as after the second inert annealing step, showing that the E_G and XRD (112) chalcopyrite peak position does not increase until the second step is performed.

Since the XRD (112) chalcopyrite peak did not shift toward CuGaS_2 after the low-temperature sulfurization, but did after the high-temperature inert annealing, an interesting question regarding the sulfurization process emerged: is sulfur being “stored” within the sample during the low-temperature sulfurization and if so how? To the best of our knowledge there are no studies

reporting this phenomenon, but we speculate that the sulfur is “stored” in three possible ways: 1) interstitially within the CuGaSe₂ lattice, 2) as a layer of elemental sulfur that redeposits on the surface during cooldown or 3) within the secondary copper selenide/sulfide phases. The surface color change could support the third explanation, but additional characterization is necessary to be certain.

iii. PEC Performance of Functional E_G-tunable CuGa(S,Se)₂ Photocathodes

Using the two-step annealing we fabricated functional CuGa(S,Se)₂/FTO photoelectrodes and compared their PEC performances to that of Cu-rich CuGaSe₂ photocathodes. First, a Cu-rich CuGaSe₂ precursor was cracked in half. One half received a two-step annealing (1st step = 1.0 mg S, 300 °C, 60 mins; 2nd step = 500 °C, 10 mins). The other half was not annealed. The two halves were then KCN-etched and wired up as photoelectrodes. Chopped-illuminated LSV preconditioning scans were performed until any unstable features, usually present in the first several LSV scans of a photoelectrode, were removed, prior to performing the scans shown in Figure 18. Figure 18.a shows that the KCN-etched Cu-rich CuGa(S,Se)₂ photocathode (E_G=1.72 eV) yielded a J_{SAT} of approximately 10 mA/cm² whereas that of the KCN-etched Cu-rich CuGaSe₂ (E_G=1.66 eV) photocathode was approximately 9 mA/cm². The photocurrent onset potential (V_{ONSET}, defined as the potential at which the line extrapolated from the exponential rise portion of the photocurrent intersects the potential axis) of the KCN-etched Cu-rich CuGa(S,Se)₂ photocathode (-0.20 V_{RHE}) was anodically shifted 125 mV relative to that of the KCN-etched Cu-rich CuGaSe₂ photocathode (-0.32 V_{RHE}). Figure 18.b compares the difference in PEC performance between Cu-rich and Cu-poor CuGaSe₂. The un-etched, as-deposited Cu-rich CuGaSe₂ photocathode (black line) output negligible photocurrent. A subsequent KCN-etch on this photocathode allowed it to output a photocurrent comparable to that measured on the etched Cu-rich CuGaSe₂ (identical curve measured on KCN-etched Cu-rich CuGaSe₂ in Figure 18.a). Overall, the Cu-poor CuGaSe₂ photocathode performed best, exhibiting a E_{ONSET} (-0.03 V_{RHE}) that was anodically shifted approximately 300 mV relative to the KCN-etched Cu-rich CuGaSe₂ photocathode, and a J_{SAT} (18 mA/cm²) double that of the Cu-rich (9 mA/cm²).

An interesting feature about the LSV data presented above is the variation of E_{ONSET} between samples. Other groups have also observed similar effects of copper not only on the V_{ONSET}, but also on the J_{SAT} of copper gallium selenide (spelt out to include other ternary compounds such as CuGa₃Se₅ and CuGa₅Se₈) photocathodes. Kessler *et al.* measured an anodic shift of 200 mV in the E_{ONSET} of Cu-poor when compared to Cu-rich CuGaSe₂ photocathodes (both samples had J_{SAT} of approximately 1 mA/cm²).³² Kim *et al.* observed an anodic shift of approximately 500 mV and an increase from 2 to 5 mA/cm² when the Cu/Ga ratio of their copper gallium selenide photocathodes decreases from 0.6 to 0.3.³³ Coincidentally, they also found that the valence band maximum (E_V) decreases in energy (deepens) as the Cu/Ga ratio decreases. Thus they conclude that the observed anodic shift in E_{ONSET} is due to the E_V deepening.

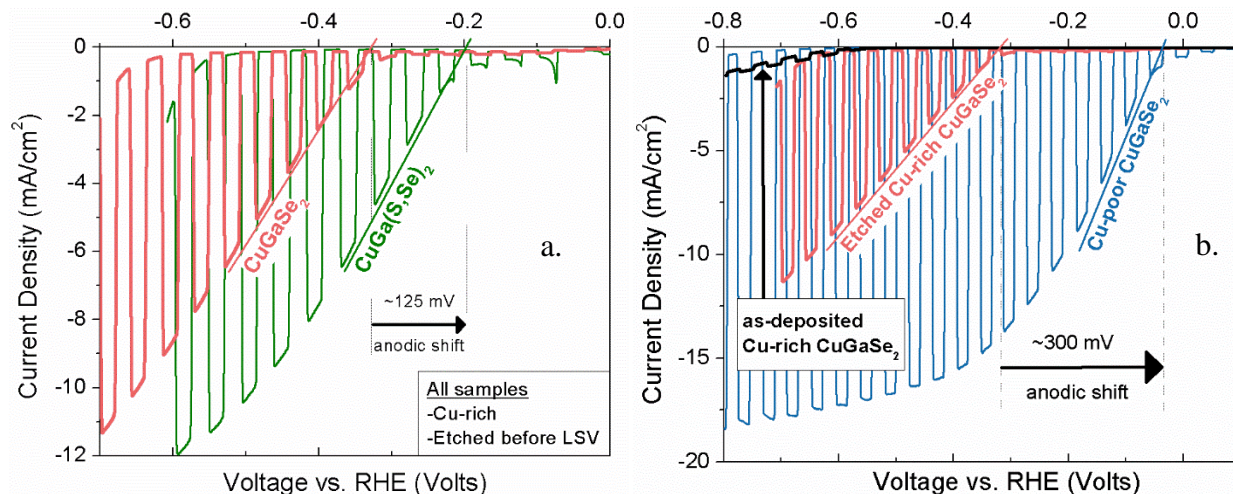


Figure 18. (a) Chopped-Illuminated LSV scans of KCN-etched Cu-rich CuGa(S,Se)₂ and CuGaSe₂ photocathodes. CuGa(S,Se)₂ outperformed CuGaSe₂, exhibiting a J_{SAT} approximately 1 mA/cm² higher and a E_{ONSET} 125 mV more anodic. (b) Chopped-Illuminated LSV scans of Cu-rich (un-etched = black, etched = red) and Cu-poor CuGaSe₂ (blue) photocathodes. Without etching, Cu-rich photocathodes output negligible photocurrent. Cu-poor CuGaSe₂ outperformed KCN-etched Cu-rich CuGaSe₂, exhibiting a J_{SAT} approximately doubled and a E_{ONSET} 300 mV more anodic.

To determine if a deepening of Ev could explain the varying E_{ONSET} of the samples in Figure 18, we measured the flat-band potential (E_{FB}) via the illuminated open circuit potential (OCP) technique [20]. As seen in Figure 19, the photocathodes were first allowed to reach a stable dark OCP value prior to illumination. The electrodes were then illuminated with 1-sun until a stable value was reached. This procedure was repeated all the way up to 5 suns (the limit of our experimental setup) in 1-sun increments. For the Cu-poor CuGaSe₂, illumination caused the OCP to shift positively. On the other hand, the etched Cu-rich CuGaSe₂ and CuGa(S,Se)₂ photocathodes both experienced a negative shift in OCP upon illumination, which was unexpected as it is commonly assumed that p-type semiconductors shift positively upon illumination.³⁴ Although we did not measure the conductivity type of these samples, all of our samples exhibit large photocathodic current implying p-type conductivity. Furthermore, CuGaSe₂ (Cu-poor or Cu-rich) free of external dopants has always been reported p-type in the literature.³⁵ We do not offer an explanation for this phenomenon here, but simply point out an exception to the positive-shift/p-type rule. We also point out that the E_{FB} values of 0.53 V_{RHE} (Cu-poor CuGaSe₂), 0.38 V_{RHE} (Cu-rich CuGaSe₂), and 0.41 V_{RHE} are close approximations to a true value since we were still able to observe small changes in OCP of 2-3 mV in going from 4 to 5 suns.

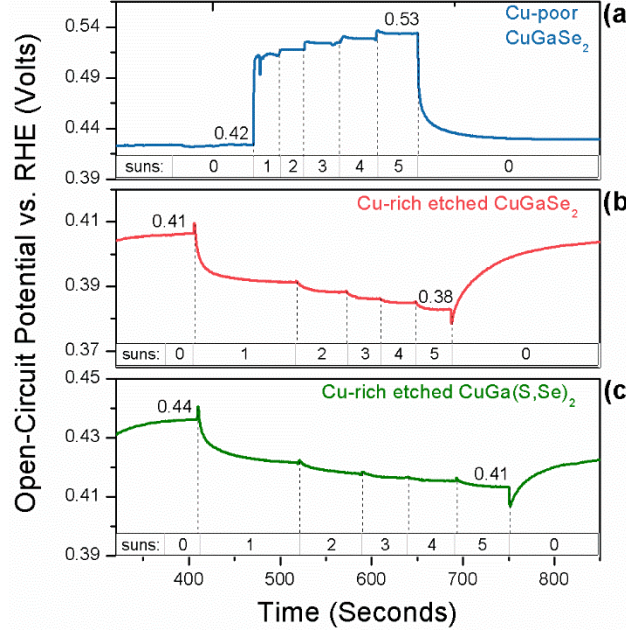


Figure 19. Illuminated OCP measurements on the same samples of the previously shown LSV scans of Figure 18. The etched Cu-rich CuGaSe₂ and CuGa(S,Se)₂ photocathodes exhibited a negative shift of the OCP under illumination, implying upward band bending at equilibrium, whereas Cu-poor CuGaSe₂ exhibited a positive OCP shift under illumination, implying downward band bending at equilibrium.

Using the E_{FB} values from Figure 19 and the Gerischer model of electron transfer,³⁶ in Figure 20 we have drawn a series of energy band diagrams to explain the variation in E_{ONSET} of our samples. Several initial assumptions have been made in order to draw the diagrams. For CuGaSe₂, the Fermi level to valence band maximum difference ($E_F - E_v$) and E_G were 0.20 and 1.66 eV, respectively.^{27,35} For CuGa(S,Se)₂ ($E_G = 1.72$ eV), the 0.06 eV increase in E_G is included exclusively as a deepening of E_v , since it has been observed that sulfur deepens only the E_v in similar copper gallium selenide compounds (e.g. CuGa₃(S,Se)₅).³⁷

Our rationale for interpreting the Gerischer model is as follows. According to the model of electron transfer:

$$J_{CB \rightarrow H^+} \propto \int_{E_C}^{\infty} f(E, E_F) \cdot g_{CB}(E) \cdot D_{H^+}(E) dE \quad (1)$$

where $J_{CB \rightarrow H^+}$ is the cathodic current density due to electrons transferring from the conduction band into the electrolyte, E is the energy level in question, $g_{CB}(E)$ is the density of states in the semiconductor conduction band, $f(E)$ is the Fermi-Dirac function, E_F is the Fermi level, and $D_{H^+}(E)$ is the distribution of H^+ states in the electrolyte. Equation (1) essentially implies that: 1) more overlap of the conduction band and H^+ energy states ($g_{CB} \cdot D_{H^+}$) should yield higher current and 2) E_F modulates this product such that the smaller the conduction band minimum to Fermi level energy difference ($E_C - E_F$) is, the higher the current will be. Since these terms are all functions of electron energy, which in turn is dependent on applied bias, we can say that the LSV with the most anodic E_{ONSET} will be the electrode that has the greatest $g_{CB} \cdot D_{H^+}$ and/or smallest $E_C - E_F$ (i.e. greatest $f \cdot g_{CB} \cdot D_{H^+}$).

With those remarks, we can now explain the energy band diagrams below in Figure 20. Before bringing the semiconductor and the electrolyte in contact (flat-band, Figure 20.a) already we see that Cu-poor CuGaSe₂ will lead to the greatest $g_{CB} \cdot D_{H^+}$ overlap, followed by CuGa(S,Se)₂ and then Cu-rich CuGaSe₂, which coincides with the trend we saw for E_{ONSET} in Figure 18. After contact (equilibrium with E_{H_2/H^+} , Figure 20.b) the Cu-poor bands bend down while the Cu-rich bands bend up, causing Cu-poor CuGaSe₂ to not only have an even greater $g_{CB} \cdot D_{H^+}$ overlap, but also a smaller (Ec -EF), which is why we have drawn the Cu-poor CuGaSe₂ $J_{CB \rightarrow H^+}$ cathodic current hump larger than the Cu-rich samples, shown in Figure 20.b. Also included in the bottom right of Figure 20.b are the $J_{VB \leftarrow H_2}$ anodic current humps, due to electrons transferring from the electrolyte H₂ states into the valence band, equal in area to their respective $J_{CB \rightarrow H^+}$ cathodic current humps in order to accurately represent the exchange current between semiconductor and electrolyte. Figure 20.c shows what happens to the bands when applying a cathodic potential in dark, but since we have assumed that the potential pushes all bands up equally (0.4 eV in this example) applying a bias does not grant favorable energetics to any one material relative to the others. However, we can see that the $J_{CB \rightarrow H^+}$ humps have slightly grown since (Ec -EF) has become smaller. Finally, Figure 20.d shows the effect of 1-sun illumination. It has been observed that Cu-poor Cu(In,Ga)Se₂ has stronger quasi Fermi level splitting (qFLs) than Cu-rich Cu(In,Ga)Se₂ ($1.09 < E_G < 1.16$ eV).³⁸ Assuming this stronger qFLs also holds true for CuGaSe₂, we have drawn Cu-poor CuGaSe₂ with a higher quasi Fermi level for electrons (E_F^n) than Cu-rich CuGaSe₂. The higher E_F^n of Cu-poor CuGaSe₂ would make the (Ec -EF) even smaller, leading to a greater $f \cdot g_{CB} \cdot D_{H^+}$ product in comparison to the Cu-rich samples, which is why the Cu-poor cathodic current hump on the right of Figure 20.d was drawn largest.

In regard to Cu-poor vs. Cu-rich CuGaSe₂ and the work of Kim *et al.*,³³ we believe it is not so much that the Ev is deepened, but that Ec (yielding a greater $g_{CB} \cdot D_{H^+}$) and EF (yielding a smaller Ec-EF at surface due to greater band bending) are simultaneously deepened with it, both of which yield a greater $f \cdot g_{CB} \cdot D_{H^+}$ product and thus a higher $J_{CB \rightarrow H^+}$ at more anodic potentials. In regard to CuGa(S,Se)₂ though, it is not entirely clear how its E_{ONSET} is 125 mV more anodic than Cu-rich CuGaSe₂. Figure 20.a shows that, under our assumptions, the Ec of CuGa(S,Se)₂ is only 30 meV lower than Cu-rich CuGaSe₂ and that the Ec-EF of both Cu-rich samples coincidentally turned out to be exactly the same at equilibrium (1.49 eV). How do we account for the other 95 meV? A possible answer is that the qFLs is approximately 100 meV greater than Cu-rich CuGaSe₂, which is why the qFLs for CuGa(S,Se)₂ is drawn to be 0.40 instead of 0.30 eV in Figure 20.d.

To assess the viability of the CuGa(S,Se)₂ photoelectrodes as a top cell, we first performed external quantum efficiency (QE) measurements on a 1.1eV Cu(In,Ga)Se₂-based solar cell (PCE \approx 17%), provided by the National Renewable Energy Laboratory), shown in Figure 21, before and after being shaded by the CuGa(S,Se)₂ photocathode of Figure 18 ($E_G = 1.72$ eV). The short-circuit current density of the shaded Cu(In,Ga)Se₂ device was calculated to be 4.14 mA/cm² by integrating the product of the QE and AM1.5 spectrum over all photon energies. Comparing the J_{SAT} of the CuGa(S,Se)₂ photocathode (10.0 mA/cm²) and the shaded J_{SC} of the Cu(In,Ga)Se₂ device calculated from QE measurements (4.14 mA/cm²), we can see that a hypothetical tandem device in which they are paired together would be limited by the photocurrent of the shaded bottom cell. A theoretical upper limit STH efficiency for this hypothetical device can be calculated by using a variation of an equation for STH efficiency given by Chen *et al.*:¹¹

$$\text{Theoretical STH [\%]} = \frac{\min \left[J_{\text{top}}, J_{\text{bot}} \left[\frac{\text{mA}}{\text{cm}^2} \right] \right] \times 1.23[\text{V}] \times \eta_f}{P_{\text{total,AM1.5}} \left[\frac{\text{mW}}{\text{cm}^2} \right]} \times 100 \quad (2)$$

where J_{top} and J_{bot} are the photocurrent densities of the top and bottom cell, respectively, η_f is the faradaic efficiency for hydrogen evolution, $P_{\text{total,AM1.5}}$ is the power density of the AM1.5 spectrum integrated over all wavelengths (100 mW/cm²), and the factor of 100 is multiplied to turn the ratio into a percentage. Using $J_{\text{top}}=10$ mA/cm² and $J_{\text{bot}}=4.14$ mA/cm² in equation 2, and assuming a faradaic efficiency of 1, yields a theoretical STH efficiency upper limit of 5.1% for this hypothetical tandem device.

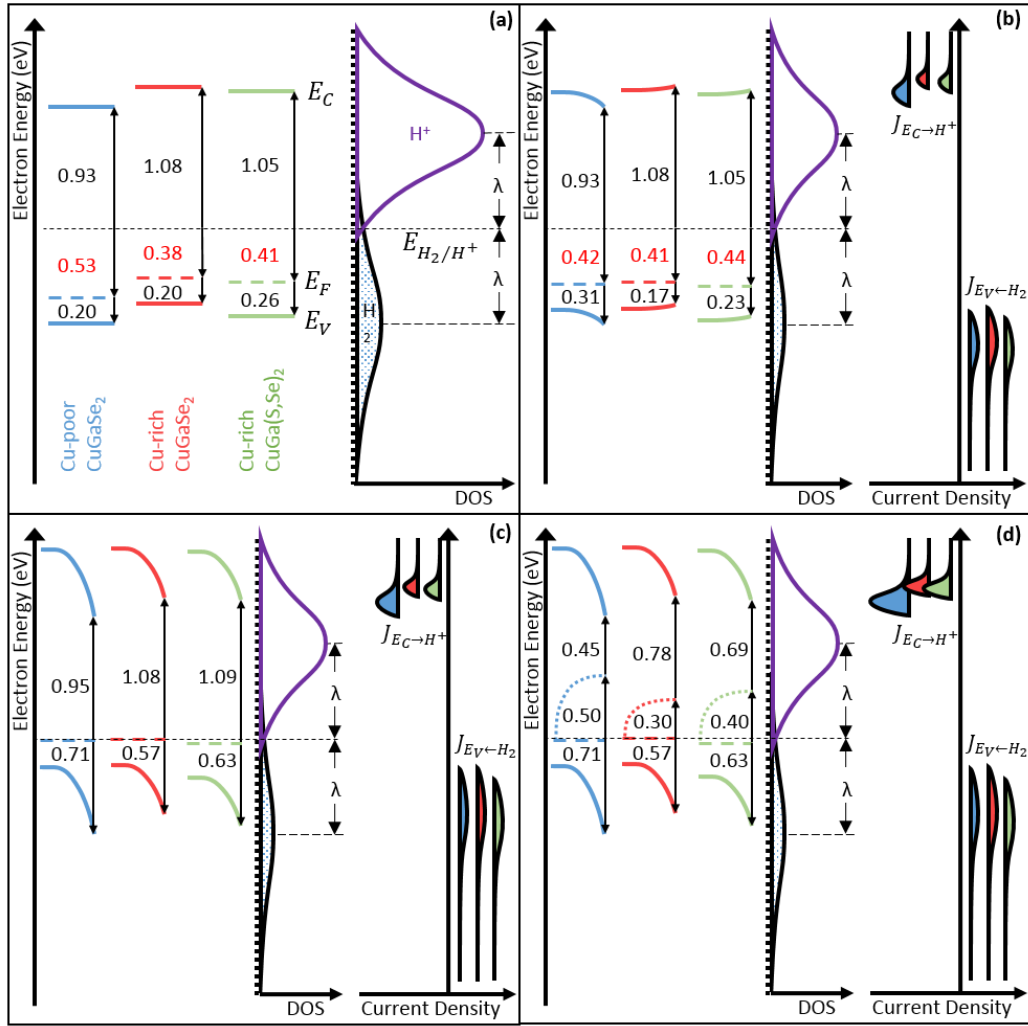


Figure 20. (a) Energy band diagrams of the samples from Figure 19 (blue = Cu-poor CuGaSe₂, red = Cu-rich CuGaSe₂, green = Cu-rich CuGa(S,Se)₂) before contact with the electrolyte with the (red numbers = flat-band potentials), (b) after contact (red numbers = dark OCP values), (c) under cathodic potential (-0.4 V), and (d) with 1-sun illumination added. Reorganization energy, λ , was chosen to be 0.73 eV. Since Cu-poor CuGaSe₂ has the lowest E_C and bands that bend down, instead of up, it ends up having the greatest $f \cdot g_{CB} \cdot D_{H^+}$ product, at any given potential, and thus the most anodic V_{ONSET} .

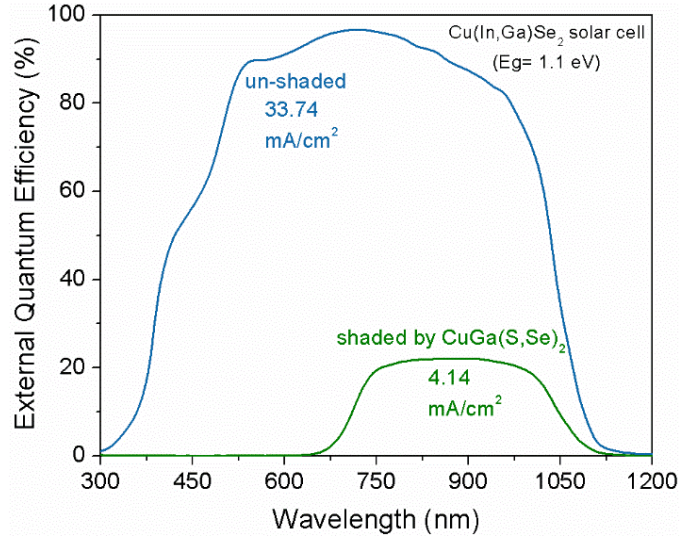


Figure 21. External quantum efficiency measurements of Cu(In,Ga)Se₂ solar cell showing that its photocurrent output was drastically reduced when shaded by the CuGa(S,Se)₂ photocathode of Figure 18.

To better understand why the shaded QE of the Cu(In,Ga)Se₂ device was low, UV-vis transmittance measurements of Cu-poor CuGaSe₂, KCN-etched Cu-rich CuGaSe₂ and CuGa(S,Se)₂ were compared, as seen in Figure 22. Comparing the Cu-poor vs Cu-rich CuGaSe₂, we can see that just by growing it Cu-rich reduced the sub-E_G transmittance by 30 points, from an approximate average of 80% to 50%. Meeder *et al.* appear to be the first to have provided insight into this copper-dependent reduction in transmittance by associating the sub-E_G absorption to a defect level that becomes present only when CuGaSe₂ is Cu-rich.³⁹ The authors calculated the defect level, associated with a broad photoluminescence (PL) peak measured at 1.25 eV, to be an acceptor level 250 meV above E_v. Spindler *et al.* expanded on this work, concluding that the broad PL peak observed by Meeder *et al.* is instead due to an electron trap situated at least 390 meV below E_c, which they refer to as DD2.⁴⁰ The works of Krystopza *et al.* support Spindler's conclusion in which they report that an electron trap level exists between 100-400 meV below E_c, as measured by photoinduced current transient spectroscopy.⁴¹ Additionally, Spindler *et al.* also calculated that DD2 is not saturated during their PL measurements. From this calculation, they speculate that the under-saturated DD2 causes the reduced qFLs in Cu-rich vs Cu-poor Cu(In,Ga)Se₂ observed by Babbe *et al.* [27]. All this evidence suggests a copper induced defect band located 100-400 meV below E_c that causes a reduction in both the sub-E_G transmittance, via a mechanism that is yet unclear, and PEC performance, via a reduction in qFLs. If this conclusion is true for Cu-rich CuGaSe₂, then a likely cause for the low sub-E_G transmittance, and thus the low shaded QE of Cu(In,Ga)Se₂, in Cu-rich CuGa(S,Se)₂ is due to it being Cu-rich. Now focusing on the change in sub-E_G transmittance before and after the two-step annealing, we see that it was reduced by another 20 points, from 50% to 30%. We do not yet have an explanation as to why this reduction occurs during the two-step annealing, but speculate that it could be caused by either a change in crystal structure or defect chemistry both of which can affect the optical properties of a material.

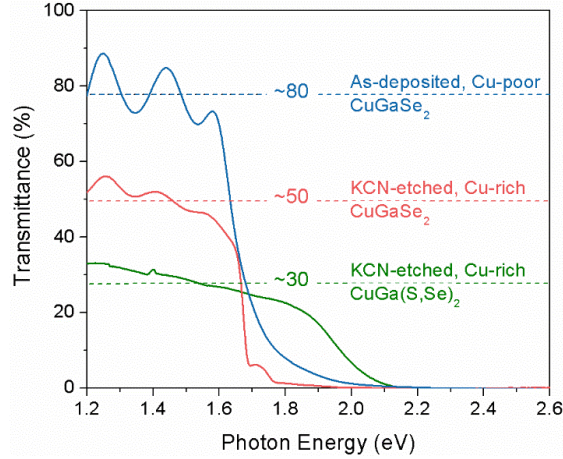


Figure 22. Sub-EG transmittance of Cu-poor CuGaSe_2 (top), Cu-rich CuGaSe_2 (etched, middle), and Cu-rich $\text{CuGa}(\text{S},\text{Se})_2$ (etched, bottom) showing that growing CuGaSe_2 Cu-rich reduces the sub-EG transmittance significantly and is further reduced after the two-step annealing.

iv. Conclusions

The goal of this study was to synthesize band gap-tunable $\text{CuGa}(\text{S},\text{Se})_2$ on transparent conductive FTO and explore its performance as a wide-EG top cell for PEC water splitting applications. First, we demonstrated that our one-step sulfoselenization annealing was successful at converting CuGaSe_2 into $\text{CuGa}(\text{S},\text{Se})_2$. Copper content had a profound effect on the sulfurization, as only Cu-rich CuGaSe_2 precursors could be converted into $\text{CuGa}(\text{S},\text{Se})_2$. Unfortunately, this one-step sulfoselenization would also lead to highly resistive FTO back contacts. A two-step annealing was then developed to prevent the FTO from becoming resistive, in which the first step was a low-temperature ($300\text{ }^\circ\text{C}$) sulfurization and the second step was a high-temperature ($500\text{ }^\circ\text{C}$) annealing in an inert atmosphere. Using this two-step annealing, an etched Cu-rich $\text{CuGa}(\text{S},\text{Se})_2$ (1.72 eV) photocathode with $J_{\text{SAT}}=10\text{ mA/cm}^2$ and $V_{\text{ONSET}}=-0.20\text{ V vs RHE}$ was obtained. A high-performance $\text{Cu}(\text{In},\text{Ga})\text{Se}_2$ bottom solar cell shaded by this $\text{CuGa}(\text{S},\text{Se})_2$ photocathode output a QE-calculated J_{SC} of 4.14 mA/cm^2 , showing that the sub-EG transmittance of the $\text{CuGa}(\text{S},\text{Se})_2$ was the limiting factor of such a hypothetical tandem device.

We also investigated the impact of copper content in chalcopyrite photocathodes using CuGaSe_2 as a case study. When compared to etched Cu-rich CuGaSe_2 , Cu-poor CuGaSe_2 output a J_{SAT} twice as high ($9\text{ vs }18\text{ mA/cm}^2$), had a E_{ONSET} that was 300 mV more anodic, and a sub-EG transmittance that was 30 points higher. According to our Gerischer analysis using measured E_{FB} values, it appears that Cu-rich CuGaSe_2 has an inherently lower E_{C} as well as interface bands that bend upward (towards vacuum) whereas Cu-poor CuGaSe_2 exhibited a downward band bending, with a 135 meV difference between the two, which partly explains the 300 mV anodic shift that Cu-poor CuGaSe_2 experienced. We also presented a complementary explanation of the difference in performance between Cu-poor and Cu-rich CuGaSe_2 that suggests the reduced PEC performance (J_{SAT} , V_{ONSET}) and sub-EG transmittance in Cu-rich CuGaSe_2 are both caused by the presence of a copper-induced defect level, as identified by other groups, situated $100\text{-}400\text{ meV}$ below E_{C} . From this comparison of Cu-poor and Cu-rich CuGaSe_2 photocathodes, we predict that Cu-poor $\text{CuGa}(\text{S},\text{Se})_2$ would perform better than the Cu-rich $\text{CuGa}(\text{S},\text{Se})_2$, although a successful synthesis route for Cu-poor $\text{CuGa}(\text{S},\text{Se})_2$ is yet to be developed.

d. Wide band gap Cu(In,Ga)S₂ absorbers from Cu(In,Ga)Se₂ precursors

i. Overview

Cu(In,Ga)S₂ is a preeminent wide-E_G top cell candidate for chalcopyrite-based HPE devices. Numerous groups have already demonstrated from modeling or experiments that E_G in the 1.54 eV (CuInS₂) to 2.46 eV (CuGaS₂) range can be attained with Cu(In,Ga)S₂ absorbers, implying that the optimum E_G range (1.8-2.0 eV) PEC water splitting can be achieved with a specific [Ga]/([Ga]+[In]) (GGI) ratio. In the context of solar energy conversion however, the vast majority of work reported on sulfide-based chalcopyrites are focused primarily on CuInS₂ for PV applications,¹⁷ as this phase exhibits E_G close to optimum for maximum theoretical power conversion efficiency (PCE) with a single junction solar cell (Shockley-Queisser limit). In terms of synthesis, two primary methods have been explored to form CuInS₂ thin film solar absorbers: either direct co-evaporation⁴² or sulfurization of copper-rich Cu-In stacks in sulfur-vapor⁴³ (a process latter referred to as “close-space sulfurization”; CSS). Finally, molybdenum has been the prime substrate for most studies on CuInS₂-based PV devices, a choice largely driven by the success achieved with Cu(In,Ga)Se₂ solar cells on this electrical back-contact. Integrating Cu(In,Ga)S₂ on a transparent conductive F:SnO₂ (FTO) substrate, however, is a much more challenging task, as this material tends to react readily with sulfur to form resistive SnS_x. This implies that direct co-evaporation of Cu(In,Ga)S₂ on FTO should be avoided, as SnS_x would inevitably form at the absorber/back contact interface during the initial stage of deposition. In this project, we focused our efforts on integrating photoactive Cu(In,Ga)S₂ thin films on transparent conductive F:SnO₂ (FTO), while preserving the optoelectronic properties of the substrate and preventing the formation of a resistive SnS_x interfacial layer.

ii. Synthesis techniques

The band gap tunable Cu(In,Ga)S₂ thin film materials used in this study were obtained using a two-step approach, involving co-evaporation of Cu(In,Ga)Se₂ precursors on fluorine-doped SnO₂-coated soda lime glass substrates followed by closed-space sulfurization (CSS). The Cu(In,Ga)Se₂ precursors were first synthesized using a two-stage process comprising a Cu-poor step (stage #1) and a Cu-free growth phase (stage #2). The deposition temperatures, as measured by a thermocouple contacting the backside of the FTO substrates, were 150°C for stage #1 and 350°C for stage #2. For each of the two stages, the deposition times and evaporation rates were adjusted to achieve specific [Ga]/([Ga]+[In]) (GGI) ratios. A total of three deposition runs were performed for this study with targeted GGI ratios of 0.7 (later referred as ‘0.7-series’), 0.8 (‘0.8-series’) and 1 (‘1-series’). Precursors sulfurization took place in an in-house-built tube furnace in which a cylindrical weighing bottle containing elemental sulfur and a Cu(In,Ga)Se₂ precursor is placed. Both the precursor and sulfur were introduced in the weighing bottle under nitrogen atmosphere in an in-house-built glove-box with O₂ concentration less than or equal to 0.1%, corresponding to the lower detection limit of the oxygen sensor. The temperature and duration of the CSS process were empirically adjusted to achieve maximum conversion of the precursor, while at the same time limiting sulfur reaction with the FTO substrate. In fact, our preliminary studies revealed that “over sulfurization” of Cu(In,Ga)Se₂ precursors can lead to highly resistive SnO₂:F back contacts (from the formation of a SnS_x interfacial layer), and in some extreme cases, the delamination of the absorber and electrical back contact altogether from the soda lime glass substrate. Best results were achieved by sequencing the CSS process into two individual steps: a low-temperature annealing

in sulfur vapor (350°C, 60 minutes) with approx. 150 mg of sulfur (pressure = sulfur vapor pressure at 350°C ~ 0.130 atm.), followed by a high-temperature crystallization (500°C, 10 minutes) in nitrogen in absence of sulfur. In the present report, the term “sulfurized” will be used to describe samples exposed to the entire CSS process (low-temp. annealing in sulfur vapor *and* high-temp. crystallization).

iii. Microstructural, chemical and optical properties of Cu(In,Ga)S₂ absorber

The top view SEM micrograph in Figure 23.a of an as-deposited ‘0.7-series’ precursor (800 nm thick) reveals that this modified process leads to Cu(In,Ga)Se₂ films made of small, smooth grains (~100 nm across) that agglomerate into larger clusters. This morphology differs significantly with that of Cu(In,Ga)Se₂ absorbers fabricated with traditional high-temperature 3-stage process, in which the Cu_{2-x}Se-assisted phase induces the growth of large and jagged columnar grains (~1 μm across). The top view SEM micrograph in Figure 23.b demonstrates that the grains remain small, but become sharp and plate-like as a result of sulfurization. The cross-section analysis in Figure 23.a also reveals that the sulfurized precursor contains voids, as evidenced by the white regions in the bright field TEM image. The elemental composition of as-deposited and sulfurized precursors from the ‘0.7-series’, ‘0.8-series’ and ‘1-series’ were measured by top-down EDX to verify that sulfur was indeed incorporated during the CSS process. These results are presented in Table 2, along with [S]/([S]+[Se]) (SSSe) and GGI ratios, two parameters known to control E_G in Cu(In,Ga)(S,Se)₂. It can be seen that GGI ratios remain relatively unchanged after the CSS process, while up to 95% of selenium has been replaced with sulfur. Subsequent TEM-EDX analyses performed on a sulfurized precursor from ‘0.7-series’ reveals constant GGI and SSSe ratios throughout the Cu(In,Ga)S₂ bulk, averaging respectively 0.72 and 0.92 (Figure 24.b), in excellent agreement with top-down EDX data (GGI= 0.69, SSSe= 0.93). This analysis indicates that the resulting CuInGaS₂ is not band gap-graded.

Microstructural analyses performed on precursors before and after sulfurization confirm that selenium is substituted with sulfur in the chalcopyrite crystallographic lattice. The XRD scans in Figure 23.c and performed on a precursor from ‘0.7-series’ show that the prominent (112), (220), and (312) reflection peaks were shifted to higher angles after sulfurization, a direction consistent with the substitution of selenium with an element with smaller radius in the chalcopyrite lattice, in this case sulfur. This elemental substitution is also confirmed by Raman spectroscopic analyses performed on a precursor from ‘0.7-series’ and presented in Figure 23.c. One can see that the fundamental A₁ mode measured at 185 cm⁻¹, characteristic of selenium vibration against the cation lattice in Ga-rich chalcopyrites,⁴⁴ was shifted after the CSS process to 308 cm⁻¹, a value corresponding to the A₁ mode characteristic of sulfur vibration against the cation lattice in Ga-rich chalcopyrites.⁴⁵ Additional peaks observed for the sulfurized precursor were assigned to three vibration modes known for Ga-rich, S-based chalcopyrites; B_{2(TO)}² (276 cm⁻¹), E_{5(TO)} (342 cm⁻¹) and B_{2(LO)}³ (380 cm⁻¹).

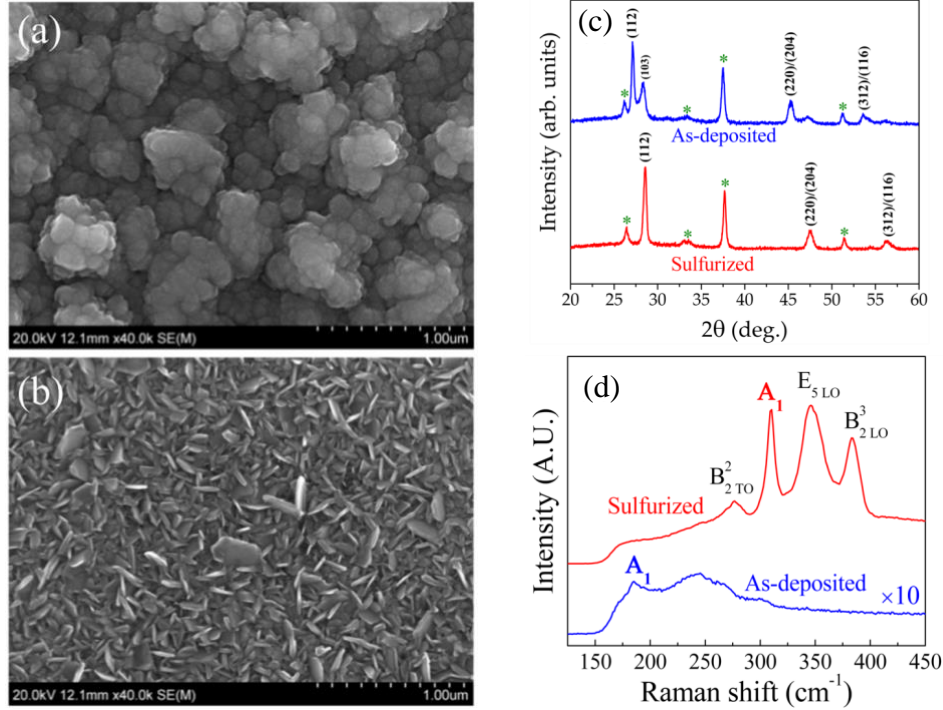


Figure 23. Top view scanning electron micrographs of (a) as-deposited and (b) sulfurized ‘0.7-series’ Cu(In,Ga)Se₂ thin film. (c) XRD scan and (d) Raman shift measured on as-deposited and sulfurized precursor from the ‘0.7-series’. Diffraction peaks measured on the FTO substrate are identified by asterisks.

Table 2. Elemental composition (relative error: +/- 2%), GGI, SSSe and E_G (+/- 0.05 eV) calculated from UV-visible spectroscopy measurements of Cu(In,Ga)Se₂ precursors from ‘0.7-series’, ‘0.8-series’ and ‘1-series’ before and after sulfurization.

| | GGI=0.7-series | | GGI=0.8-series | | GGI=1-series | |
|------------------|----------------|----------------|----------------|----------------|--------------|----------------|
| | As-deposited | Sulfurized | As-deposited | Sulfurized | As-deposited | Sulfurized |
| [Cu] | 12.4% | 13.2% | 10.1% | 11.4% | 13.6% | 14.3% |
| [In] | 9.7% | 8.8% | 6.5% | 4.4% | 0.0% | 0.0% |
| [Ga] | 21.5% | 19.7% | 23.4% | 21.1% | 29.2% | 27.1% |
| [Se] | 56.4% | 3.9% | 60.0% | 3.2% | 57.2% | 3.0% |
| [S] | 0.0% | 54.5% | 0.0% | 59.9% | 0.0% | 55.6% |
| [Ga]/([Ga]+[In]) | 0.69 | 0.69 | 0.78 | 0.83 | 1.00 | 1.00 |
| [S]/([S]+[Se]) | 0.00 | 0.93 | 0.00 | 0.95 | 0.00 | 0.95 |
| Bandgap | 1.42 eV | 2.05 eV | 1.51 eV | 2.20 eV | 1.67 eV | 2.45 eV |

It is worth noting that the fundamental A₁ mode measured on Cu(In,Ga)Se₂ precursor is much broader and weaker in intensity than that of Cu(In,Ga)S₂ (Figure 23.d) or any chalcopyrite absorbers synthesized by our group so far. Although Raman spectroscopy is often used for phase identification, studies have shown direct correlations between broadening of Raman peaks and absorber crystal quality (grain size and defects density) for chalcopyrites,⁴⁶ concluding that the more defective the material, the broader the fundamental A₁ mode. Thus, we conclude that the broad Raman response observed on the as-deposited Cu(In,Ga)Se₂ precursor is an indicator of

“poor” crystallographic ordering, induced by the low-temperature used during the co-evaporation process and the absence of a Cu_{2-x}Se -assisted growth phase. Reflecting on the Nakada *et al.* report correlating chalcopyrite synthesis temperature with sulfur diffusion depth,⁴⁷ we conclude that the “poor” crystallographic ordering of the Cu-poor $\text{Cu}(\text{In,Ga})\text{Se}_2$ precursors used in the present study is the key attribute facilitating sulfur incorporation and selenium substitution.

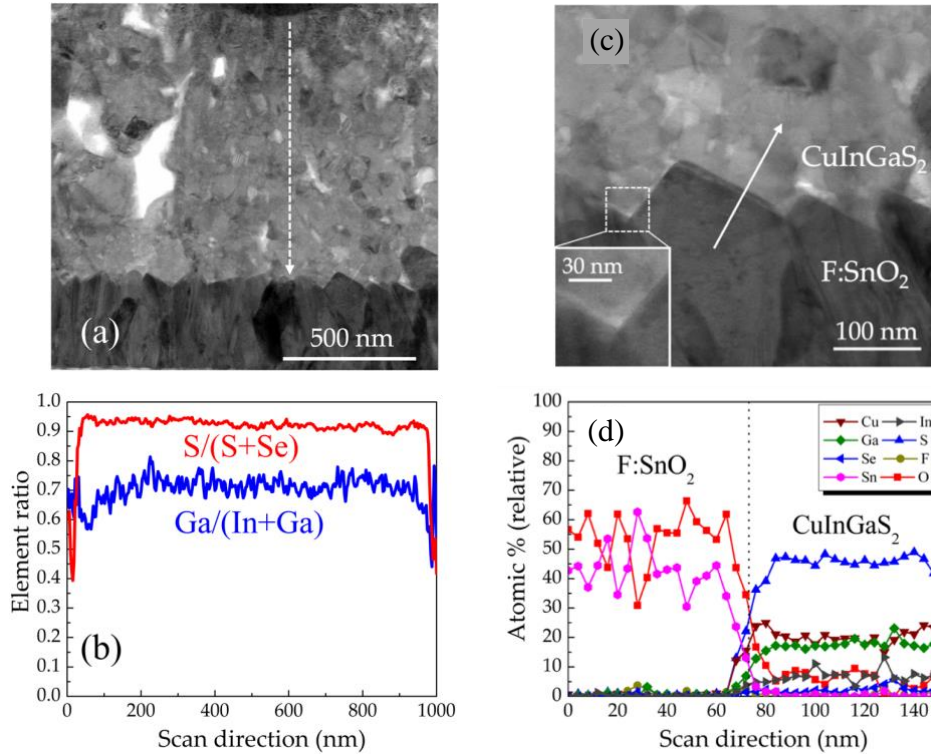


Figure 24. (a) Bright field TEM micrograph and (b) Ga/(Ga+In) and S/(S+Se) ratios measured in sulfurized precursor from the ‘0.7-series’ taken along the vector indicated by the white arrow in (a). (c) Bright field TEM micrograph and (d) Cu, In, Ga, S, Se, F, Sn and O elemental distribution at the $\text{CuInGaS}_2/\text{FTO}$ interface taken along the vector indicated by the white arrow in (c). All Data were collected at 300 keV using a ~ 0.2 nm diameter electron probe.

Sequencing the CSS process into a low-temperature sulfurization followed by a high-temperature crystallization is key to minimizing the formation of Sn_xS at the $\text{CuInGaS}_2/\text{FTO}$ interface. This claim is supported by the bright field TEM micrograph (Figure 24.c) and TEM-EDX survey scan profiles (Figure 24.d) of this interface, where a sharp transition can be observed between the FTO substrate and the CuInGaS_2 absorber, with minimal species inter-diffusion. Notably, the Sn and S profile transitions at the interface occur within less than 20 nm (equivalent to 4 data points in the line profile), confirming that the CSS process is effective in preventing FTO from reacting with sulfur.

As a result of the CSS process, we observed a systematic increase in E_g , as seen from the Tauc plots in Figure 25.a. Prior to sulfurization, the E_g of as-deposited ‘0.7-series’, ‘0.8-series’ and ‘1-series’ precursors was 1.42 eV, 1.51 eV and 1.67 eV, respectively. After sulfurization, their E_g increased to 2.05 eV, 2.20 eV and 2.45 eV. The change in band gap can also be observed by the naked eye, as presented in Figure 25.b which shows an optical image of the red 2.05 eV, orange

2.20 eV and yellow 2.45 eV Cu(In,Ga)S₂ wide band gap absorbers, along with a brown 1.67 eV CuGaSe₂ baseline reference film (all films on FTO substrates). The change in E_g for Cu(In,Ga)Se₂ precursors of given GGI ratios is also in good agreement with our theoretical calculations (Figure 4.a), as shown in Figure 25.c, supporting that sulfur replaced selenium as a result of the CSS process.

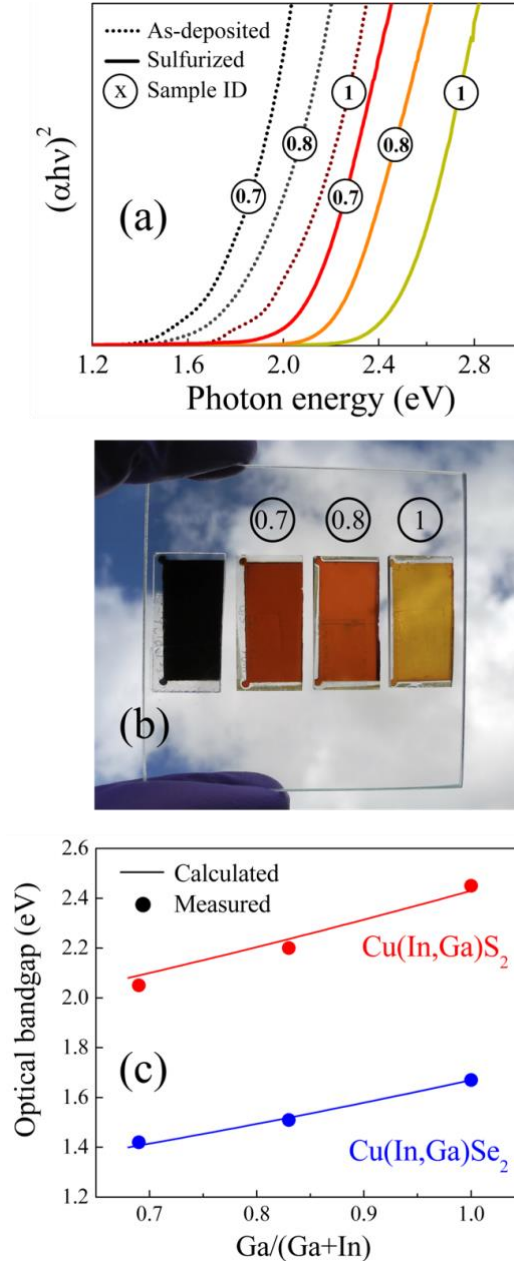


Figure 25. (a) Tauc plots measured on ‘0.7-series’, ‘0.8-series’ and ‘1-series’ Cu(In,Ga)Se₂ precursors before (dotted lines) and after (solid lines) the CSS process. (b) Left to right: Optical image of 1.67 eV CuGaSe₂, 2.05 eV ‘0.7-series’, 2.20 eV ‘0.8-series’ and 2.45 eV ‘1-series’ Cu(In,Ga)S₂ thin films. All layers are integrated on FTO substrates. (c) Measured and calculated optical band gaps for Cu(In,Ga)Se₂ and Cu(In,Ga)S₂ as function of GGI.

iv. Photoelectrochemical properties of Cu(In,Ga)S₂ absorbers

Figure 26.a presents the Mott-Schottky (MS) analysis performed at a frequency of 10 kHz on both 2.05 eV CuInGaS₂ and 1.67 eV CuGaSe₂ baseline photoelectrodes under simulated AM1.5G illumination. The negative slopes of MS plots revealed p-type conductivity for both absorbers, whereas the intercepts with the potential axis indicated E_{FB} of +275 mV_{RHE} and +500 mV_{RHE} for 1.67 eV CuGaSe₂ baseline and 2.05 eV CuInGaS₂, respectively. The E_{FB} values measured on 2.05 eV CuInGaS₂ and 1.67 eV CuGaSe₂ baseline photoelectrodes were then combined with UV-visible spectroscopy measurements to derive the approximate band-edges position of these materials (Figure 26.b). The positions of the valence band maxima (E_v) were set identical to that of the Fermi levels, as commonly done for highly p-type copper chalcopyrite absorbers. The conduction band minima (E_c) were obtained by adding the value of the optical band gaps. Our results place the E_v and E_c of 2.05 eV CuInGaS₂ 230 meV lower and 150 meV higher than that of the 1.67 eV CuGaSe₂. While this analysis combines bulk band gap and flat-band potential analysis techniques and does not measure the surface band gap directly, it suggests that roughly 2/3 of the band gap difference between the 1.67 eV CuGaSe₂ baseline and 2.05 eV CuInGaS₂ stems from a downward shift in E_v (230 meV), which is an ideal situation for improving the energetics of p-type PEC systems. Furthermore, this conclusion is supported by separate hybrid functional calculations of band alignments previously reported by our team on several chalcopyrite candidates,⁴⁸ which predict CuInS₂ and CuGaS₂ to exhibit lower E_v positions relative to CuGaSe₂. We also determined that GGI has a large influence on the relative position of E_c . Using these calculations, we estimate an E_v downward shift of 330 meV and an E_c upward shift of 90 meV for the 2.05 eV CuInGaS₂ relative to CuGaSe₂. This estimate assumes that all E_G bowing occurs in E_c of 2.05 eV CuInGaS₂. Although this uncertainty could translate to either band-edge, nevertheless our calculated ($\Delta E_v = -330$ mV, $\Delta E_c = +90$ mV) and experimentally measured ($\Delta E_v = -230$ mV, $\Delta E_c = +150$ mV) values agree with each other to within 100 meV.

The LSV measured on the 2.05 eV CuInGaS₂ photocathode, presented in Figure 26.c, reveals good photoconversion properties with negligible dark current between light (+0.35 V_{RHE}) and dark (-0.4 V_{RHE}) current onset potentials and a saturated photocurrent density (J_{SAT}) of -5.25 mA/cm² at -400 mV_{RHE}. Also, the “ $V_{onset} - V_{FB}$ ” quantity (150 mV) is significantly lower than that of CuGaSe₂ baseline photocathodes (500 mV), suggesting more favorable energetics towards the hydrogen evolution reaction (HER). It is worth mentioning that the surface energetics of 2.05 eV CuInGaS₂ are still far from optimum for un-assisted PEC water splitting. To achieve spontaneous water photocleavage, the energetics and activity towards HER of the proposed wide band gap chalcopyrite materials must be tailored respectively with n-type buffer materials (see Task 2) and catalysts (see Task 3) to reduce overpotentials and improve kinetics. Nonetheless, our preliminary PEC testing revealed that the CSS process is a viable approach to produce single phase, photoactive, wide- E_G Cu(In,Ga)S₂ materials with relatively good catalytic properties towards HER.

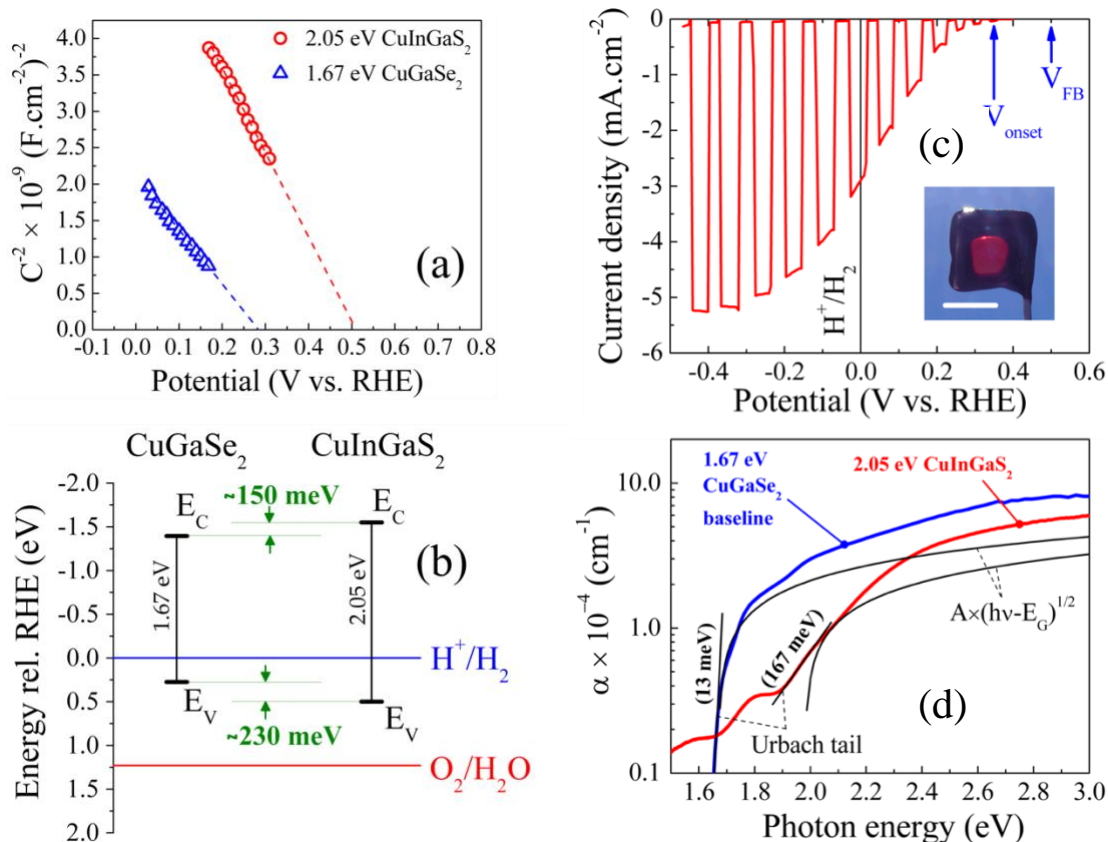


Figure 26. (a) MS plots measured on a 1.67 eV CuGaSe₂ baseline (open triangles) and a 2.05 eV CuInGaS₂ (open circles) photocathodes. (b) E_v and E_c positions of 1.67 eV CuGaSe₂ baseline and 2.05 eV CuInGaS₂ relative to RHE derived from MS and UV-visible measurements. (c) Linear sweep voltammetry measured under chopped AM1.5G illumination in 0.5M H₂SO₄ on a 2.05 eV 800 nm thick CuInGaS₂ photocathode integrated on FTO and (Inset) optical image of the photoelectrode (scale bar = 1 cm). (d) Absorption spectra of 2.05 eV CuInGaS₂ and 1.67 eV CuGaSe₂ baseline absorbers.

v. Conclusions

We developed a two-step synthesis technique in which a Cu(In,Ga)Se₂ precursor deposited on FTO is subsequently converted into a wide band gap Cu(In,Ga)S₂ absorber using a close-space sulfurization (CSS) process. The success of this approach relied on the “poor” crystallographic ordering of the Cu(In,Ga)Se₂ precursor co-evaporated at low-temperature which facilitate the diffusion of sulfur into the film bulk. To preserve FTO’s optical and electrical properties, the CSS process was sequenced in two individual steps, a low-temperature annealing in sulfur vapor followed by a high-temperature crystallization under inert atmosphere. Raman, XRD, EDXS and UV-visible spectroscopy techniques confirmed that selenium was substituted with sulfur in the Cu(In,Ga)Se₂ precursor lattice, while TEM imaging and TEM-EDX profiles confirmed that little to no inter-diffusion took place at the CuInGaS₂/FTO interface. Photoelectrodes made of 800 nm-thick 2.05 eV CuInGaS₂ absorbers were found to be p-type, with a flat-band potential of +500 mV_{RHE} and capable of generating up to -5.25 mA/cm₂ at saturation. This photocurrent density value, corresponding only to 38% of the theoretical limit, appears to originate from sub-par optical absorption properties of CuInGaS₂ when compared to those of other chalcopyrite solar absorbers (Figure 26.d), including our baseline CuGaSe₂ thin film materials.

e. Wide band gap Cu(In,Ga)S₂ absorbers from Cu-In-Ga metallic precursors

i. Overview

In this task, our team adapted a known method reported by the PV community⁴⁹ to create band gap tunable Cu(In,Ga)S₂. In this approach, metallic elements (Cu, In, Ga) were co-evaporated first onto a substrate and then subjected to a sulfurization treatment to form semiconducting Cu(In,Ga)S₂. Series of depositions were first performed to establish a baseline in order to create 1.5 eV Ga-free CuInS₂. Copper and indium were deposited either simultaneously, or stacked (copper first or indium first). We concluded that the higher the copper to indium ratio, the easier the sulfurization process. Best results were achieved with [Cu]/[In]~1.2-1.3. However, such high copper content led inevitably to the formation of un-wanted Cu₂S, requiring post sulfurization etch with KCN. Subsequent tests were performed with Cu-In-Ga alloys to widen the optical band gap. Our results evidenced that single phase Cu(In,Ga)S₂ was formed through inter-diffusion of In and Ga between CuInS₂ and CuGaS₂ phases, produced sequentially at different stages of the sulfurization process. Best performing Cu(In,Ga)S₂ absorbers synthesized via this method generated up to 12 mA/cm² for a band gap energy of 1.8 eV. Similarly to CuGa(S,Se)₂, we discovered that Cu(In,Ga)S₂ fabricated with copper-rich metallic precursors led to absorbers with poor sub-band gap optical transmission, typically below 35%.

ii. CuInS₂ thin film processing and PEC/PV characterizations

Copper-indium alloys were deposited by co-evaporation with no intentional substrate heating and then sulfurized in a subsequent annealing step to form Cu(In,Ga)S₂ films (Figure 27.a). This synthesis route is attractive for our purposes as it avoids large thermal budgets that may degrade an underlying solar cell if integrated into a tandem device and has the potential to be scaled up. As a preliminary proof-of-concept test, we focus on CuInS₂ first as they would produce the less complex yet structurally identical parent material of Cu(In,Ga)S₂. Films were grown on Mo using excess copper (in form of additional Cu layer deposited on top of the Cu-In alloy layer), with a target [Cu]/[In] ratio of 1.2. Lower ratios were found to limit sulfur diffusion/incorporation, leading to partially sulfurized films. Samples were then sealed in a close capsule with sulfur (200 mg) and annealed at 575°C for 60 minutes. As a result of the sulfurization process, excess Cu₂S was observed by Raman analysis, as seen in Figure 27.b, and subsequently etched with KCN. Overall, this approach led to high quality CuInS₂ with large grains that in some cases span the entire film thickness (Figure 27.c). It is also noteworthy that the underlying molybdenum is minimally sulfurized during this process, with MoS₂ thicknesses in the order of 150 nm or less.

Newly formed CuInS₂ samples were then integrated as solar cells using standard CdS n-type buffers (typically 80 nm thick), sputtered intrinsic/resistive ZnO (100 nm) and reactively sputtered ITO (200 nm). The latter was performed using a shadow mask comprising sixteen 0.12 cm² holes and placed directly in contact with the sample, leading to 16 individual solar cells on a single 1”x1” sample. Figure 28.a presents the J-V curves measured on 12 out of the 16 cells (4 cells were electrically shorted). The open circuit potentials ranged from 667 mV to 741 mV, with an averaged value of 710 mV. It is worth mentioning the wide spread in solid-state properties measured across this particular sample, as revealed by the short circuit photocurrent density ranging from 12 to 20 mA/cm².

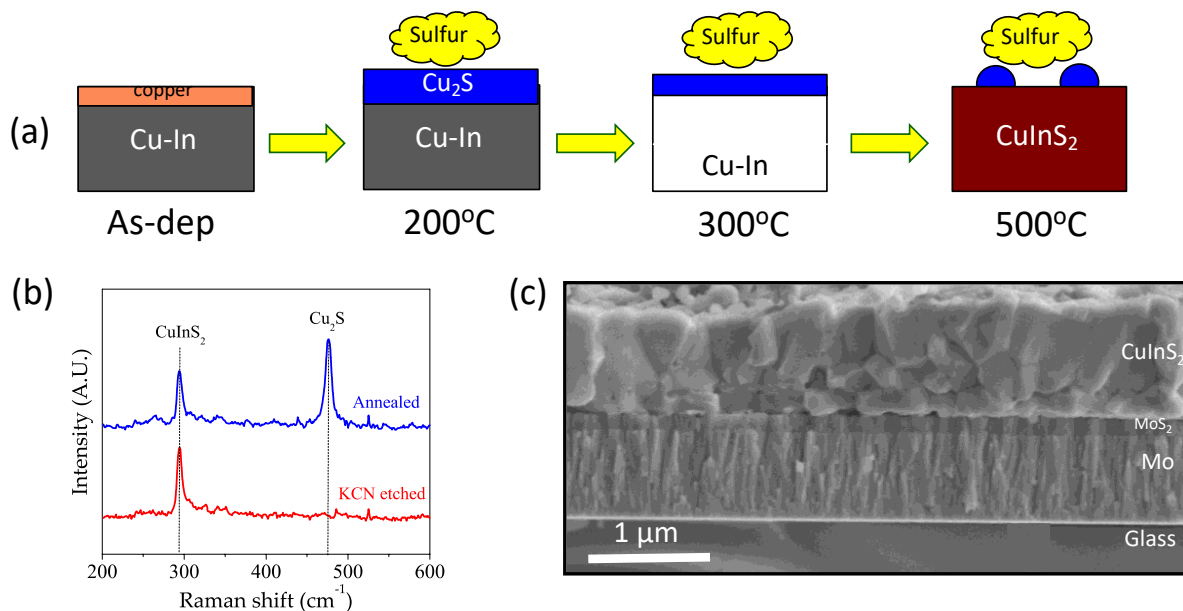


Figure 27. (a) CuInS₂ thin film processing. (b) Raman shift measured on CuInS₂ before and after KCN etch. (c) SEM cross-sectional view of CuInS₂ integrated on Mo substrate.

Figure 28.b presents the quantum efficiency measured on one particular CuInS₂ cell which J-V curve is highlighted in red in Figure 28.a. It can be seen that the conversion efficiency increases sharply near 370nm when ZnO and ITO become transparent. The absorption cut off from CdS is also observed at about 475 nm. At 550 nm, the conversion efficiency reaches a maximum of 68%. Then the QE drops suddenly, revealing possible recombination phenomena in the absorber. Eventually, the QE drops to zero at about 850 nm. The derivative of the QE vs. excitation wavelength was used to determine the absorber band gap. A maximum was reached at 807 nm, indicating a bandgap of 1.55 eV for this absorber. This value coincides well with the expected bandgap for CuInS₂. The same sample was further coated with Ru nanoparticles HER catalyst and cut into small pieces to form individual PEC devices. The PEC characteristic of the device which EQE is shown in Figure 28.b is presented in Figure 28.c. A maximum photocurrent density of 12.5 mA/cm² was achieved, in good agreement with integrated EQE data (15 mA/cm²). Finally, a E_{ONSET} as high as 900 mV vs. RHE was achieved, corresponding to the highest value reported so far on any chalcopyrite-based PEC device.

iii. Band gap tunable Cu(In,Ga)S₂ thin film synthesis and PEC/PV characterization

With this baseline process established, we then focused our efforts on the synthesis of band gap tunable Cu(In,Ga)S₂. A similar approach was used, with the exception of gallium being added during the co-evaporation process (Figure 29.a). We established that Cu(In,Ga)S₂ was formed through different stages during the sulfurization process. First, part of the copper reacted with indium at around 300°C to form single phase CuInS₂ (Figure 29.b). As the temperature increased during the sulfurization process, the remaining copper reacted with gallium to form CuGaS₂ at around 550°C (Figure 29.b) and SEM cross-sectional analyses (Figure 29.c). Eventually, a single phase Cu(In,Ga)S₂ layer was formed at around 600°C, through Ga and In interdiffusion between the CuInS₂ and CuGaS₂ layers (Figure 29.b and Figure 29.d).

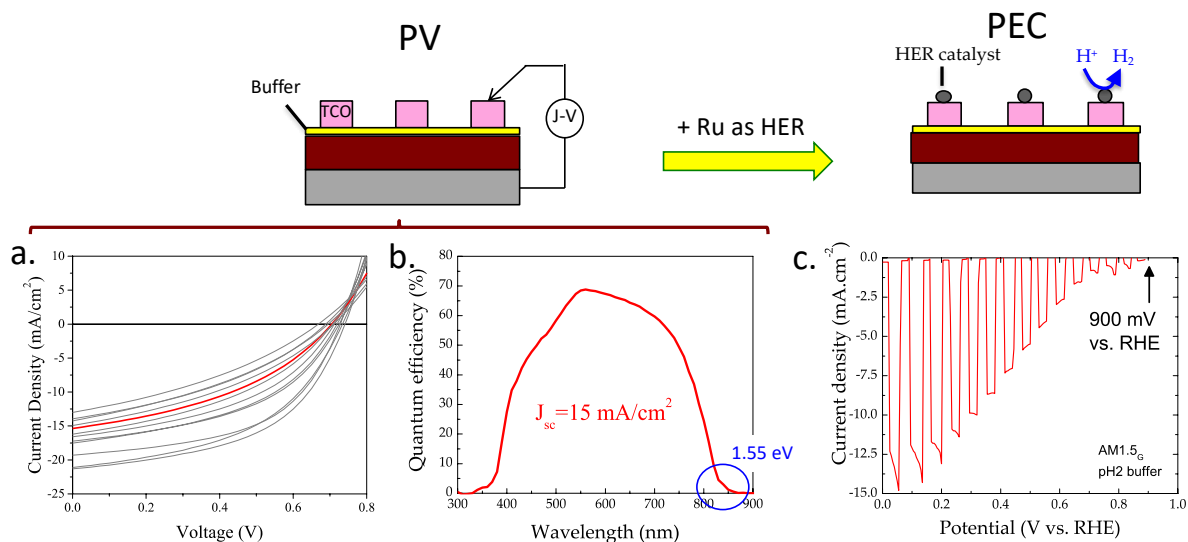


Figure 28. (a) J-V characteristics measured on 12 CuInS₂ cells integrated on a 1”x1” Mo-coated glass substrate. (b) EQE measured on a CuInS₂ cell which J-V characteristic is highlighted in red in (a). (c) LSV measured on the same CuInS₂ cell in PEC configuration using Ru nanoparticles as HER catalyst.

The PEC performances of wide band gap Cu(In,Ga)S₂ were then accessed. Figure 30.a presents the LSV measured on a sample with a GGI ratio of 0.32. A E_{ONSET} of 0.1 V vs. RHE and a saturation photocurrent density of 10.5 mA/cm² at -0.4 V. vs RHE were observed. Subsequent IPCE data measured at -0.285 V vs. RHE revealed relatively high photoconversion efficiency in the visible part of the solar spectrum, with IPCE values in the 40-60% range (Figure 30.b). The derivative of the IPCE data near the cutoff region indicated a band gap energy value of 1.71 eV. Integrated the IPCE curve over AM1.5G led to a current density of approx. 8 mA/cm², in good agreement with LSV measurements.

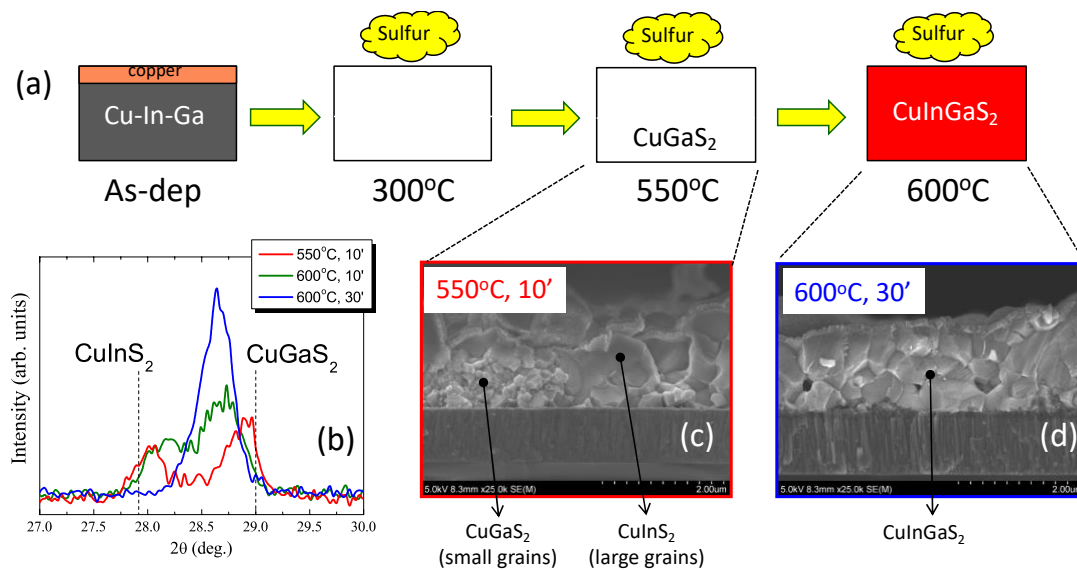


Figure 29. (a) Cu(In,Ga)S₂ thin film processing. (b) Diffraction pattern measured on Cu(In,Ga)S₂ at different stages of the sulfurization process with (c,d) matching SEM cross-sectional views.

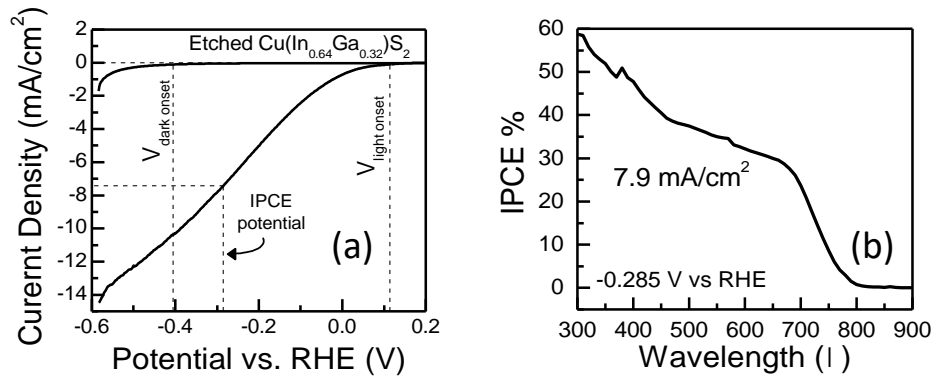


Figure 30. (a) LSV and (b) IPCE measured on a 1.7 eV CuInGaS₂ photocathode.

In the final phase, the GGI ratio was slightly increased during precursors co-evaporation to yield Cu(In,Ga)S₂ with higher band gap energies. The cross-sectional SEM view in Figure 31.a of a fully integrated Cu(In,Ga)S₂ solar cells also revealed minimal MoS₂ interfacial layer growth during precursors sulfurization, as observed with CuInS₂. The resulting Cu(In,Ga)S₂ film was dense, void-less and made of grains 400-600 nm across. The EQE measured on films indicated very good conversion efficiency, with EQE values up to 80% at 500 nm wavelength (Figure 31.b). Integrated EQE data led to short-circuit photocurrent density of 12 mA/cm² for a 1.8 eV chalcopyrite absorber, the highest value achieved during this research program.

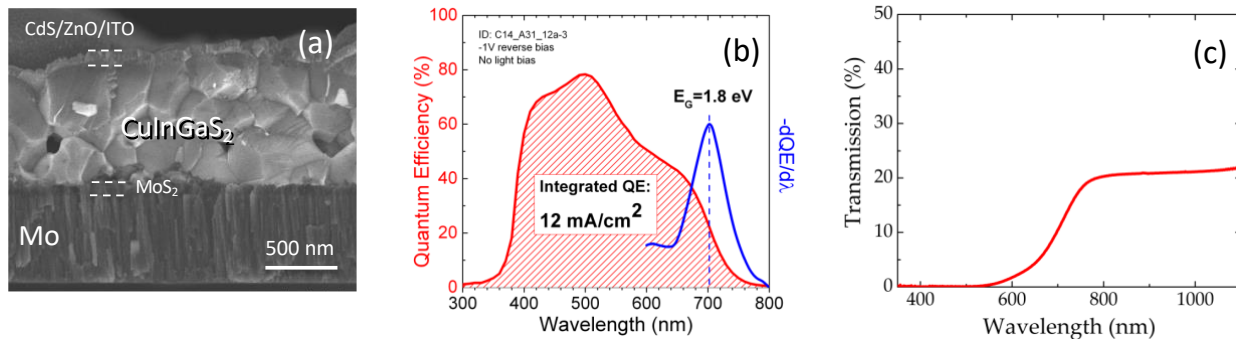


Figure 31. (a) SEM cross-sectional view and (b) EQE curve of a fully integrated 1.8 eV CuInGaS₂. (c) Typical transmission curve measured on a CuInGaS₂ thin film fabricated from a metallic precursors and deposited a on soda-lime glass substrate.

It should be noted that the resulting Cu(In,Ga)S₂ had very poor sub-band gap optical transmission (< 30%), as evidenced in Figure 31.c. In a tandem device application, such low transparency would reduce the photocurrent produced by the underlying cell(s), reducing the efficiency of the device. Upon further investigation, it appears that the cause for such low sub-band gap transmission is the high copper concentration required with this synthesis technique (CGI>1.2), a phenomena also observed with CuGa(S,Se)₂ (see Section 3.c.ii). We speculate “d-d excitations” at copper centers to be responsible for this phenomena, yet additional theoretical modeling and testing is required. Since growing metallic precursors with CGI<1 would not yield to fully sulfurized absorbers, this technique was eventually abandoned by our group.

4. Technical achievements in Task 2 “Sub-surface energetics improvement”

a. Surface and interface characterization by photoelectron spectroscopy

This task was performed to investigate the chemical and electronic properties of chalcopyrite thin films for photoelectrochemical (PEC) water splitting. For this purpose, the UNLV team has utilized a suite of experimental techniques, both in the lab at UNLV and at Beamline 8.0.1 at the Advanced Light Source (ALS), Lawrence Berkeley National Laboratory, to derive a comprehensive picture of surfaces and interfaces of the chalcopyrite-based PEC system. Experiments include studies to investigate electronic structure properties (such as band gaps and band alignments) and to gain insights into the chemical properties of liquid/chalcopyrite interfaces. Experimental techniques include a number of different soft x-ray and electron spectroscopies: X-ray photoelectron (XPS) and X-ray emission (XES) spectroscopy for the determination of the surface and near-surface chemical structure, respectively, as well as complementary ultraviolet photoelectron (UPS) and inverse photoemission (IPES) spectroscopy. The combination of these techniques provides detailed information about the surface chemical properties, surface band edge positions, work function, and surface electronic band gap.

i. Chemical characterization of Cu(In,Ga)S₂ absorber and CdS buffer layer surfaces

Preliminary work included “zeroth-round” XPS, UPS, and IPES measurements and analysis of two sample sets received from UH. In addition, XES measurements and analysis of a separate sample series, which included a crystallized and non-crystallized absorber pair, were performed. The goal of the initial XPS, UPS, and IPES experiments was to establish sample handling and shipping procedures to minimize surface exposure to ambient conditions, to test for unexpected elements at the surface, and to prepare a detailed and optimized experimental series to derive the electronic structure of the CdS/Cu(In,Ga)S₂ interface. The first sample set consisted of two different samples: one Cu(In,Ga)S₂ (CIGS) “bare” absorber (CIGS_22A) and one CIGS absorber with a CdS buffer layer (CIGS/CdS_22B) on a Mo-coated soda lime glass substrate. After brief air exposure and/or rinsing, the samples were vacuum-sealed and shipped to UNLV. Upon arrival, the samples were immediately unpacked in a N₂ glove box, mounted, and moved into the ultra-high vacuum chamber for measurement. XPS survey spectra indicate a significant presence of surface oxides on the bare absorber surface, while the CdS surface was found to be more pristine. Furthermore, we found a significant Na signal on the absorber surface. The Na signal is a common finding on chalcopyrite PV absorber surfaces and generally either due to the diffusion of Na from the soda-lime glass substrate or Na-containing additions during the growth process. Interestingly, we also found a significant (yet smaller) Na signal on the CdS surface, in contrast to most other systems that have been studied by the UNLV team.

An initial XPS survey spectrum of the “as-received” absorber surface and that of the full-thickness CdS buffer layer surface is shown in Figure 32. The survey spectrum displays all expected absorber-related photoemission and Auger lines (i.e., of Cu, In, Ga, and S for the absorber surface, and Cd and S for the buffer layer surface). The XPS survey spectrum also indicates a notable presence of oxygen (and, to a lesser extent, carbon) on the absorber surface.

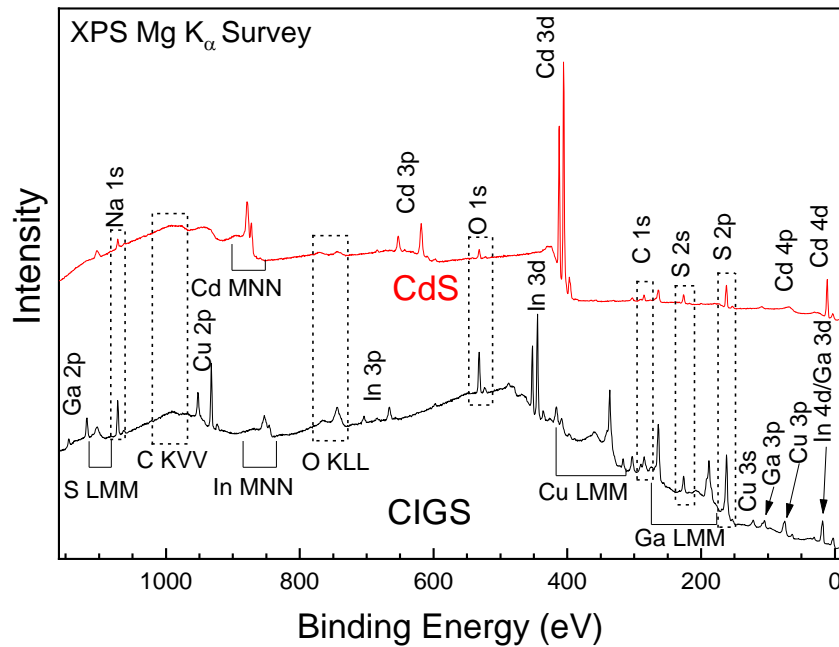


Figure 32. Mg K_{α} X-ray photoelectron spectroscopy (XPS) survey spectra of a “bare” Cu(In,Ga)S₂ absorber and a CdS/CIGS interface sample.

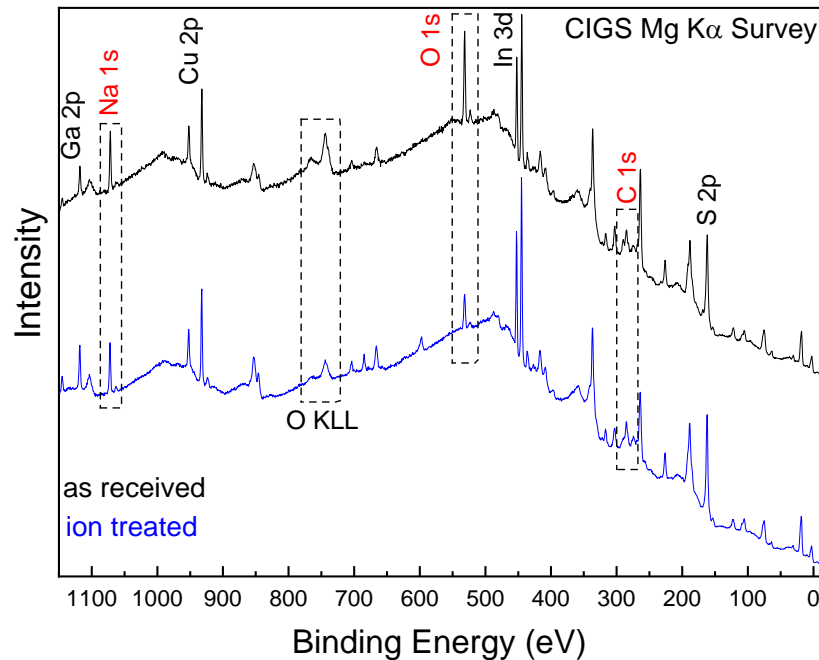


Figure 33. Mg K_{α} X-ray photoelectron spectroscopy (XPS) survey spectra of a Cu(In,Ga)S₂ absorber, highlighting the reduction in signal of surface adsorbates (primarily oxygen) after ion treatment.

Additionally, we tested the effectiveness of our low-energy (50 eV) Ar⁺ ion treatment at removing surface adsorbates (Figure 33). XPS survey spectra were acquired after the ion treatment and show a reduction (but not removal) of the oxygen signal at the surface of the bare absorber (the CdS buffer layer remained virtually unchanged after treatment). Initial XPS survey spectra also

indicated a significant sodium (and carbon) signal on the CIGS absorber. In contrast to our experience with other chalcopyrite absorbers, however, the ion treatment did not lead to an appreciable change in the intensity of the sodium (or carbon) signal, suggesting that the Na (and C) is more strongly bound than a “simple” surface adsorbate. In contrast, a small yet significant Na signal was found on the initial XPS survey spectra of the CdS surface, and an observed reduction of the Na signal after ion treatment suggests that the Na atoms were weakly bound at the CdS surface.

Also, within the first project year, the world-wide first XES measurements of a solid/liquid interface of a PEC material were collected at the ALS in our custom-designed *in situ* cells. Such measurements allow for the characterization of the solid/electrolyte interface between custom-deposited CIGS thin films on Au-coated, C-based membranes and a highly acidic, sulfur-free electrolyte. The S L_{2,3} XES spectra of the first two solid/liquid interface experiments, along with corresponding reference samples, are shown in Figure 34.

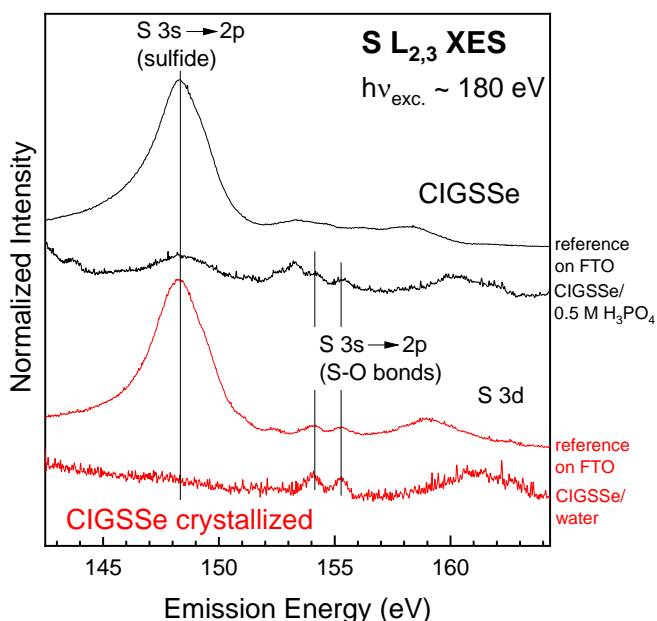


Figure 34. S L_{2,3} soft x-ray emission spectroscopy (XES) of CIGSSe samples. Top (black): Sulfurized “CIGSSe” sample, both as a reference on an FTO substrate, and as a solid/liquid interface with a 0.5 M H₃PO₄ electrolyte solution. Bottom (red): Sulfurized and crystallized CIGSSe sample (“CIGSSe crystallized”), measured as a reference on FTO and at the solid/liquid interface with water.

ii. Chemical characterization of several chalcopyrite-based absorber surfaces

The second sample set received from UH consisted of 4 new samples: a CuInGa metal alloy (“CIG”), a sulfurized CuInGa metal alloy (“CIGS”), an as-deposited CuGaSe₂ (“CGSe”), and a sulfurized CuGaSe₂ film (“CGSSe”). The XPS survey spectra of the four different absorber surfaces are shown in Figure 35. Detailed spectra were recorded for each pertinent peak. The goal of these experiments was to identify the magnitude and origin of any possible contamination, chiefly carbon, oxygen, and sodium, on and in several different absorber films. As shown in Figure 35, all expected metal lines (i.e., of Cu, In, and/or Ga) are found. However, the CIGS sample

clearly stands out, in that the Cu signal is substantially attenuated (most likely due to the oxygen-rich surface layer), while the In and Ga signals are very strong. Our XPS study of the first sample set indicated a significant presence of sodium on the CIGS absorber, as well as a smaller (yet appreciable) sodium signal on the surface of the CdS/CIGS interface sample. Conversely, as shown in Figure 36, only negligible amounts of sodium are found at the surface (if any) for the entire second sample series.

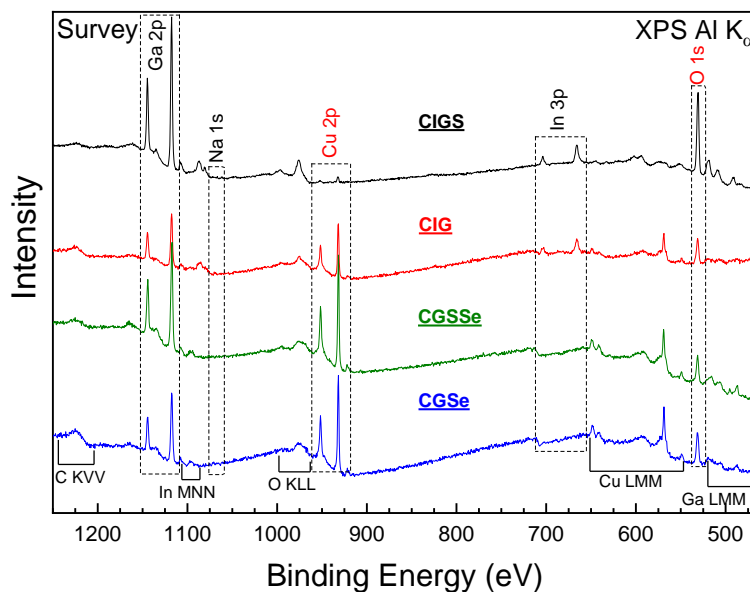


Figure 35. Mg K_{α} XPS survey spectra of the four samples from the second sample series.

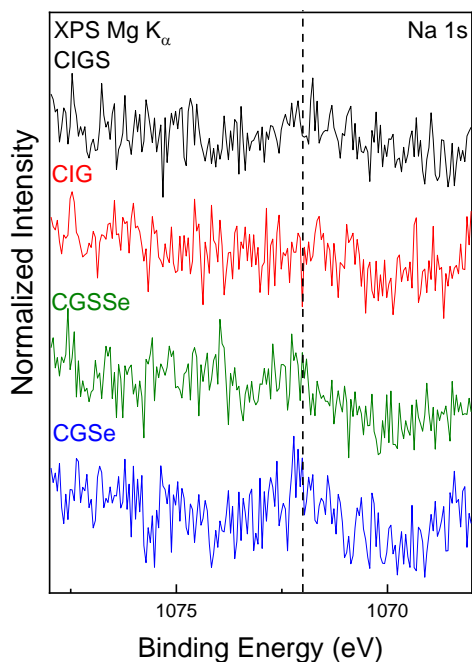


Figure 36. Detailed spectra of the Na 1s peak obtained from the second sample series. Only negligible amounts of sodium are found at the surface (if any).

iii. Chemical and electronic characterization: band alignment at the CdS/CIGS interface

In a continued effort to characterize the electronic surface of the CdS/Cu(In,Ga)S₂ interface, a sample series was specifically “designed” to allow for determination of the electronic structure, including the band alignment and band gaps at the junction. The sample series consisted of Cu(In,Ga)S₂ (CIGS) absorbers with CdS buffer layers of varying thickness (deposited using chemical bath deposition, CBD). More specifically, this third sample series consisted of six samples: a sulfur-free CuInGa metal alloy (“CIG”), a sulfurized CuInGa metal alloy (“CIGS”) etched with KCN, and four samples consisting of CdS buffer layers with increasing thickness, deposited on the CIGS substrate (“CdS/CIGS”) by CBD. The buffer layer thicknesses are defined by a variation of the deposition time: 30 secs, 1 min, 2 min, and 6 min (full CBD time), respectively. The 6 min sample was further treated by annealing at an elevated temperature (120°C, 7 min.).

XPS survey spectra shown in Figure 37 display all expected absorber-related signals (Cu, In, Ga, and S) on the CIGS surface, as well as Cd lines on the 30 sec, 2 min, and 6 min CdS/CIGS samples, which increase in intensity with buffer layer thickness. The increase in CBD time leads to an increase in Cd intensity, in parallel to a continuous attenuation of absorber-related peaks (as expected). The absence of absorber-related signals (Cu, In, Ga) in the CdS XPS spectra suggests that the CdS layer is closed and sufficiently thick to act as a benchmark sample for a detailed electronic structure study. In addition, CIGS-related signals are still detected for the thinnest buffer layer thickness, and hence this sample will complement the set for a complete derivation of the band alignment, since it will enable us to monitor the interface-induced band bending, both in the absorber as well as the buffer. Below, this data will be combined with the results for valence band maximum (VBM) and conduction band minimum (CBM) obtained with UPS and IPES, respectively.

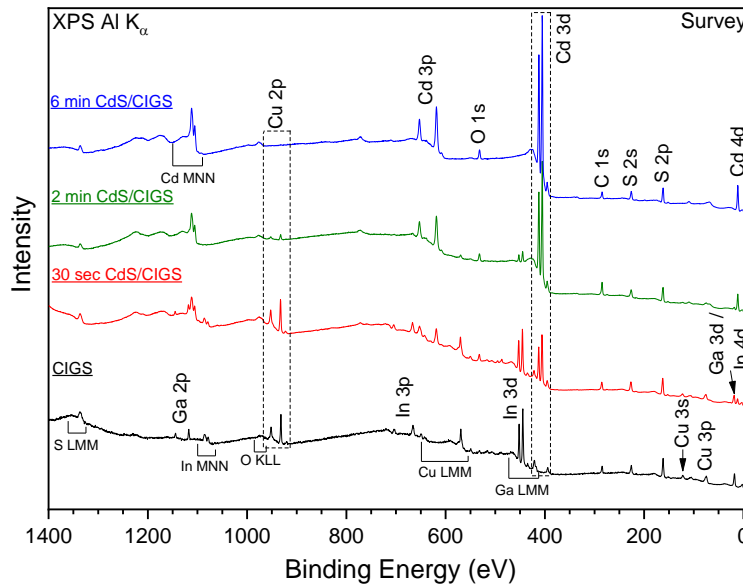


Figure 37. Al K_α XPS survey spectra of a Cu(In,Ga)S₂ absorber (“CIGS”) and three additional CdS/CIGS samples with increasing buffer layer thickness (CBD times of 30 seconds, 2 minutes, and 6 minutes, respectively).

Initial XPS survey spectra also show the CIGS surface to exhibit substantially less oxidation (attributed to the post-sulfurization KCN etching) than in the results of the prior sample series. Low-energy Ar⁺ ion treatments, using 50 eV Ar⁺ ions, were again employed for surface cleaning, thus allowing subsequent XPS measurements with a reduced impact of surface adsorbates. The 30-minute (in total) ion-treated surfaces were used to derive the interface-induced band bending, as seen in shifts of core-level peaks between the absorber surface and the intermediate-thickness sample, as well as between the intermediate-thickness sample and the fully formed buffer surface. In detail, the interface-induced band bending can be inferred by comparing different combinations of core-level peak positions of the CIGS absorber (Cu 2p, In 3d, Ga LMM) and the CdS buffer (Cd 3d, S 2p).

Further, UPS and IPES measurements were performed to derive the VBM and CBM of the CIGS absorber and the full-thickness 6 min CdS/CIGS sample (Figure 38). We find VBMs of -0.60 ± 0.10 eV and -2.07 ± 0.15 eV for CIGS and CdS, respectively. Furthermore, the observed CBMs of 1.01 ± 0.15 eV for CIGS and 0.41 ± 0.15 eV for CdS suggest the presence of a significant cliff in the conduction band, likely even after the interface-induced band bending corrections are included (see below). For a tentative determination of the surface electronic band gaps, we find 1.61 ± 0.18 eV for the CIGS absorber surface and 2.48 ± 0.18 eV for the CdS surface.

As mentioned, the UPS and IPES measurements of the VBM and CBM of the CIGS absorber and the fully formed CdS/CIGS sample need to be interpreted in view of band bending changes during the interface formation to derive the full electronic structure picture. The resulting band alignment at the CdS/CIGS interface is shown in Figure 39. Even after taking the interface-induced band bending corrections (oval) into account, the observed CBMs for the CIGS and CdS surfaces show the presence of an appreciable “cliff” in the conduction band (0.40 eV), whereby the CBM of the buffer lies below that of the absorber. This type of alignment can encourage electron-hole recombination at the interface, which hinders device efficiency by potentially lowering the open-circuit voltage of the cell.

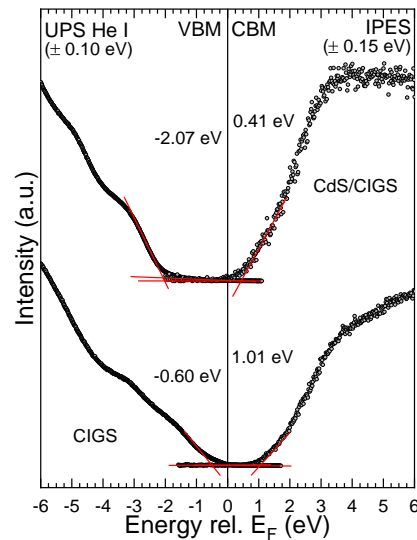


Figure 38. UPS (left) and IPES (right) spectra of the Cu(In,Ga)S₂ absorber (bottom), as well as the thinnest (30 sec) and thickest (6 min) CdS/CIGS interface samples. Red lines indicate the band edges approximated by linear extrapolation, and the numerical results are listed.

The last steps in this project included measurements and analysis of a second sample series specifically “designed” to allow for determination of the electronic Cu(In,Ga)S₂ surface and CdS/Cu(In,Ga)S₂ interface structure by combining results obtained from XPS, UPS, and IPES measurements. The goal of these experiments was to emulate the results from the previous band alignment investigation with optimal sample preparation and handling. This “trophy” sample series consisted of five samples: a sulfurized CuInGa metal alloy absorber etched with KCN (“CIGS”), three samples consisting of CdS buffer layers with increasing thickness (“CdS/CIGS”), deposited on the CIGS absorber by CBD (30 sec, 2 min, and 6 min deposition time), and a second 6 min buffer layer sample that was further treated by annealing in air at 120°C for 7 minutes.

An initial XPS survey spectrum of the “as-received” absorber surface is shown in Figure 40, bottom. The survey spectrum displays all expected absorber-related photoemission and Auger lines (i.e., of Cu, In, Ga, and S). The XPS survey spectrum also indicates a notable presence of carbon (and, to a lesser extent, oxygen) on the absorber surface. In comparison to previously measured CIGS absorber samples provided by UH, the survey spectrum indicates a more Cu-rich surface (note the Cu 2p peaks) even after etching in KCN (which has been shown to remove copper sulfide from the surface).

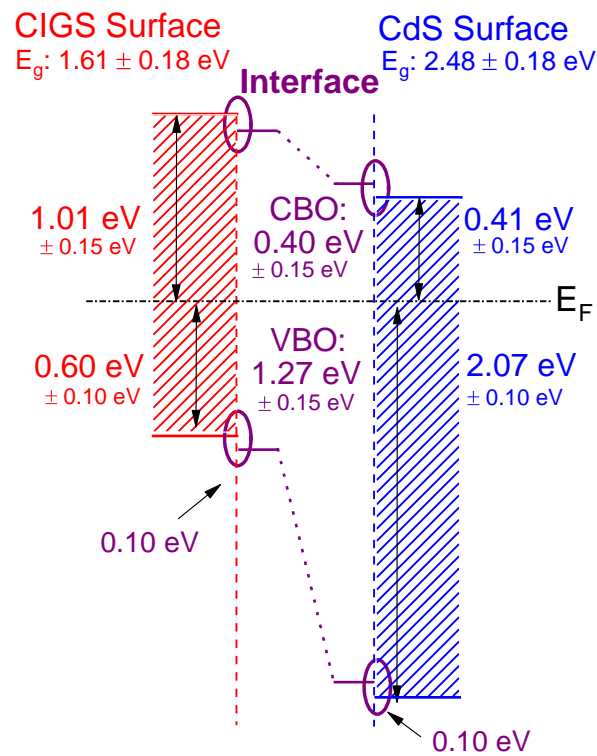


Figure 39. Schematic representation of the band alignment at the CdS/CIGS interface. The far left and right depict the band edge positions at the CIGS and CdS surfaces, respectively. In the center, the derived band alignment at the interface is shown after taking interface-induced band bending changes (ovals) into account.

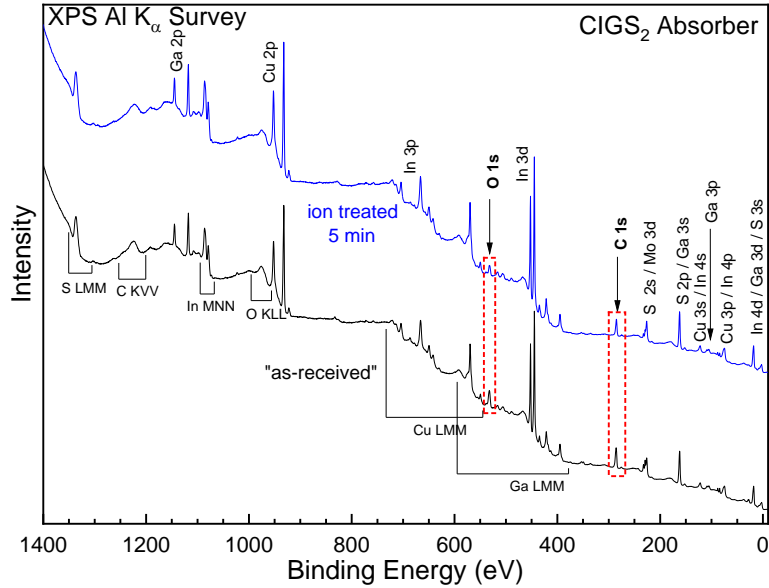


Figure 40. Al K_{α} XPS survey spectra of the “as-received” $\text{Cu}(\text{In,Ga})\text{S}_2$ absorber surface (black) and the 5 min ion treated $\text{Cu}(\text{In,Ga})\text{S}_2$ (blue). O and C 1s peaks are highlighted.

Low-energy ion treatments were employed using 50 eV Ar^+ ions to remove weakly-bound surface adsorbates by means of ion-stimulated desorption, thus allowing for subsequent spectroscopic measurements with reduced signal attenuation due to surface adsorbates. The XPS survey spectrum after a short (5 min) low-energy ion treatment (Figure 40, top) shows a reduction in the C and O signals with a corresponding increase in all absorber-related lines (Cu, In, Ga, and S) due to reduced attenuation in the carbon- and oxygen-containing adsorbate layer. The full set of survey spectra is shown in Figure 41.

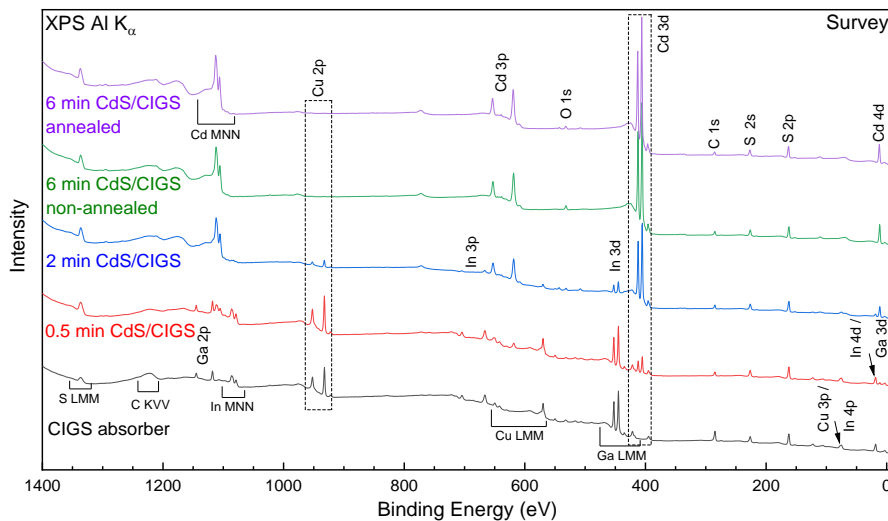


Figure 41. Al K_{α} XPS survey spectra of all five samples from the final sample series: the $\text{Cu}(\text{In,Ga})\text{S}_2$ (CIGS) bare absorber, two intermediate thickness (0.5 and 2 min) CdS buffer layer samples, and the non-annealed and annealed full-thickness (6 min CBD) CdS buffer layer surfaces. Dashed boxes highlight the changes in intensity for an absorber (Cu 2p) and a buffer (Cd 3d) signal as a function of deposition time, which were used to monitor the band bending changes induced by the interface formation.

In conjunction with XPS measurements, UPS and IPES measurements were performed to derive the VBM and CBM of the CIGS absorber surface and the fully formed buffer layer sample. Figure 42 shows the corresponding UPS and IPES spectra. Due to the higher Cu content at the absorber surface, the proper derivation of the band edges is more difficult. Furthermore, we find a significant tailing in the CdS spectra, probably due to defects induced by the drastically different absorber surface. These tails are indicated in Figure 42 with green extrapolations, while the “true” VBM and CBM are approximated by the red lines. With this approach, we find VBMs of -0.73 ± 0.10 eV and -1.80 ± 0.15 eV for CIGS and CdS, respectively. Additionally, we find CBMs of 0.22 ± 0.10 eV and 0.61 ± 0.15 eV for CIGS and CdS, respectively. The defect states of CdS extend all the way to -0.43 eV for the valence band, and 0.22 eV for the conduction band. For the surface electronic band gaps, we hence find 0.95 ± 0.18 eV for the CIGS absorber surface and 2.41 ± 0.18 eV for the CdS surface (when ignoring the defect states).

This is an unusually small surface band gap for a CIGS absorber – typically, high-efficiency chalcopyrite absorber surfaces show band gaps in the range of 1.3 - 1.5 eV. We ascribe this finding to the high Cu surface content, seen both in the survey spectra of Figure 40, Figure 41 and Figure 42, as well as in the Cu 3d-derived peak in Figure 42 (at ~ -3 eV), we speculate that there is a presence of copper sulfide species as well. In that case, the observed band gap would have to be ascribed to the lowest-band gap species found at the surface (with sufficient concentration), most likely the copper sulfide.

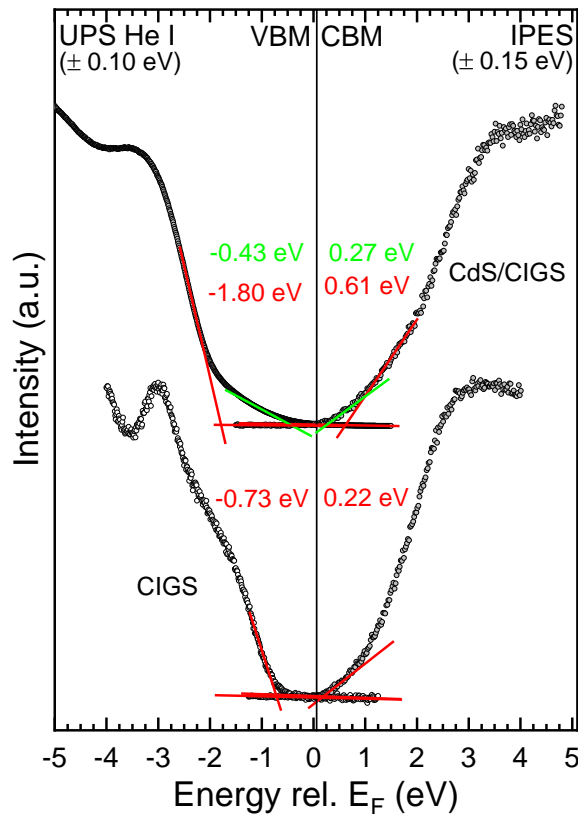


Figure 42. UPS (left) and IPES (right) spectra of the Cu(In,Ga)S₂ absorber (bottom), as well as the thickest (6 min) CdS/CIGS sample (top). Red and green lines indicate the band edges approximated by linear extrapolation, and the numerical results are listed.

b. Surface treatment of chalcopyrite photocathodes with n-type buffer layers

Pairing up state of the art copper gallium selenide solar cells (max $V_{OC} \sim 730$ mV)⁵⁰ with a state of the art wide band gap solar cell (CuGaSe₂, max $V_{OC} \sim 1,000$ mV)⁵¹ should provide a V_{OC} of approximately 1.7 V. Since the thermodynamic limit of the water splitting is 1.23 V plus approx. 0.4 V in overpotential, this pairing should have sufficient voltage to initiate the reaction. As photocathodes though, state of the art CuGaSe₂ have lagged behind their photovoltaic counterpart, yielding a maximum E_{ONSET} of 0.6 V vs RHE. This section summarizes on our efforts to push the current state of the art of wide band gap chalcopyrites past a E_{ONSET} of 0.6 V vs RHE.⁵² One method that has been shown to consistently increase the E_{ONSET} of CGSe photocathodes is to deposit a layer of cadmium sulfide (CdS) to form a buried junction. Indeed, when employing this method, CdS does increase the E_{ONSET} anodically substantially by 800 mV, matching that reported in [52], as seen in Figure 43.a. Unfortunately, this CdS surface treatment is not stable under PEC testing conditions (even when tested at pH9, a pH in which CdS is usually deposited by chemical bath) as seen in Figure 43.b.

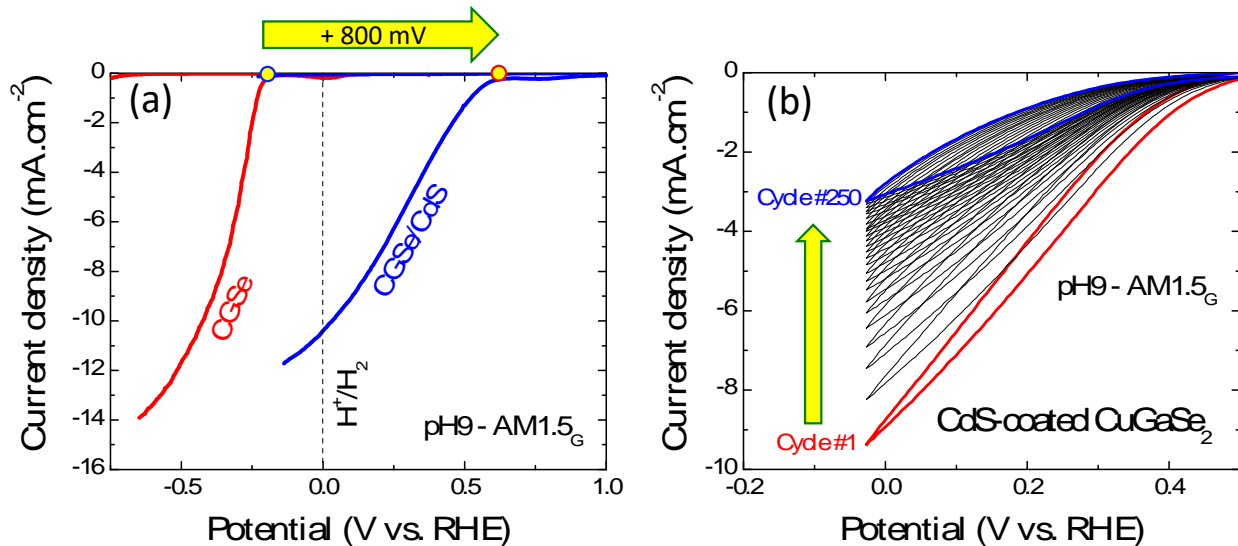


Figure 43. (a) Current voltage characteristics of CGSe photocathodes showing that an +800 mV shift in E_{ONSET} is achieved when coating the photocathode with CdS. (b) Cyclic voltammetry of CGSe/CdS revealing that these state of the art photocathodes degrade even at pH 9.

Indium sulfide (In₂S₃) was then tested as an alternative to CdS. The main motivation for using In₂S₃ was due to it possessing similar optical properties as CdS as shown in Figure 44.a. To fabricate the protective coating on top of the CGSe, an approximately 100 nm thick layer of In₂S₃, seen in Figure 44.b, was deposited by spin coating several drops of a molecular ink composed of thiourea and indium chloride dissolved in methanol. Preliminary linear sweep voltammetry tests, seen in Figure 45.a, demonstrated that compared to bare CGSe photocathodes (black) a coating of indium sulfide actually improved the E_{ONSET} of CGSe (purple). Surprisingly, the coating of indium sulfide increased the E_{ONSET} more than bare CGSe photocathodes with Ru particles on the surface (green). Additionally, CGSe/In₂S₃/Ru photocathodes were stable even after 1000 cycles of cyclic voltammetry in 0.5 M sulfuric acid, seen in the red and blue curves of Figure 45.b.

Note regarding the use of Ru as HER: Pt is normally the catalyst of choice when it comes to improving HER activity of a (photo)cathode. However, we found that adding Pt to the surface of CGSe/In₂S₃ photocathodes actually worsens energetics, leading to a cathodic shift in the V_{ONSET}, as seen in Figure 45.b. In contrast, as seen in Figure 45.a, the addition of Ru did in fact lead to an anodic shift in E_{ONSET} when deposited onto CGSe photocathodes. Similar results were also obtained on a-SiC photocathodes in our previous DOE-funded PEC project, with Ru (Pt) drastically improving (worsening) the energetics of a-SiC towards HER. We concluded at the time that a Schottky barrier would form at the a-SiC/Pt interface, since Pt has a much higher work function than a-SiC. We stipulate that the same phenomena takes place with CGSe/In₂S₃, although additional analyses are required to validate this hypothesis.

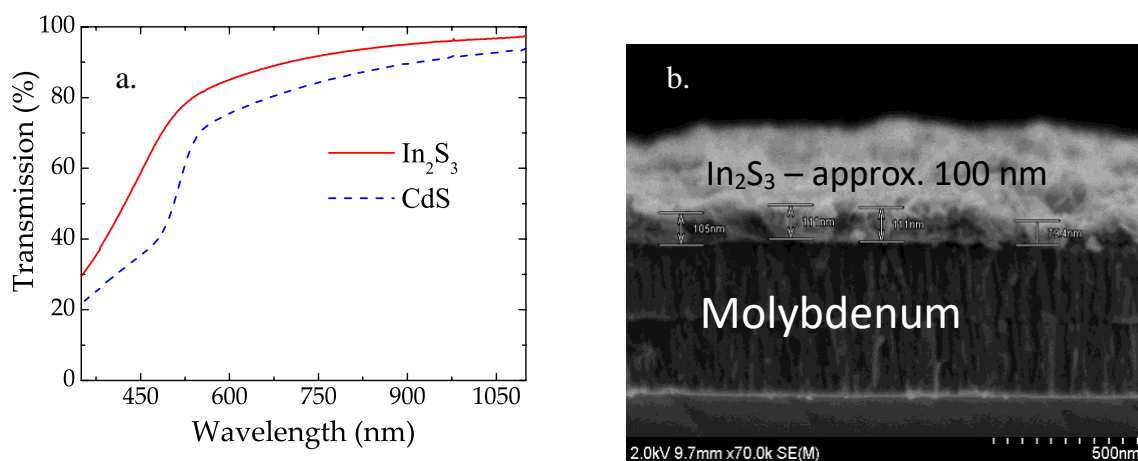


Figure 44. (a) Optical transmittance of a 100-nm thick layer of In₂S₃ demonstrating its similarity to that of CdS (b) An scanning electron microscope (SEM) image of a 100 nm thick layer of In₂S₃ spin-coated onto molybdenum-coated glass.

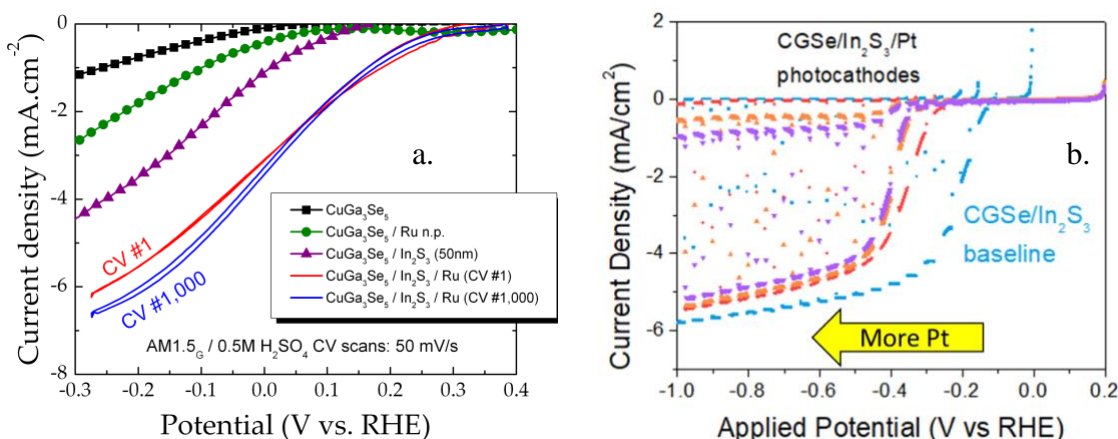


Figure 45. (a) LSV and CV measurements on showing that In₂S₃ keeps CGSe photocathodes stable for up to 1,000 CV cycles. (b) Several LSV scans showing that as more platinum is added to CGSe/In₂S₃ photocathodes, the more the E_{ONSET} shifts anodically.

Alkali treatments of chalcopyrite photocathodes were also tested as a mean to improve energetics. As seen in Figure 46.a, the E_{ONSET} did in fact significantly increase anodically when an optimal amount (similar performance between 23 and 30 nm) of NaF was deposited immediately after

finishing the CGSe layer deposition. The same LSV behavior is observed whether the NaF is deposited before or after the CGSe deposition. However, pre-CGSe NaF samples exhibited issues with adhesion if exposed to high temperatures, as seen in Figure 46.b. After several attempts to rectify the issue, the pre-CGSe NaF deposition was abandoned and only post-CGSe NaF was utilized for the remainder of the study.

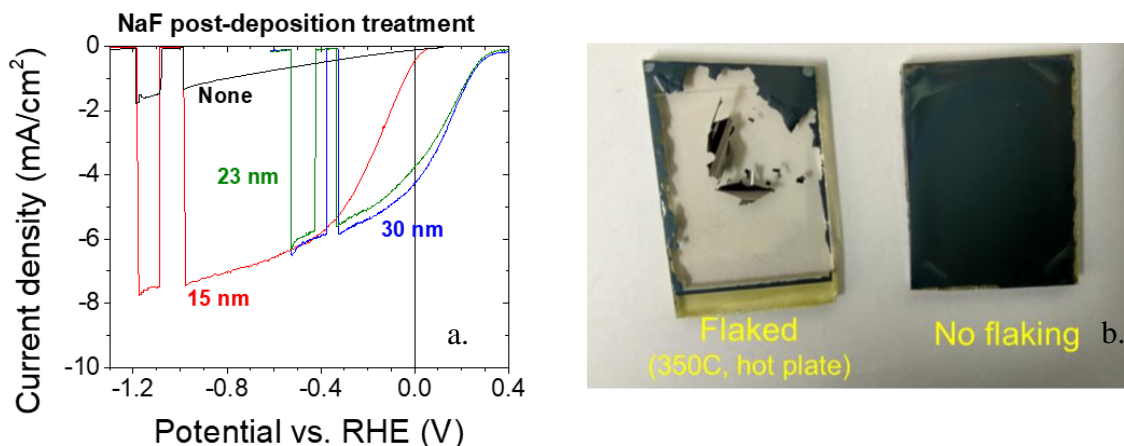


Figure 46. (a) LSV scans of photocathodes that received a NaF post-CGSe deposition showing that an optimal anodic E_{ONSET} shift is achieved between 23-30 nm of NaF. (b) A photograph demonstrating that pre-CGSe NaF samples (left) faced adhesion issues whereas post-CGSe NaF samples (right) did not.

Finally, we applied all the aforementioned treatments (NaF, CdS, In_2S_3 and Ru) to several CGSe photocathodes and measured their PEC performance by LSV, seen in Figure 47. The E_{ONSET} for most fully-treated photocathodes fell between 0.5-0.6 V vs RHE. Although we were successful in finding a coating that was substantially more stable (In_2S_3) than CdS, the E_{ONSET} of these fully-treated CGSe photocathodes were found to not provide enough voltage to split water coupled with a CIGS solar cell (see section 6.b for more details).

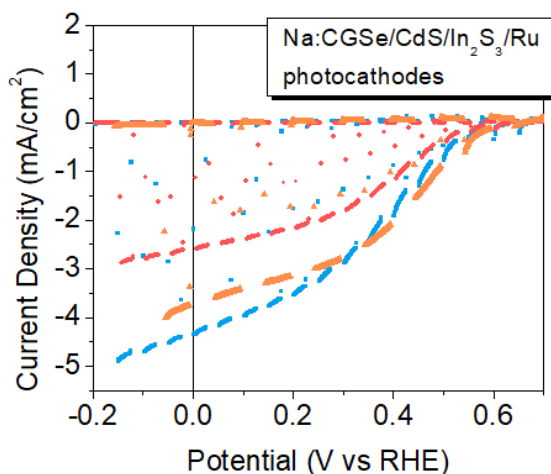


Figure 47. LSV scans of fully-treated CGSe photocathodes showing that most exhibited an E_{ONSET} between 0.5-0.6 V vs RHE.

5. Technical achievements in Task 3 “Surface catalysis and corrosion resistance”

a. ALD MoS₂ development

In our efforts to provide long-term durability enhancement to CGSe photocathode devices, we developed an atomic layer deposition (ALD) approach to depositing molybdenum disulfide (MoS₂) coatings. The first step of this approach involves an O₂ plasma-enhanced ALD process utilizing molybdenum hexacarbonyl as metal precursor for the deposition of molybdenum oxide (MoO_x). Conversion of the surface layers of this coating to MoS₂ is achieved through a sulfidization annealing procedure in a 10% H₂S/ 90% H₂ atmosphere in a tube furnace heated to 200-250°C and held for 1-2 hrs. Evidence for this conversion is provided in Figure 48.a, where the presence of the Mo₄₊ state and the S₂₋ state appear in the Mo 3d and S 2p XPS spectra, respectively (data measured at Stanford). A CGSe sample coated in this fashion is an active PEC device and remains active over the course of 500 illuminated cyclic voltammetry (CV) photoelectrochemical cycles in 0.5 M sulfuric acid (Figure 48.b). In Figure 48.c, we present XPS evidence that the MoS₂ motif remains on the sample surface after 500 CV cycles.

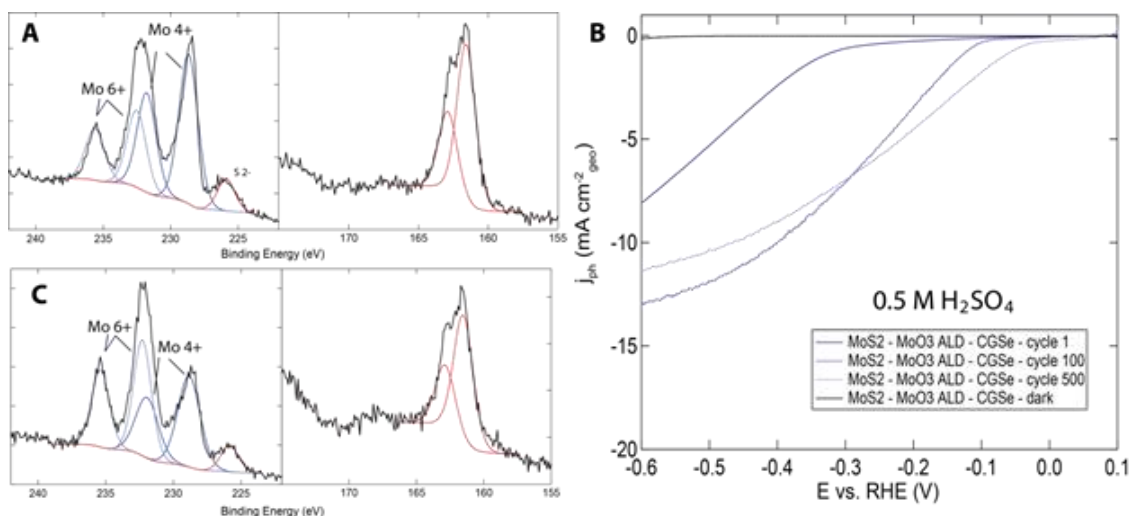


Figure 48. (a) XPS spectra of MoS₂/MoO_x/CGSe before electrochemical stability testing. (b) LSVs during an illuminated potential cycling stability test of the MoS₂/MoO_x/CGSe photocathode. (c) XPS spectra of MoS₂/MoO_x/CGSe after 500 CVs of electrochemical stability testing. All data were measured by the Jaramillo group at Stanford.

This coating strategy was then applied to a CGSe device that had been treated with a CdS buffer layer for improved photovoltaic activity, and this treatment resulted in an active PEC photocathode with onset potential near +0.4 V vs. RHE (Figure 49.a, blue curve). The durability of the CGSe/MoO_x/MoS₂ photocathode without the CdS layer was investigated and shown to maintain its initial activity over 50 hrs of continuously illuminated PEC testing (Figure 49.b).

b. MoS₂/TiO₂ coating strategy

Although the MoS₂ via MoO_x ALD approach showed promise as a durable catalytic coating for the PEC hydrogen evolution reaction, this plasma-induced surface reaction appeared to have deleterious effects on the underlying semiconducting layers. With this complication in mind, we

moved to a surface coating strategy that involved first depositing a thin TiO₂ coating via thermal ALD followed by the plasma-enhanced MoO_x ALD treatment and then sulfidation in the aforementioned H₂S/H₂ environment. This treatment led to dramatically enhanced durability of a CGSe photocathode sample, with one sample remaining active for nearly 350 hrs of continuously-illuminated operation (Figure 50.a). The delayed degradation of this MoS₂/TiO₂-treated device compared to a bare CGSe photocathode was shown by inductively couple plasma-mass spectrometry (ICP-MS) investigations (Figure 50.b). These experiments showed that all of the copper dissolved from a bare CGSe sample in 50 hrs of continuously-illuminated PEC operation, whereas this complete dissolution did not take place until about 350 hrs in the MoS₂/TiO₂-treated sample.

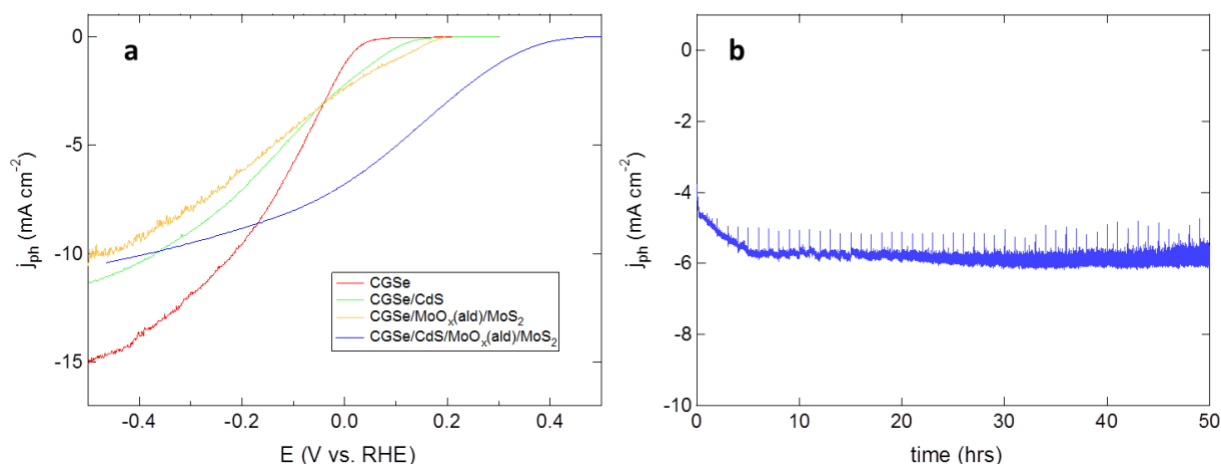


Figure 49. (a) Activity of CGSe electrodes incorporating the MoS₂ protection scheme. The MoS₂ was synthesized by sulfidation of atomic layer deposited MoO_x films in an H₂S atmosphere. CdS films were deposited by standard chemical bath deposition methods. (b) Stability of MoS₂/MoO_x/CGSe electrodes held at -0.2 V vs. RHE. The MoS₂ protection layer protects the CGSe electrode from corrosion for greater than 50 hrs.

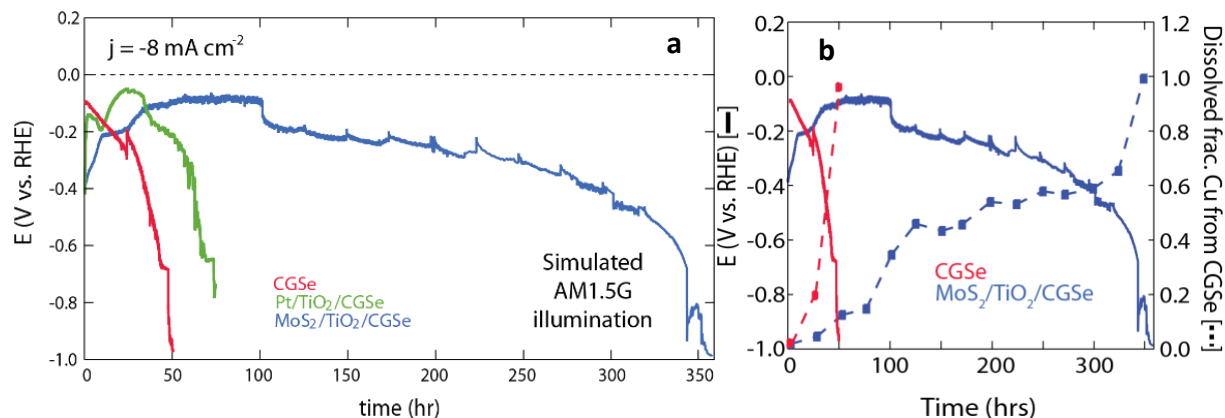


Figure 50. (a) Chronopotentiometry plot of CGSe electrodes with different catalytic and protecting schemes. This plot was generated by holding the electrodes at -8 mA cm⁻² continuously with one linear sweep voltammogram every 24 hours. (b) Chronopotentiometry plot of CGSe electrodes with and without catalytic and protecting schemes (from a). On the secondary ordinate, data from inductively-coupled plasma mass spectrometry (ICP-MS) are shown, demonstrating the fraction of Cu in the film that dissolved into the electrolyte, sampled at intervals by aliquotting.

This dual MoS₂/TiO₂ coating was then introduced into a CGSe photocathode device that had been coated with a CdS buffer layer, resulting in a highly active PEC photocathode with onset potential greater than +0.5 V vs. RHE (Figure 51.a).⁵³ The PEC performance of devices prepared in this manner degraded over the course of 24 hrs of continuously-illuminated testing, as evidenced by the time-lapsed linear sweep voltammograms of Figure 51.a and the chronoamperometric durability testing of Figure 51.b. The degradation of these devices was explored in-depth via x-ray spectroscopies conducted by the Heske group at UNLV and reported in our collective publication.⁵³

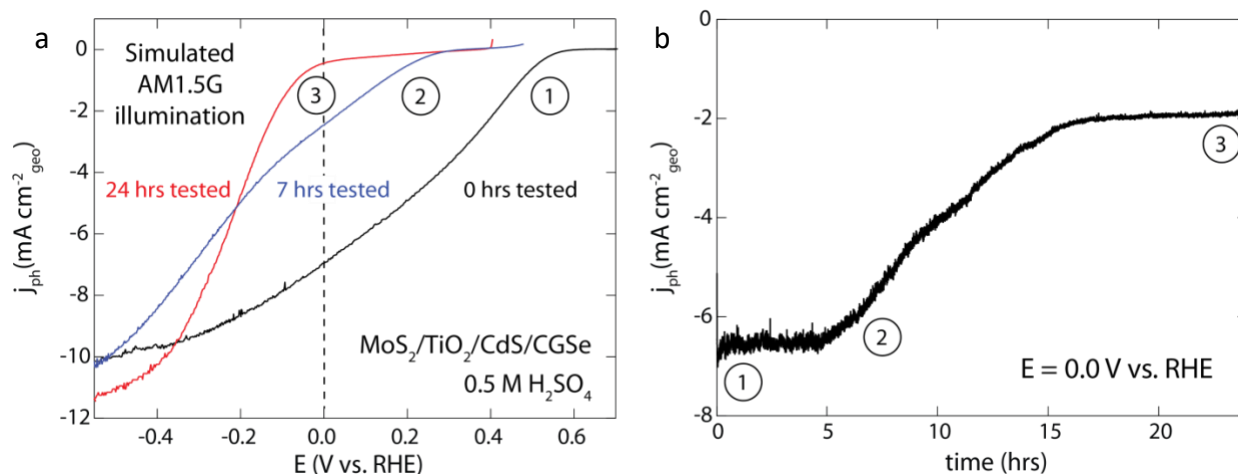


Figure 51. LSVs of MoS₂/TiO₂/CdS/CGSe electrode sibling samples after electrochemical chronoamperometry (0 V vs. RHE) tests lasting 0, 7, and 24 hrs. (b) 24 hr chronoamperometry (0 V vs. RHE) plot with marks to denote LSV time stamps.

c. TiO₂ durability investigation

The imperfect durability of the MoS₂/TiO₂ coated devices in Figure 51 induced us to investigate the mechanisms for the device degradation. As a start, we focused upon the intrinsic durability of the TiO₂ coating layer, since we hypothesized that this layer is less durable than the MoS₂ overcoating. By preparing simplified electrochemical devices composed of a degenerately doped (n⁺) silicon wafer piece as conductive substrate, a ~5 nm ALD TiO₂ protective coating, and a nanoparticulate (“1 nm” via electron beam evaporation) Pt catalytic layer, we aimed to investigate the durability of these TiO₂ coatings under electrochemical hydrogen evolution reaction (HER) conditions in acid. We found that these as-deposited coatings were highly unstable, requiring dramatically increased overpotentials for the HER after less than 10 hrs of continuous testing at -10 mA cm⁻² in acidic media (Figure 52.a, blue curve). We managed to improve the durability of these coatings by a rapid thermal annealing (RTA, <10 min at < 500°C) procedure in an oxygen-containing atmosphere prior to Pt deposition (Figure 52.a, black curve). However, this annealing procedure proved deleterious to a complete CGSe/TiO₂/Pt photocathode device, the PEC activity of which suffered dramatically (Figure 52.b).

In an effort to identify an annealing condition that would impart durability to the TiO₂ coating without compromising the CGSe photoactivity, we investigated the effect of temperature on the durability of the TiO₂-coated electrochemical HER devices. While all of the RTA-treated devices showed improved activity over the as-deposited TiO₂ coatings, it appeared that a 500°C treatment

imparted the greatest durability (Figure 53.a). As shown in the grazing-incidence x-ray diffractogram of Figure 53.b, such a treatment results in the crystallization of the TiO₂ from its as-deposited amorphous state to an anatase phase, perhaps leading to the enhancement in durability. Further investigations are underway in order to determine the minimally-invasive treatment that can enact such a phase transition while not deleteriously affecting the underlying CGSe absorber.

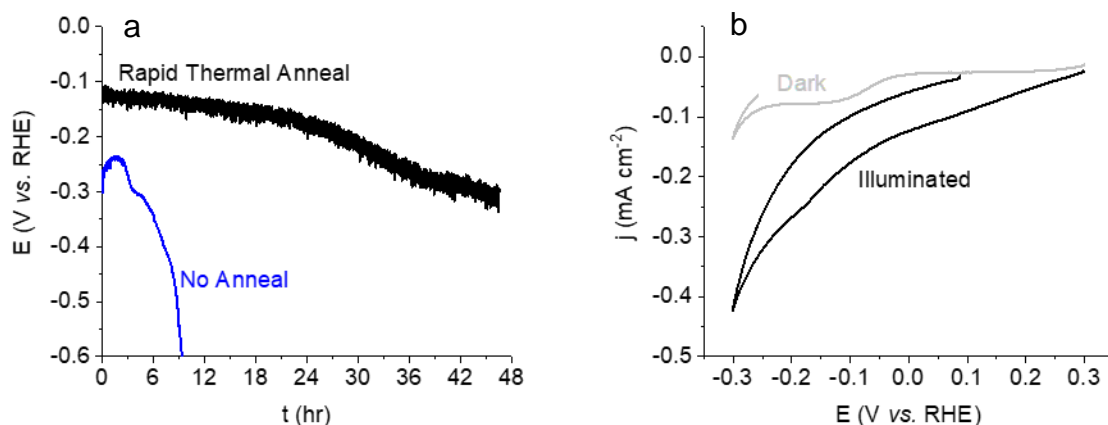


Figure 52. (a) CP of n-Si/TiO₂/Pt electrodes comparing the durability with and without an RTA procedure being employed, tested in 0.1 M HClO₄ electrolyte (b) LSV of an analogously-prepared CGSe|TiO₂|Pt device both under 1 Sun illumination and in the dark, tested in 0.5 M H₂SO₄ electrolyte; all experiments were performed with H₂ bubbling continuously, a Hg/HgSO₄ reference electrode, and an Ir/IrO_x counter electrode

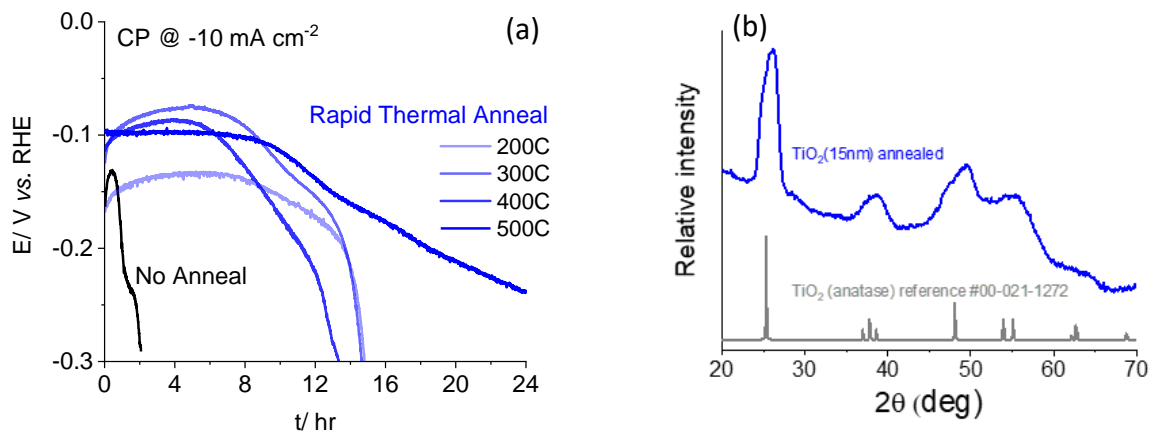


Figure 53. (a) CP of n-Si|TiO₂|Pt devices comparing the durability after treatment of an RTA procedure at different temperatures, tested in 0.5 M H₂SO₄ electrolyte; all experiments were performed with H₂ bubbling continuously, a Hg/HgSO₄ reference electrode, and an Ir/IrO_x counter electrode. (b) GI-XRD characterization of an RTA-treated TiO₂ coating showing the emergence of a crystalline anatase TiO₂ phase.

6. Technical achievements in Task 4 “Structure validation and benchmark efficiency measurement”

The purpose of this task was to determine the water splitting capabilities of chalcopyrite-based hybrid photoelectrodes. Despite our best efforts, we found that wide band gap chalcopyrite top cells in combination with narrow-band gap Cu(In,Ga)Se₂ solar cells ultimately did not provide enough voltage to spontaneously initiate water splitting. In light of this findings, we pursued alternate structures, such as replacing the bottom narrow band gap CIGSe device with a GaAs solar cell in the monolithic tandem PEC device.

a. Temperature resistant transparent conductive oxides as window layers

In preparation to fabricate monolithic tandem HPE devices with GaAs, efforts were first focused on the development of high temperature resistant transparent conductive oxide (TCO) films to be used as intermediate window layer between the top wide band gap chalcopyrite and the bottom GaAs solar cell. In this study, we first used p-n+ Si wafers provided by Stanford as a cheap alternative to GaAs in order to validate our processes. These wafers were used both to investigate the effects of high temperature cycles on TCOs and to validate the integration scheme of wide band gap chalcopyrites into monolithic tandem HPE devices.

Indium tin oxide (ITO) and indium molybdenum oxide⁵⁴ (IMO) thin-films have previously been investigated by our group for their potential as intermediate window layer materials for monolithic tandem devices. To further study these TCOs and their integration into devices, 500 nm of each TCO was RF-sputter deposited onto HF-etched Si p-n+ substrates. A portion of each TCO/Si sample was then annealed at 500 °C for 1 hour in vacuum in order to mimic the conditions of a thin CuGaSe₂ film deposition. The 1x1 inch Si p-n+ solar cells were then broken into pieces less than 0.5 cm² for more realistic charge collection distances, and to allow for a statistical sample distribution. The short-circuit current and Voc from J-V measurements of the ITO/Si p-n+ and IMO/Si p-n+ solar cells before and after annealing are plotted versus sample area in Figure 54. While these parameters are closely tied to the performance of the p-n+ junction and thus the Si absorber substrate, non-ideal TCO properties, such as reduced optical transmission or a non-ideal Si-TCO junction, would also cause these values to suffer. The ITO/Si cells show a Jsc of ~ 24.7 mA/cm², and even a slight increase in Jsc after annealing. The IMO/Si samples underperform in comparison, with a lower average Jsc of ~ 23.3 mA/cm². However, for both TCO materials little to no change in the average Jsc is seen after annealing. This is very promising, in that the annealing treatment is shown to not significantly reduce the current output, regardless of the TCO used. The Voc results presented at the bottom of Figure 54 show the as-deposited IMO/Si sample set to produce the highest average Voc, but the annealed IMO/Si sample to produce the lowest average Voc. Further, a reduced average Voc is seen for both annealed sample sets, regardless of the TCO used. Because the Voc is dependent on the saturation current in the cell, this suggests an increased recombination in the cells after annealing, which may or may not be dependent on the TCO used. Overall, the ITO/Si films show better performance both as-deposited and after annealing, compared to the IMO/Si films. The cause of the reduced Voc after annealing needs to be further understood, but both TCO materials and the Si wafers have shown to be able to withstand the deposition temperatures required for the wide band gap chalcopyrite absorber, and with little to no loss in Jsc. These results are promising enough to warrant further investigation of both TCO materials as window layers integrated in full tandem devices.

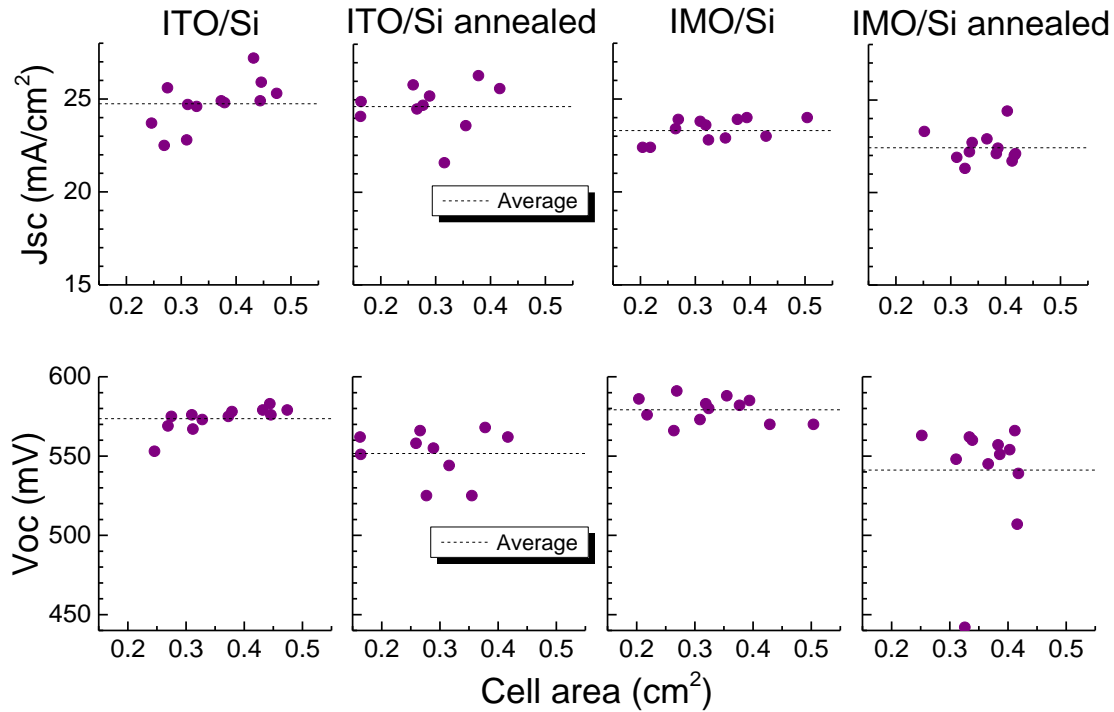


Figure 54. J_{sc} and V_{oc} values taken from J-V curves measured on each sample.

Based on these results, ITO was further used to integrate the wide band gap chalcopyrite CuGaSe_2 (CGSe) with a p-n+ Si wafer into our first monolithic tandem device structure. CGSe was co-evaporated by a three-stage process onto both ITO/Si and ITO/Mo substrates, to test the performance of both CGSe with an ITO back contact, and CGSe as a top-cell in a monolithic device. The J-V curve of the CGSe film deposited onto ITO/Mo is shown in Figure 55.a. The J_{sc} ($3.3 \text{ mA}/\text{cm}^2$), Fill Factor (FF, 32%), and open-circuit voltage (V_{oc} , 745 mV) obtained are similar to a comparably grown CGSe film on $\text{SnO}_2:\text{F}$ (FTO, dashed black line). These results show ITO to act as a sufficient transparent back contact for CGSe, on-par with industrial FTO substrates. A J-V curve of an ITO/Si bottom cell from our previous TCO testing after the 500°C 1 hour annealing (Figure 54) is shown in Figure 55.b, for reference. A J_{sc} of $24 \text{ mA}/\text{cm}^2$ is achieved, as well as a FF of almost 70% and V_{oc} of 562 mV.

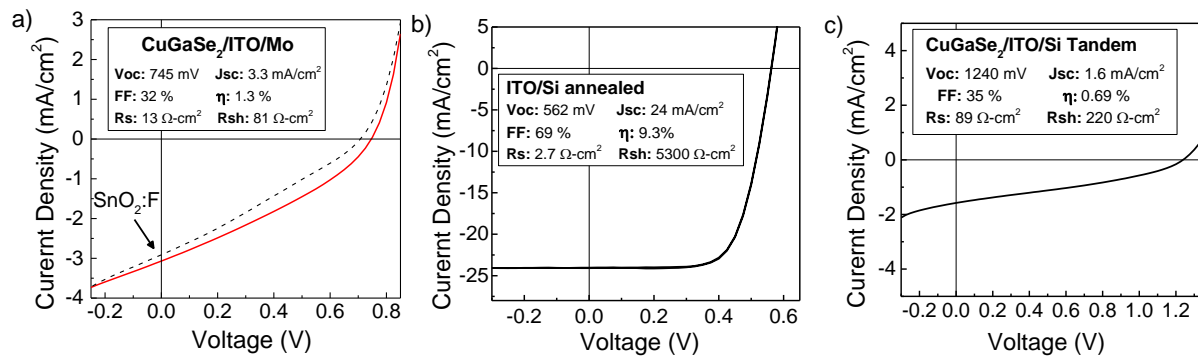


Figure 55. J-V curves of (a) CuGaSe_2 on ITO as bottom contact, (b) Si with ITO top contact after annealing, and (c) first $\text{CuGaSe}_2/\text{ITO}/\text{Si}$ monolithic tandem device demonstrating over 1.2 V V_{oc} .

In the final tandem device shown in Figure 55.c, the V_{oc} from the two cells is additive, producing a total V_{oc} of 1240 mV. While a V_{oc} over 1300 mV should be possible, variation in cell performance may be responsible for the slightly lower V_{oc} achieved for this sample. A lower than expected J_{sc} of 1.6 mA/cm² is achieved by the monolithic tandem device. We attribute this to current mis-match as described in the following. While the bottom Si cell outputs 24 mA/cm², after light filtering from the top absorber is taken into account this could easily drop below the 3.3 mA/cm² output by the top absorber, resulting in the Si bottom cell limiting the overall device current. This conclusion is further supported by the QE data shown in Figure 56, taken from an annealed ITO/Si cell with various CGSe filters placed over it. Here we see that even a 270 nm CGSe film reduces the current output from the Si cell below it by almost half, and a 500 nm thick film reduces the current output by almost half again, to ~6 mA/cm². Optimization of the CGSe thickness for these Si wafers (or other high-current density bottom cells) will need to be performed to ensure optimal current matching in the final tandem device.

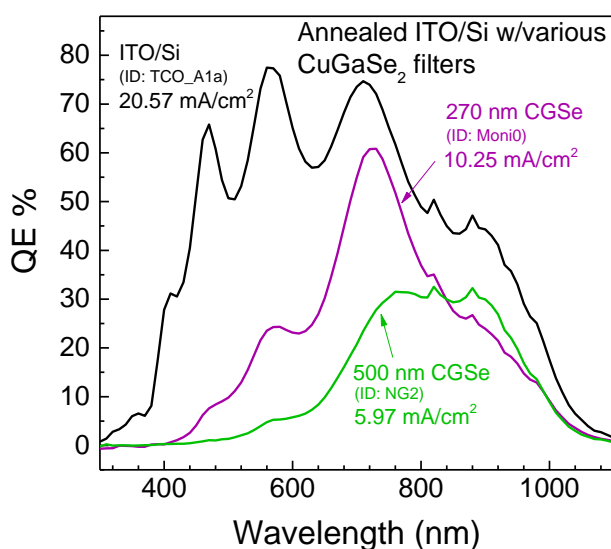


Figure 56. QE measurement of an annealed ITO/Si cell (black), and the same cell filtered by a 270 nm thick CGSe film (purple), and a 500 nm CGSe film (green).

b. CuGaSe₂/GaAs Tandem PEC cell

In a second phase, our group switched from p-n+ Si solar cells to single junction GaAs structures provided by SpectroLab several years prior the beginning of this program. Figure 57.a shows the current-voltage behavior of a GaAs solar cell measured in-lab exhibiting a V_{oc} of 970 mV. Given the E_{ONSET} of champion CGSe photocathodes from Figure 47 was 0.6 V vs RHE, using a GaAs solar cell as a PV driver was expected to provide close to 1.6 V vs RHE, theoretically sufficient to spontaneously split water. In order to determine if enough current could be generated by the coupling of the two sub-cells, quantum efficiency measurements were done on the GaAs cell shaded by several CGSe champion photocathodes (comprising Ru, In₂S₃ and CdS surface layers), seen in Figure 57.b. The GaAs cell generated 3.4 mA/cm² J_{sc} on average, enough current to yield up to 4.2% STH efficiency, assuming this current to be the lesser of the two cells.

The PEC current-voltage behavior of a CGSe champion top cell is shown in Figure 58.a along with its performance when stacked with a GaAs bottom cell. While coupling the CGSe cell with a GaAs solar cell did in fact shift the E_{ONSET} 800 mV anodically from 0.3 to 1.1 V vs RHE, the E_{ONSET} still fell short of the voltage deemed theoretically necessary to split water. A considerable amount of voltage was lost due to simple aging of the CGSe photocathodes. As seen in Figure 58.b, after only 5 days of the first measurement, the E_{ONSET} was reduced by 0.3 V and after 14 days by another 0.1V down to 0.2 V vs RHE. Based on these initial results, we decided not to proceed with the monolithic integration of chalcopyrites on GaAs until the origin of samples aging was better understood and addressed.

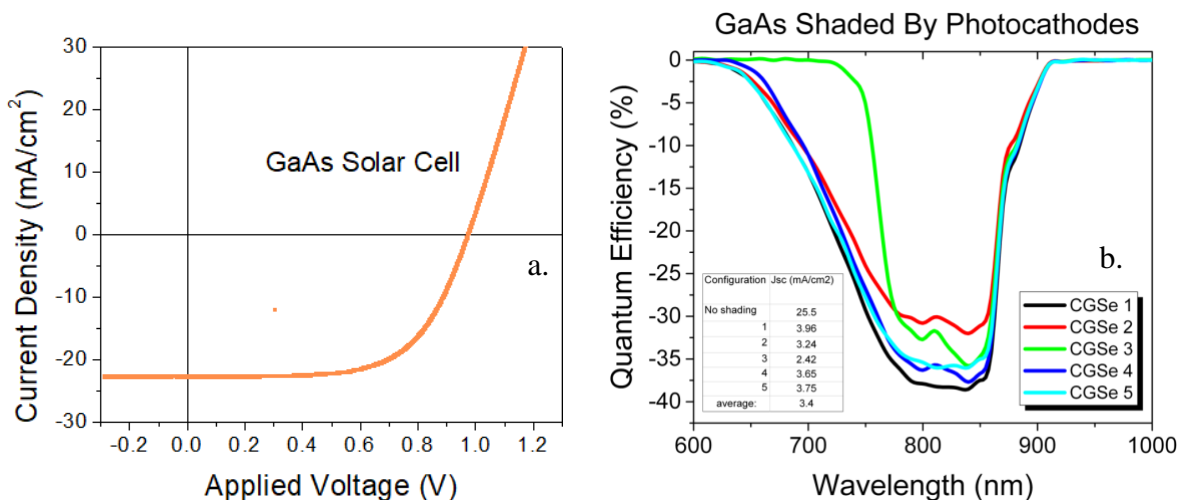


Figure 57. (a) Current-voltage behavior of a GaAs solar cell exhibiting an V_{oc} of 970 mV. (b) Quantum efficiency of the same GaAs solar cell shaded by several champion CGSe photocathodes exhibiting an average shaded J_{sc} of 3.4 mA/cm².

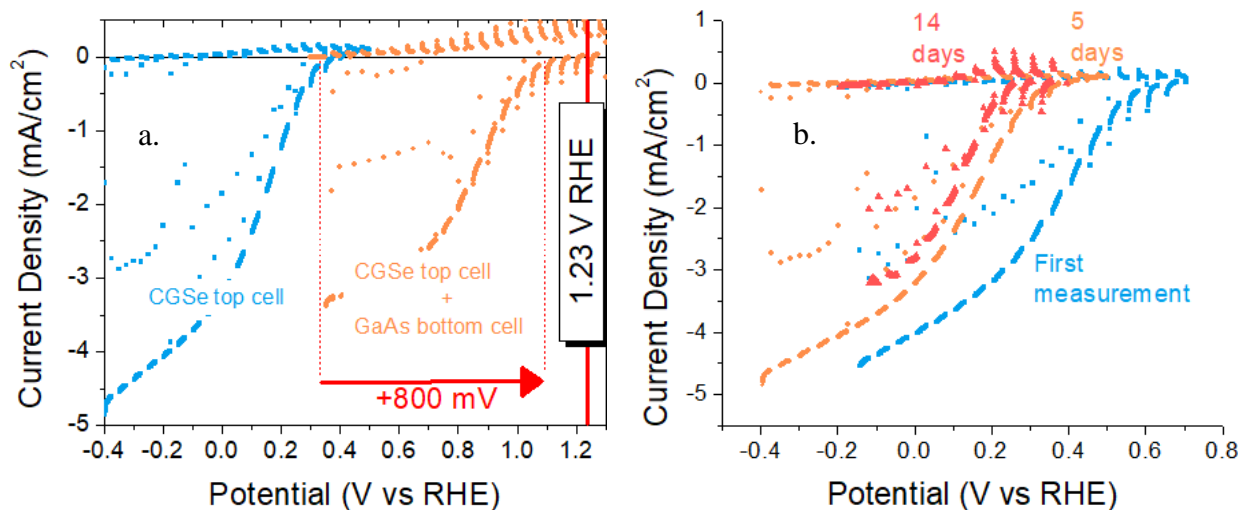


Figure 58. (a) Current-voltage behavior of a CGSe champion and its mechanical coupling with a GaAs solar cell. (b) LSV scans of a CGSe champion showing that mere aging contributed significantly with the voltage loss that prevented an E_{ONSET} high enough to split water.

7. Summary and outlook

During this multi-year research program, we have significantly advanced the knowledge in wide band gap copper chalcopyrites for PEC water splitting. By combining unique analytical techniques, state-of-the-art theoretical modeling with cutting-edge thin film materials synthesis, we permitted the development of promising materials candidates with tunable bulk and/or interface properties, including Cu(In,Ga)S_2 , CuGa(S,Se)_2 , CuGaSe_2 and CuGa_3Se_5 . New synthesis methods were also developed to facilitate the integration of these absorbers onto transparent conductive FTO substrates without deteriorating their optoelectronic properties, a critical step towards the realization of mechanically stacked or monolithically integrated tandem PEC devices. Through advanced X-ray photoelectron spectroscopy characterizations, we have also quantified the energetics of wide band gap chalcopyrites interfaced with conventional CdS buffer layer, revealing that such architecture would lead to undesirable interfacial electronic recombination due to large conduction band offsets. Alternate surface treatments techniques were developed to improve chalcopyrite energetics towards the hydrogen evolution reaction. By combining In_2S_3 , CdS and alkali treatments, onset potential as high as 600 mV vs. RHE were demonstrated with CuGa_3Se_5 absorbers integrated on FTO substrates (compared to 0 V vs RHE without treatment). Unique surface passivation methods were also developed to improve the durability of our chalcopyrite candidates. Using a combination of ultra-thin MoS_2 and TiO_2 films deposited by atomic layer deposition, we were able to increase the durability of CuGaSe_2 from less than 50 hours to over 350 hours. Finally, new techniques were investigated to integrate wide band gap chalcopyrites into tandem devices. We demonstrated that ITO and IMO transparent conductive oxide films could withstand the high temperatures required for top film deposition (typically 500°C) and be use as effective transparent window layers in monolithically integrated devices, as demonstrated with $\text{CuGaSe}_2/\text{c-Si p-n+}$ tandem solid-state structures. Best performing top cells were finally integrated using a mechanical stacking approach with GaAs bottom PV drivers. Unfortunately, aging significantly degraded the photocathodes performance, leading to tandem structures unable to drive the water splitting reaction without an external bias. As such, our end goal (3 L of H_2 in 8 hours) was not met on time. We have since identified important barriers which must be addressed in future studies to enable the realization of functional and durable chalcopyrite-based tandem PEC devices. Some of these key barriers are listed below.

ABSORBERS - Assessing the effect of copper on optical transmission: a key parameter to consider when selecting a wide band gap absorber for tandem applications is its sub-band gap optical transmission. The latter must be as high as possible in order to effectively power the bottom junction(s). However, we discovered that most synthesis techniques reported by the PV research community (i.e., CuInS_2 from sulfurization of Cu-rich metal alloys) lead to wide band gap chalcopyrites with extremely poor sub-band gap transmission, typically below 30% (e.g., CuGa(S,Se)_2 from CuGaSe_2 and Cu(In,Ga)S_2 from Cu/In/Ga metallic alloys). Ironically, growing these precursors copper-poor did not permit the incorporation of sulfur, as reported in Section 3.c for CuGa(S,Se)_2 . We eventually discovered a new approach to sulfurize a Cu-poor selenide precursor by deposited it a low temperature, yielding to wide band gap chalcopyrite 2.0 eV CuInGaS_2 with transmission over 70%. Nonetheless, the role of copper in sub-band gap transmission remains unknown to this date. We speculate “d-d excitations” at copper centers to be responsible for this phenomena, yet additional theoretical modeling and testing is required. Considering the potential of wide band gap chalcopyrites for both PEC and PV applications, we believe additional efforts should be engaged by the community to further study this issue.

INTERFACES - Improving energetics: our PEC studies have demonstrated over the years that bare chalcopyrites have poor energetics with respect to the water splitting redox potentials, with Fermi levels located usually only 100 meV below HER. As such, it is highly unlikely that efficient chalcopyrite-based PEC structures can be obtained without additional n-type buffer layers (buried junction scheme). Tests were performed so far with conventional sulfide buffer layers, including CdS and In₂S₃, and encouraging results were achieved. Nonetheless, these sulfide layers have intrinsic limitations when paired with wide band gap chalcopyrites, including relatively poor energetic alignment (as evidenced in Section 4.a) and band gaps too narrow for proper optical match with 1.8 eV absorbers. As such, we recommend the development of non-sulfide-based buffers with wider band gaps and, if possible, tunable energetics. Potential buffer candidates that meet these criteria include (Mg,Zn)O and Cu-free (In,Ga)Se₂.

DURABILITY – *In-situ* methods to understand photocorrosion mechanisms: the strategy used thus far by our group (and the PEC community in general) to address electrode durability is limited to the exploration of surface passivation strategies, where more durable materials are coated on top of less durable ones. Success is usually defined by the improvement of the operation time of the protected absorber when compared to the bare one. Although this approach can provide guidelines for the selection of surface passivators, it does not address the fundamental issue of semiconductor corrosion itself, and hence the mechanisms leading to PEC material deterioration during water splitting are, for the most part, unknown (or ignored). In the past, our team worked on uncovering these mechanisms by performing post-PEC testing spectroscopic studies, and observed for instance that Ga₂O₅ layers form at the surface of CuGaSe₂ photocathodes after a single linear sweep voltammetry, whereas SeO₂ native oxide layers observed prior to the testing procedures were removed during PEC testing. We stipulated at the time that CuGaSe₂ corrosion could originate from dissolution of Ga₂O₅, a material known to be highly unstable in acid. However, it is likely that the CuGaSe₂ surface chemistry was halted after PEC testing when the sample was removed from the test cell, further rinsed with DI water and dried with nitrogen, packed, and finally shipped from Hawaii to UNLV. To finally reveal the complex chemistry taking place at the surface of photocathodes during PEC water splitting, new *in-situ* and *in-operando* characterization techniques, such as X-ray-based spectroscopic techniques, must be further developed by the PEC community.

8. Acknowledgments

This material is based upon work supported by the U.S. Department of Energy's Office of Energy Efficiency and Renewable Energy (EERE) under the Fuel Cell Technologies Office (FCTO) under Award Number DE-EE0006670.

N. Gaillard would like to express his utmost gratitude to all faculty members, students, postdoctoral fellows and senior scientists involved in this multi-year program, including Drs. Marina Chong, Kimberly Horsley, Dixit Prasher, Wilman Septina and Mr. Alexander Deangelis at the University of Hawaii, Prof. Thomas Jaramillo, Drs. Thomas Hellstern and David Palm at Stanford, Prof. Clemens Heske, Drs. Monica Blum, Lothar Weinhardt and James Carter at the University of Nevada, Las Vegas, Drs. Tadashi Ogitsu and Joel Varley at Lawrence Livermore National Laboratory and Drs. Kai Zhu, Christopher Muzzillo, Miguel Contreras, Heli Wang and Todd Deutsch at the National Renewable Energy Laboratory.

9. Disclaimer

This report was prepared as an account of work sponsored by an agency of the United States Government. Neither the United States Government nor any agency thereof, nor any of their employees, makes any warranty, express or implied, or assumes any legal liability or responsibility for the accuracy, completeness, or usefulness of any information, apparatus, product, or process disclosed, or represents that its use would not infringe privately owned rights. Reference herein to any specific commercial product, process, or service by trade name, trademark, manufacturer, or otherwise does not necessarily constitute or imply its endorsement, recommendation, or favoring by the United States Government or any agency thereof. The views and opinions of authors expressed herein do not necessarily state or reflect those of the United States Government or any agency thereof.

10. Products developed under the Award

a. Research papers (6)

N. Gaillard, D. Prasher, M. Chong, A. Deangelis, K. Horsley, H. A. Ishii, J. P. Bradley, J. Varley, and T. Ogitsu, Wide band gap Cu(In,Ga)S₂ Photocathodes Integrated on Transparent Conductive F:SnO₂ Substrates for Chalcopyrite-Based Water Splitting Tandem Devices, *ACS Appl. Energy Mater* **2** (8), 5515 (2019). <https://doi.org/10.1021/acsaem.9b00690>.

A. D. Deangelis, K. Horsley and N. Gaillard, Wide Band Gap CuGa(S,Se)₂ Thin Films on Transparent Conductive Fluorinated Tin Oxide Substrates as Photocathode Candidates for Tandem Water Splitting Devices, *The Journal of Physical Chemistry C* **122** (26), 14304 (2018). <https://doi.org/10.1021/acs.jpcc.8b02915>.

C. Muzzillo, W. Ellis Klein, Z. Li, A. Deangelis, K. Horsley, K. Zhu and N. Gaillard, Low-Cost, Efficient and Durable H₂ Production by Photoelectrochemical Water Splitting with CuGa₃Se₅ Photocathodes, *ACS Appl. Mater. Interfaces* **10** (23), 19573 (2018). <https://doi.org/10.1021/acsaami.8b01447>

Varley, J. B.; Lordi, V.; Ogitsu, T.; Deangelis, A.; Horsley, K.; Gaillard, N. Assessing the Role of Hydrogen in Fermi-Level Pinning in Chalcopyrite and Kesterite Solar Absorbers from First-Principles Calculations. *Journal of Applied Physics* **2018**, *123* (16), 161408. <https://doi.org/10.1063/1.5006272>. [Editor's Pick]

T.R. Hellstern, D.W. Palm, J. Carter, A.D. DeAngelis, K. Horsley, L. Weinhardt, W. Yang, M. Blum, N. Gaillard, C. Heske, and T.F. Jaramillo. Molybdenum disulfide catalytic coatings via atomic layer deposition for solar hydrogen production from copper gallium diselenide photocathodes. *ACS Applied Energy Materials* **2**, 1060-1066 (2019). <https://doi.org/10.1021/acsaem.8b01562>

A. D. DeAngelis, K. C. Kemp, N. Gaillard and K. S. Kim, Antimony(III) Sulfide Thin Films as a Photoanode Material in Photocatalytic Water Splitting, *ACS Appl. Mater. Interfaces* **8** (13), 8445 (2016). [10.1021/acsaami.5b12178](https://doi.org/10.1021/acsaami.5b12178)

b. Invited presentations (24)

N. Gaillard, Wide Band gap Chalcopyrite-based Photoelectrodes for Renewable Hydrogen Production, The 2019 Spring Meeting of the European Materials Research Society (E-MRS), Symposium A "Latest Advances in Solar Fuels III", A.5.6, Nice (France), 2019.

N. Gaillard, A. D. DeAngelis and K. Horsley, Wide Band gap Copper Chalcopyrite Candidates for Renewable Hydrogen Generation, the 233rd Electrochemical Society Meeting, Symposium I05, 1884, Seattle (WA), 2018.

N. Gaillard, A. D. DeAngelis and K. Horsley, Novel Chalcopyrite Materials for Economical Photoelectrochemical Hydrogen Production the 231st Electrochemical Society Meeting, Symposium I03, 1532, New Orleans (LA), 2017.

N. Gaillard, A. D. DeAngelis and K. Horsley, Development of Wide Band gap Copper Chalcopyrite Materials for Economical Photoelectrochemical Hydrogen Production, the 230th Electrochemical Society Meeting, Symposium L04, 3630, Honolulu (HI), 2016.

N. Gaillard, A. DeAngelis, M. Chong and D. Prasher, Wide Band gap Copper Indium Gallium Disulfide Thin Film Materials for Photoelectrochemical Hydrogen Production, the 228th Electrochemical Society Meeting, Symposium L06, 1702, Phoenix (AZ), 2015.

T. Ogitsu, J. Varley, A. Deangelis, K. Horsley and N. Gaillard, Integrating Ab-Initio Simulations and Experimental Characterization Methods: Towards Accelerated Chalcopyrite Materials Development for Hydrogen Production, the 233rd Electrochemical Society Meeting, Symposium I05, 1855, Seattle (WA), 2018.

T. Ogitsu, J. Varley, F. Zhou, V. Lordi and N. Gaillard, Computational Design of Chalcopyrite Photoabsorbers for Photoelectrochemical H₂ Production, the 230th Electrochemical Society Meeting, Symposium L04, 3635, Honolulu (HI), 2016.

T. Ogitsu, J. Varley, N. Gaillard, C. Heske and M. Blum, First-Principle Simulations in Chalcopyrite Based Photoelectrode Development, the 231st Electrochemical Society Meeting, Symposium I03, 1529, New Orleans (LA), 2017.

J. Varley, Elucidating the Role of Point Defects in the Performance of Thin-Film Solar Cells Through First-Principles Calculations, Gordon Research Conference, Defects in Semiconductors (2018).

Jaramillo, T. F. (2016, March). Catalyst Development and Integration onto Semiconductors for Solar H₂ Production by Photoelectrochemical (PEC) Water-Splitting. Presented at the 2016 MRS Spring Meeting, Phoenix, AZ.

Jaramillo, T. F. (2016, October). Electrocatalyst Development for Solar Fuels: H₂ Evolution, O₂ Evolution, and CO₂ Reduction. Presented at PRiME 2016, Honolulu, HI.

Jaramillo, T. F. (2019, April). Development of Catalytic Coatings for H₂-Producing Photocathodes in Solar Water-Splitting. Presented at the 2019 MRS Spring Meeting, Phoenix, AZ.

C. Heske, “Using soft x-rays to look into (buried) interfaces of energy conversion devices”, Chemical and Materials Engineering, University of Nevada, Reno, Mar. 7, 2015.

C. Heske, “Helping to optimize Solar Energy-Conversion Devices with Soft X-Ray and Electron Spectroscopies”, American Ceramic Society Glass and Optical Materials Division, joint conference with the Deutsche Glastechnische Gesellschaft (ACerS GOMD-DGG meeting), Miami, FL, May 17-21, 2015.

C. Heske, “Using Soft X-Rays and Electrons to Determine the Chemical and Electronic Structure of Semiconductors for Solar Water Splitting”, Symposium “L10: Photocatalysts, Photoelectrochemical Cells and Solar Fuels”, 227th ECS Meeting, Chicago, IL, May 24-28, 2015.

C. Heske, “Using soft x-rays to look into (buried) interfaces of energy conversion devices”, XIV SBPMA Conference, Brazilian Materials Research Society (B-MRS), Rio de Janeiro, Sept. 28, 2015.

C. Heske, “Soft x-ray spectroscopy to study liquids, solids, gases, and their interfaces”, Advanced Light Source Users’ Meeting, Berkeley, Oct. 6, 2015.

C. Heske, “Chalcopyrites and III-V semiconductors for solar water splitting – a detailed look at the electronic and chemical surface structure”, Symposium “L07: Photocatalysts, Photoelectrochemical Cells and Solar Fuels”, 228th ECS Meeting, San Diego, CA, June 2, 2016.

C. Heske, “Helping to optimize Solar Energy-Conversion Devices with Soft X-Ray and Electron Spectroscopies”, “The Future of X-Ray and Electron Spectroscopies” Conference, Uppsala University, Sweden, June 17, 2016.

T. Ogitsu*, J. Varley, N. Gaillard, C. Heske, and M. Blum, “First-Principle Simulations in Chalcopyrite Based Photoelectrode Development”, 231st ECS Meeting, New Orleans, May 28 – June 2, 2017.

C. Heske, “Chemical and Electronic Surface Structure of Compound Semiconductors for Solar Water Splitting”, Symposium “L02: Photocatalysts, Photoelectrochemical Cells and Solar Fuels 8”, 232nd ECS Meeting, Washington, DC/National Harbor, MD, October 3, 2017.

C. Heske, “From applied to fundamental, from high throughput to *operando*: soft x-ray spectroscopy of systems for energy conversion”, ALS Energy Materials and Catalysis Review and Workshop, Berkeley, Jan. 17-18, 2018.

C. Heske, “Soft X-ray Spectroscopy of Materials and Interfaces for Solar Energy Conversion”, Boston College, Mar. 8, 2018.

C. Heske, “Chemical and Electronic Surface Structure of Chalcopyrites and other Compound Semiconductors for Solar Water Splitting”, Symposium on Latest Advances in Solar Fuels, 2019 E-MRS, Nice, France, May 27-31, 2019.

c. Contributed presentations (9)

K. Horlsey, A. Deangelis and N. Gaillard, Cu(In,Ga)S₂ Photocathodes with Optical Band gap Over 1.7 eV for Photoelectrochemical Water Splitting, the Materials Research Society Spring Meeting, Symposium EN18, EN18.15.05, Phoenix (AZ), 2018.

A. Deangelis, K. Horlsey and N. Gaillard, Wide band gap CuGa(S,Se)₂ As Top Cell Photocathodes for Tandem Water Splitting Devices, the 233rd Electrochemical Society Meeting, Symposium I05, 1929, Seattle (WA), 2018.

N. Gaillard, K. Horlsey and A. Deangelis, Photoelectrochemical and Solid-State Properties of Wide Band gap Copper Chalcopyrites for Renewable Hydrogen Generation, the Materials Research Society Spring Meeting, Symposium ES7, ES7.16.02, Phoenix (AZ), 2017.

A. D. DeAngelis, K. Horsley and N. Gaillard, Solid-State Characterization of Wide band gap CuGa(S,Se)₂ for PEC Water Splitting, the 230th Electrochemical Society Meeting, Symposium L04, 3714, Honolulu (HI), 2016.

A. D. DeAngelis, and N. Gaillard, Wide band gap Tuneable CuGaSSe Photocathodes for PEC Water Splitting, the Materials Research Society Spring Meeting, Symposium EE2, EE2.4.02, Phoenix (AZ), 2016.

N. Gaillard, A. D. DeAngelis, M. Chong and A. Zeng, Development of Wide Band gap Copper Chalcopyrite Thin Film Materials for Photoelectrochemical Hydrogen Production, the Materials Research Society Spring Meeting, Symposium J, J2.04, San Francisco (CA), 2015.

J. B. Varley, F. Zhou, V. Lordi, T. Ogitsu, and N. Gaillard, Identifying Optimal Chalcopyrite Alloys for Photoelectrochemical Hydrogen Production through First-Principles, the Materials Research Society Spring Meeting, Symposium EE2, EE2.4.01, Phoenix (AZ), 2016.

J. Carter*, B. Elizan, M. Blum, K. Horsley, A. DeAngelis, W. Yang, L. Weinhardt, N. Gaillard, and C. Heske, "Soft X-ray Spectroscopic Investigation of the CdS/Cu(In,Ga)S₂ Interface in Thin Films for Photoelectrochemical Water Splitting", MRS Spring Meeting 2017, Phoenix, AZ, April 17-21, 2017.

Hellstern, T. R., DeAngelis, A. D., King, L. A., Chakthranont, P., Britto, R. J., Gaillard, N., and Jaramillo, T.F. (2016, October). Non-Precious Metal-Catalyzed Photoelectrodes for Hydrogen Production Via Solar Water Splitting. Presented at PRiME 2016, Honolulu, HI.

d. Poster presentations (8)

A. Deangelis, K. Horlsey and N. Gaillard, Wide band gap CuGa(S,Se)₂ As Top Cell Photocathodes for Tandem Water Splitting Devices, the Materials Research Society Spring Meeting, Symposium EN19, EN19.04.34, Phoenix (AZ), 2018.

K. Horsley, A. DeAngelis, T. Hellstern, T. Jaramillo and N. Gaillard, Monolithic Tandem Devices using Wide band gap Chalcopyrite Absorbers for Photoelectrochemical Water Splitting, the Materials Research Society Spring Meeting, Symposium ES14.9.32, Phoenix (AZ), 2017.

J. Carter*, M. Blum, K. Horsley, A. DeAngelis, W. Yang, D. Hauschild, L. Weinhardt, N. Gaillard, and C. Heske, "Soft X-ray Spectroscopy of the CdS/Cu(In,Ga)S₂ Interface for Photoelectrochemical Water Splitting", Gerischer Electrochemistry Today Symposium, Boulder, CO, August 15, 2018.

J. Carter*, M. Blum, K. Horsley, A. DeAngelis, W. Yang, D. Hauschild, L. Weinhardt, N. Gaillard, and C. Heske, "Soft X-ray Spectroscopy of the CdS/Cu(In,Ga)S₂ Interface for Photoelectrochemical Water Splitting", Annual Undergraduate/Graduate Student Poster Competition Exposition, Southern Nevada Section of the American Chemical Society, November 17, 2018 (poster, 2nd place).

Palm, D. W., Hellstern, T. R., Gaillard, N., and Jaramillo, T. F. (2016, November). Engineering Interfaces for the Activation and Stabilization of Photovoltaic-Grade Thin Film Light Absorbers for Photoelectrochemical Hydrogen Production. Poster presented at 2016 AIChE Annual Meeting, San Francisco, CA.

Palm, D. W., Hellstern, T. R., DeAngelis, A. D., Gaillard, N., and Jaramillo, T. F. (2017, April). Activation and stabilization of copper chalcopyrite light absorbers for photoelectrochemical hydrogen production. Poster presented at 2017 ACS National Meeting, San Francisco, CA.

Palm, D. W., Hellstern, T. R., DeAngelis, A. D., Gaillard, N., and Jaramillo, T. F. (2017, November). Engineering Interfaces for Enhanced Carrier Extraction, Stability, and Catalysis in Copper Chalcopyrite Photoelectrochemical Arrays. Poster presented at 2017 MRS Fall Meeting, Boston, MA.

Palm, D. W., Hellstern, T. R., Carter, J., DeAngelis, A. D., Horsley, K., Blum, M., Weinhardt, L., Yang, W., Gaillard, N., Heske, C., and Jaramillo, T. F. (2018, August). Atomic layer deposited coatings for durable (photo)electrochemical hydrogen evolution. Poster presented at Gerischer Electrochemistry Today 2018, Boulder, CO.

11. References cited

- 1 Fujishima, A.; Honda, K. Electrochemical Photolysis of Water at a Semiconductor Electrode. *Nature* **1972**, 238, 37–38.
- 2 E. Miller & R. Rocheleau, patent 6887728 issued on 05/03/05.
- 3 Rocheleau, R. E.; Miller, E. L.; Misra, A. High-Efficiency Photoelectrochemical Hydrogen Production Using Multijunction Amorphous Silicon Photoelectrodes. *Energy & Fuels* **1998**, 12, 3–10.
- 4 Reece, S. Y.; Hamel, J. A.; Sung, K.; Jarvi, T. D.; Esswein, A. J.; Pijpers, J. J. H.; Nocera, D. G. Wireless Solar Water Splitting Using Silicon-Based Semiconductors and Earth-Abundant Catalysts. *Science* **2011**, 334, 645–648.
- 5 N. Gaillard, Y. Chang ; J. Kaneshiro ; A. Deangelis ; E. L. Miller, Proc. SPIE 7770, 77700V (August 24, 2010).
- 6 Abdi, F. F.; Han, L.; Smets, A. H. M.; Zeman, M.; Dam, B.; van de Krol, R. Efficient Solar Water Splitting by Enhanced Charge Separation in a Bismuth Vanadate-Silicon Tandem Photoelectrode. *Nat. Commun.* **2013**, 4, 2195.
- 7 Young, J. L.; Steiner, M. A.; Döscher, H.; France, R. M.; Turner, J. A.; Deutsch, T. G. Direct Solar-to-Hydrogen Conversion via Inverted Metamorphic Multi-Junction Semiconductor Architectures. *Nat. Energy* **2017**, 2, 17028..
- 8 Jackson, P.; Würz, R.; Rau, U.; Mattheis, J.; Kurth, M.; Schlötzer, T.; Bilger, G.; Werner, J. H. High Quality Baseline for High Efficiency, Cu(In_{1-x}Ga_x)Se₂ Solar Cells. *Prog. Photovoltaics Res. Appl.* **2007**, 15, 507–519.
- 9 Gaillard, N.; Prasher, D.; Kaneshiro, J.; Mallory, S.; Chong, M. Development of Chalcogenide Thin Film Materials for Photoelectrochemical Hydrogen Production. *Mater. Res. Soc. Symp. Proc.* **2013**, 1558, mrss13-1558-z02-07.
- 10 Jacobsson, T. J.; Fjällström, V.; Sahlberg, M.; Edoff, M.; Edvinsson, T. A Monolithic Device for Solar Water Splitting Based on Series Interconnected Thin Film Absorbers Reaching over 10% Solar-to-Hydrogen Efficiency. *Energy Environ. Sci.* **2013**, 6, 3676.
- 11 Seitz, L. C.; Chen, Z.; Forman, A. J.; Pinaud, B. A.; Benck, J. D.; Jaramillo, T. F. Modeling Practical Performance Limits of Photoelectrochemical Water Splitting Based on the Current State of Materials Research. *ChemSusChem* **2014**, 7, 1372–1385.
- 12 B. D. James, G. N. Baum, J. Perez and K. N. Baum, US DoE contract no. GS-10F-009J.
- 13 Heyd, J.; Scuseria, G. E.; Ernzerhof, M. Hybrid Functionals Based on a Screened Coulomb Potential. *J. Chem. Phys.* **2003**, 118 (18), 8207 - Blöchl, P. E. Projector Augmented-Wave Method. *Phys. Rev. B* **1994**, 50 (24), 17953–17979 - Kresse, G.; Furthmüller, J. Efficiency of Ab-Initio Total Energy Calculations for Metals and Semiconductors Using a Plane-Wave Basis Set. *Comp. Mater. Sci.* **1996**, 6 (1), 15–50.
- 14 Kajiki, T.; Hayashi, Y.; Takizawa, H. High-Pressure Synthesis of a New Copper Thioborate, CuBS₂. *Materials Letters* **2007**, 61 (11), 2382–2384 - Chen, L.-J.; Liao, J.-D.; Chuang, Y.-J. Self-Assembled Chalcopyrite Ternary Semiconductor CuBSe₂ Nanocrystals : Solvothermal Synthesis and Characterisation. *CrystEngComm* **2011**, 13 (8), 2909–2914
- 15 Pohl, J.; Albe, K. Intrinsic Point Defects in CuInSe₂ and CuGaSe₂ as Seen via Screened-Exchange Hybrid Density Functional Theory. *Phys. Rev. B* **2013**, 87 (24), 245203 - Huang, B.; Chen, S.; Deng, H.-X.; Wang, L.-W.; Contreras, M. A.; Noufi, R. N.; Wei, S.-H. Origin of

- Reduced Efficiency in Cu(In,Ga)Se₂ Solar Cells With High Ga Concentration: Alloy Solubility Versus Intrinsic Defects. *IEEE J. Photovoltaics* **2014**, 4 (1), 477–482.
- 16 Lehmann, S. *et al.* CuGaSe₂–CuGa₃Se₅ phase transition in CCSVT-grown thin films. *Thin Solid Films* **511**, 623–627, doi:10.1016/j.tsf.2005.11.067 (2006); Rusu, M. *et al.* CuGa_xSe_y chalcopyrite-related thin films grown by chemical close-spaced vapor transport (CCSVT) for photovoltaic application: Surface- and bulk material properties, oxidation and surface Ge-doping. *Sol. Energy Mater. Sol. Cells* **95**, 1555–1580, doi:10.1016/j.solmat.2011.01.016 (2011).
- 17 Kim, J., Minegishi, T., Kobota, J. & Domen, K. Investigation of Cu-deficient copper gallium selenide thin film as a photocathode for photoelectrochemical water splitting. *Jpn. J. Appl. Phys.* **51**, 015802–015806, doi:10.1143/JJAP.51.015802 (2012); Kumagai, H., Minegishi, T., Moriya, Y., Kubota, J. & Domen, K. Photoelectrochemical hydrogen evolution from water using copper gallium selenide electrodes prepared by a particle transfer method. *J. Phys. Chem. C* **118**, 16386–16392, doi:10.1021/jp409921f (2014).
- 18 Jaffe, J. E. & Zunger, A. Anion displacements and the band gap anomaly in ternary ABC₂ chalcopyrite semiconductors. *Phys. Rev. B* **27**, 5176–5179, doi:10.1103/PhysRevB.27.5176 (1983).
- 19 Alonso, M. I., Wakita, K., Pascual, J., Garriga, M. & Yamamoto, N. Optical functions and electronic structure of CuInSe₂, CuGaSe₂, CuInS₂, and CuGaS₂. *Phys. Rev. B* **63**, 075203–075213, doi:10.1103/PhysRevB.63.075203 (2001); Negami, T., Kohara, N., Nishitani, M., Wada, T. & Hirao, T. Preparation and characterization of Cu(In_{1–x}Ga_x)₃Se₅ thin films. *Appl. Phys. Lett.* **67**, 825–827, doi:10.1063/1.115456 (1995).
- 20 Metzger, W. K. *et al.* Recombination kinetics and stability in polycrystalline Cu(In,Ga)Se₂ solar cells. *Thin Solid Films* **517**, 2360–2364, doi:10.1016/j.tsf.2008.11.050 (2009).
- 21 Valderrama, R. C., Sebastián, P. J., Miranda-Hernandez, M., Enriquez, J. P. & Gamboa, S. A. Studies on the electrochemical stability of CIGS in H₂SO₄. *J. Photochem. Photobiol., A* **168**, 75–80, doi:10.1016/j.jphotochem.2004.04.006 (2004).
- 22 Bae, D., Seger, B., Vesborg, P. C. K., Hansen, O. & Chorkendorff, I. Strategies for stable water splitting via protected photoelectrodes. *Chem. Soc. Rev.* **46**, 1933–1954, doi:10.1039/C6CS00918B (2017).
- 23 Zhang, L. *et al.* Durable hydrogen evolution from water driven by sunlight using (Ag,Cu)GaSe₂ photocathodes modified with CdS and CuGa₃Se₅. *Chem. Sci.* **6**, 894–901, doi:10.1039/C4SC02346C (2015).
- 24 Kumagai, H. *et al.* Efficient solar hydrogen production from neutral electrolytes using surface-modified Cu(In,Ga)Se₂ photocathodes. *J. Mater. Chem. A* **3**, 8300–8307, doi:10.1039/C5TA01058F (2015).
- 25 Rau, U. *et al.* Oxygenation and air-annealing effects on the electronic properties of Cu(In,Ga)Se₂ films and devices. *J. Appl. Phys.* **86**, 497–505, doi:doi:http://dx.doi.org/10.1063/1.370758 (1999).
- 26 Mazzer, M. *et al.* Bifacial CIGS solar cells grown by low temperature pulsed electron deposition. *Sol. Energy Mater. Sol. Cells* **166**, 247–253, doi:10.1016/j.solmat.2016.10.048 (2017).
- 27 S. Chichibu *et al.*, “Band gap energies of bulk, thin-film, and epitaxial layers of CuInSe₂ and CuGaSe₂,” *J. Appl. Phys.*, vol. 83, no. 7, p. 3678, 1998; V. V. Kindyak, A. S. Kindyak, V. F. Gremenok, I. V. Bodnar, Y. V. Rud’, and G. A. Medvedkin, “Optical properties of laser-evaporated CuGaSe₂ films near and above the fundamental absorption edge,” *Thin Solid Films*, vol. 250, no. 1–2, pp. 33–36, 1994,

- 28 S. Chichibu and S. Shirakata, "Photoluminescence of CuGaS₂ epitaxial layers grown by metalorganic vapor phase epitaxy," *J. Appl. Phys.*, vol. 87, no. 8, pp. 3793–3799, 2000; J. Eberhardt *et al.*, "Optical properties of epitaxial CuGaS₂ layers on Si(111)," *J. Phys. Chem. Solids*, vol. 64, no. 9–10, pp. 1781–1785, 2003.
- 29 M. Bär *et al.*, "Determination of the band gap depth profile of the pentenary Cu(In_{1-x}Ga_x)(SySe_{1-y})₂ chalcopyrite from its composition gradient," *J. Appl. Phys.*, vol. 96, no. 7, pp. 3857–3860, 2004; M. Engelmann, B. E. McCandless, and R. W. Birkmire, "Formation and analysis of graded CuIn(S_{1-y}Sy)₂ films," *Thin Solid Films*, vol. 387, no. 1–2, pp. 14–17, 2001.
- 30 C. P. Liu and B. H. Tseng, "Preparation and characterization of CuInS₂ thin films completely converted from CuInSe₂ by sulfurization," *Thin Solid Films*, vol. 480–481, pp. 50–54, 2005; J. Titus, H.-W. Schock, R. W. Birkmire, W. N. Shafarman, and U. P. Singh, "Post-Deposition Sulfur Incorporation into CuInSe₂ Thin Films," *MRS Proc.*, vol. 668, 2001; T. Nakada, H. Ohbo, T. Watanabe, H. Nakazawa, M. Matsui, and A. Kunioka, "Improved Cu(In,Ga)(S,Se)₂ thin film solar cells by surface sulfurization," *Sol. Energy Mater. Sol. Cells*, vol. 49, no. 1–4, pp. 285–290, 1997; U. P. Singh, W. N. Shafarman, and R. W. Birkmire, "Surface sulfurization studies of Cu(InGa)Se₂ thin film," *Sol. Energy Mater. Sol. Cells*, vol. 90, no. 5, pp. 623–630, 2006; B. M. Basol *et al.*, "Studies on sulfur diffusion into Cu(In,Ga)Se₂ thin films," *Prog. Photovoltaics*, vol. 8, no. 2, pp. 227–235, 2000; V. Alberts, "Band gap engineering in polycrystalline Cu(In,Ga)(Se,S)₂ chalcopyrite thin films," *Mater. Sci. Eng. B Solid-State Mater. Adv. Technol.*, vol. 107, no. 2, pp. 139–147, 2004.
- 31 H. K. Park, J. Jo, H. K. Hong, G. Y. Song, and J. Heo, "Structural, optical, and electrical properties of tin sulfide thin films grown with electron-beam evaporation," *Curr. Appl. Phys.*, vol. 15, no. 9, pp. 964–969, 2015; Y. Kawano, J. Chantana, and T. Minemoto, "Impact of growth temperature on the properties of SnS film prepared by thermal evaporation and its photovoltaic performance," *Curr. Appl. Phys.*, vol. 15, no. 8, pp. 897–901, 2015; N. K. Reddy and K. T. R. Reddy, "Electrical properties of spray pyrolytic tin sulfide films," *Solid. State. Electron.*, vol. 49, no. 6, pp. 902–906, 2005; M. Calixto-Rodriguez, H. Martinez, A. Sanchez-Juarez, J. Campos-Alvarez, A. Tiburcio-Silver, and M. E. Calixto, "Structural, optical, and electrical properties of tin sulfide thin films grown by spray pyrolysis," *Thin Solid Films*, vol. 517, no. 7, pp. 2497–2499, 2009; J. Sun *et al.*, "Improved mobility of sol-gel method processed transparent tin sulfide thin films," *Mater. Lett.*, vol. 178, pp. 231–234, 2016.
- 32 J. Kessler, D. Lincot, J. Vedel, B. Dimmler, and H. W. Schock, "Photoelectrochemical studies of copper gallium diselenide films," *Sol. Cells*, vol. 29, no. 4, pp. 267–281, 1990.
- 33 J. Kim, T. Minegishi, J. Kobota, and K. Domen, "Investigation of Cu-deficient copper gallium selenide thin film as a photocathode for photoelectrochemical water splitting," *Jpn. J. Appl. Phys.*, vol. 51, no. 1, pp. 1–6, 2012.
- 34 E. Chen, Zhebo, Dinh, Huyen, Miller, *Photoelectrochemical Water Splitting Standards, Experimental Methods, and Protocols*. Springer-Verlag New York, 2013.
- 35 J. H. Schon *et al.*, "n-type conduction in Ge-doped CuGaSe₂," *Appl. Phys. Lett.*, vol. 75, no. 19, pp. 2969–2971, 1999; S. Schuler *et al.*, "Self-compensation of intrinsic defects in the ternary semiconductor CuGaSe₂," *Phys. Rev. B*, vol. 69, no. 4, p. 045210, 2004; X. Hu, J. Xue, J. Tian, G. Weng, and S. Chen, "Effect of Cu/Ga ratio on deep-level defects in CuGaSe₂ thin films studied by photocapacitance measurements with two-wavelength excitation," *Appl. Opt.*, vol. 56, no. 14, pp. 4090–4094, 2017.
- 36 H. Gerischer, "The impact of semiconductors on the concepts of electrochemistry,"

- Electrochim. Acta*, vol. 35, no. 11–12, pp. 1677–1699, Nov. 1990; R. Memming, *Semiconductor Electrochemistry*, 1st ed. WILEY-VCH Verlag, 2001.
- 37 K. Ueda, T. Maeda, and T. Wada, “Crystallographic and optical properties of CuGa₃S₅, CuGa₃Se₅ and CuIn₃(S,Se)₅ and CuGa₃(S,Se)₅ systems,” *Thin Solid Films*, vol. 633, pp. 23–30, 2017.
- 38 F. Babbe, L. Choubrac, and S. Siebentritt, “Quasi Fermi level splitting of Cu-rich and Cu-poor Cu(In,Ga)Se₂ absorber layers,” *Appl. Phys. Lett.*, vol. 109, no. 8, p. 082105, 2016.
- 39 A. Meeder *et al.*, “Photoluminescence and sub band gap absorption of CuGaSe₂ thin films,” *Thin Solid Films*, vol. 403–404, pp. 495–499, 2002.
- 40 C. Spindler, D. Regesch, and S. Siebentritt, “Revisiting radiative deep-level transitions in CuGaSe₂ by photoluminescence,” *Appl. Phys. Lett.*, vol. 109, no. 3, p. 032105, 2016.
- 41 A. Krysztopa, M. Igalson, J. K. Larsen, Y. Aida, L. Gütay, and S. Siebentritt, “Photoinduced current transient spectroscopy of defect levels in CuInSe₂ and CuGaSe₂ epitaxial and polycrystalline layers,” *J. Phys. D: Appl. Phys.*, vol. 45, no. 33, p. 335101, 2012; A. Krysztopa, M. Igalson, Y. Aida, J. K. Larsen, L. Gütay, and S. Siebentritt, “Defect levels in the epitaxial and polycrystalline CuGaSe₂ by photocurrent and capacitance methods,” *J. Appl. Phys.*, vol. 110, no. 10, p. 103711, 2011.
- 42 Marsen, B.; Wilhelm, H.; Steinkopf, L.; Klemz, S.; Unold, T.; Scheer, R.; Schock, H. W. Effect of Copper-Deficiency on Multi-Stage Co-Evaporated Cu(In,Ga)S₂ Absorber Layers and Solar Cells. *Thin Solid Films* **2011**, 519, 7224–7227.
- 43 Merdes, S.; Mainz, R.; Klaer, J.; Meeder, a.; Rodriguez-Alvarez, H.; Schock, H. W.; Lux-Steiner, M. C.; Klenk, R. 12.6% Efficient CdS/Cu(In,Ga)S₂-Based Solar Cell with an Open-circuit Voltage of 879mV Prepared by a Rapid Thermal Process. *Sol. Energy Mater. Sol. Cells* **2011**, 95, 864–869.
- 44 Shirakata, S.; Kannaka, Y.; Hasegawa, H.; Kariya, T.; Isomura, S. Properties of Cu(In,Ga)Se₂ Thin Films Prepared by Chemical Spray Pyrolysis. *Jpn. J. Appl. Phys.* **1999**, 38, 4997–5002.
- 45 Branch, M. S.; Berndt, P. R.; Botha, J. R.; Leitch, A. W. R.; Weber, J. Structure and Morphology of CuGaS₂ Thin Films. *Thin Solid Films* **2003**, 431–432, 94–98.
- 46 Rudigier, E.; Alvarez-Garcia, J.; Luck, I.; Klaer, J.; Scheer, R. Quality Assessment of Chalcopyrite Thin Films Using Raman Spectroscopy. *J. Phys. Chem. Solids* **2003**, 64, 1977–1981.
- 47 Nakada, T.; Ohbo, H.; Watanabe, T.; Nakazawa, H.; Matsui, M.; Kunioka, A. Improved Cu(In,Ga)(S,Se)₂ Thin Film Solar Cells by Surface Sulfurization. *Sol. Energy Mater. Sol. Cells* **1997**, 49, 285–290.
- 48 Varley, J. B.; Lordi, V.; Ogitsu, T.; Deangelis, A.; Horsley, K.; Gaillard, N. Assessing the Role of Hydrogen in Fermi-Level Pinning in Chalcopyrite and Kesterite Solar Absorbers from First-Principles Calculations. *J. Appl. Phys.* **2018**, 123, 161408.
- 49 Merdes, S.; Mainz, R.; Klaer, J.; Meeder, a.; Rodriguez-Alvarez, H.; Schock, H. W.; Lux-Steiner, M. C.; Klenk, R. 12.6% Efficient CdS/Cu(In,Ga)S₂-Based Solar Cell with an Open Circuit Voltage of 879mV Prepared by a Rapid Thermal Process. *Sol. Energy Mater. Sol. Cells* **2011**, 95, 864–869.
- 50 Jackson, P.; Hariskos, D.; Lotter, E.; Paetel, S.; Wuerz, R.; Menner, R.; Wischmann, W.; Powalla, M. New World Record Efficiency for Cu (In,Ga)Se₂ Thin-Film Solar Cells beyond 20%. **2011**, 3–6. <https://doi.org/10.1002/pip>.
- 51 Larsson, F.; Nilsson, N. S.; Keller, J.; Frisk, C.; Kosyak, V.; Edoff, M.; Törndahl, T. Record 1.0 V Open-circuit Voltage in Wide Band Gap Chalcopyrite Solar Cells. *Prog. Photovoltaics*

- Res. Appl.* **2017**, 25 (9), 755–763. <https://doi.org/10.1002/pip.2914>.
- 52 Moriya, M.; Minegishi, T.; Kumagai, H.; Katayama, M.; Kubota, J.; Domen, K. Stable Hydrogen Evolution from CdS-Modified CuGaSe₂ Photoelectrode under Visible-Light Irradiation. *J. Am. Chem. Soc.* **2013**, 135 (10), 3733–3735. <https://doi.org/10.1021/ja312653y>.
- 53 Hellstern, T. R.; Palm, D. W.; Carter, J.; DeAngelis, A. D.; Horsley, K.; Weinhardt, L.; Yang, W.; Blum, M.; Gaillard, N.; Heske, C.; Jaramillo, T.F. Molybdenum Disulfide Catalytic Coatings via Atomic Layer Deposition for Solar Hydrogen Production from Copper Gallium Diselenide Photocathodes. *ACS Appl. Energy Mater.* **2019**, 2 (2), 1060–1066. <https://doi.org/10.1021/acsaem.8b01562>.
- 54 Deangelis, A.; Kaneshiro, J.; Gaillard, N.; Chang, Y.; Kowalczyk, J.; Mallory, S. A.; Miller, E. Low-Temperature Indium Molybdenum Oxide as a Window Layer in CIGS Photovoltaic Devices. In *Conference Record of the IEEE Photovoltaic Specialists Conference*; 2010. <https://doi.org/10.1109/PVSC.2010.5614632>.